From Quantum Dots to Hetero Nanorods: Structural Analysis and Light Matter Interaction

John Sundar Kamal

Promoter: Prof. Dr. Ir. Zeger Hens
Thesis submitted in fulfillment of the requirements of the degree of Doctor(Ph.D) in Sciences: Physics

Ghent University
Faculty of Science
Department of Inorganic and Physical Chemistry
Academic year 2011-2012

Summary

Colloidal semiconductor nanocrystals (NCs) are a new class of materials, whose physical and material properties are strongly dependent on their size, shape, crystal structure, and surface characteristics. These nanocrystals can be synthesised as spherical particles-quantum dots(QDs), rod like particles-quantum rods(QRs) and as heterostructures. Progress in synthesis is driven by the combination of optoelectronic properties tunable by size and shape, and versatile wet-chemical processing, which opens up a vast range of potential applications. They find applications as photodetector, photovoltaic cell, flurophores, lasers and light emiting diodes *etc.* In this work the focus is to understand the transition from QDs to hetero nanorods interms of their optical properties. The formation of complex hetero nanorods is investigated by structural analysis to understand the synthesis process.

In chapter 3, optical properties of CdTe QDs are investigated. CdTe QDs are synthesised by the hot injection method. The synthesised QDs are examined by X-ray diffraction (XRD), which confirms the formation of zinc blende crystal structure. Their mean diameter and size dispersion is determined by transmission electron microscopy (TEM) measurements. UV-vis absorption spectra clearly shows a blue shift of the band gap with respect to bulk CdTe. Combining the band gap and the mean diameter of the CdTe QDs a sizing curve is constructed. The concentration of the CdTe QDs is determined by inductively coupled plasma mass spectrometry (ICP-MS) and Rutherford backscattering spectroscopy (RBS) measurements. Combining concentration, absorbance and mean diameter data, the absorption coefficients of CdTe QDs are calculated and compared with the literature data. We observe at 410 nm, intrinsic absorption coefficient μ_i is size-independent. The resulting value is close to the expected value for bulk CdTe

determined by using Maxwell-Garnett model and can be used for determining the volume fraction of spherical CdTe QDs in colloidal dispersions. Despite the size-independent μ_i at 410 nm, we observe persistent quantum confinement effects on the E_1 transition, which appears less pronounced and blueshifted in CdTe QDs relative to its bulk value of 365 nm.

Around the band gap, we find an integrated absorption coefficient μ_{gap} that scales proportionally to the inverse of the QD volume. Especially for the smaller diameters, significant deviations are found as compared to widely used literature values. The corresponding oscillator strength f_{exc} is calculated from the μ_{gap} and is almost size-independent in the diameter range 3–7 nm. Radiative lifetimes predicted based on f_{exc} are in line with experimental results and published values if a 16-fold degeneracy for the first exciton is assumed.

In chapter 4 and chapter 5, the absorption anisotropy in CdSe QRs, CdS QRs and CdSe/CdS dot-in-rods are investigated. The QRs are synthesised by the hot injection synthesis. The synthesised QRs are exmained by XRD which confirms the formation of QRs with wurtzite crystal structure. The dimensions of the QRs are deduced by TEM measurements. In the case of synthesised CdSe QRs dispersed in heptane, the experimental absorption coefficient μ at 400 nm is determined by combining UV-vis absorption spectroscopy and elemental analysis. The results show that absorption coefficient μ at 400 nm is in line with the theoretical values calculated in the frame work of Maxwell-Garnett model using local field approximatiom. The absorption coefficient of colloidal CdSe QRs is neither a constant nor equal to that of colloidal CdSe QDs. Due to the anisotropy of the local field factors, it markedly increases with increasing aspect ratio, making QRs in general stronger absorbers than QDs of the same material. The absorption anisotorpy implies that randomly dispersed CdSe QRs have larger absorption coefficient than CdSe QDs.

In addtion, we introduce and assess an electro-optical method to analyze absorption anisotropy of dispersed QRs. In this method, the absorbance of the dispersion is measured while aligning the nanocrystals using an electric field. Using alternating electric fields

high enough to prevent charge accumulation at the electrodes and low enough to ensure rotational relaxation, we demonstrate that the resulting change in absorbance as a function of field strength can be quantified by a model based on Boltzmann statistics. The method is validated using CdSe and CdS quantum rods, where we find a difference between the absorption coefficient at 400 nm and at bandgap for fields polarized parallel and perpendicular to the rod axis that is fully in line with the predictions of the local field approximation. Finally, using this method, we extended the analysis to the first exciton transition of CdSe/CdS dot-in-rods. Based on a quantitative analysis of the absorption change as a function of field strength, we find that this absorption is almost fully polarized, with a vanishing absorption coefficient for fields that are polarized perpendicular to the long axis of the rods.

The nature of wave function delocalization in CdSe/CdS dot-in-rods has been investigated by temperature-resolved and time-resolved spectroscopy. We observed that the thermally induced photoluminescence (PL) quenching is absent, which enables to study the radiative decay process directly and its effects on the wave function delocalization. The radiative lifetime increases with decreasing CdSe core size has been observed, this is caused by different degree of localization of the electronic wave function. Besides this the radiative lifetime also increases with temperature due to the change in the band offset. This change in lifetime, quantitatively agrees with a conduction band offset of 0.3 eV, as reported in literature. These results indicate that the degree of electron delocalization in the lowest conduction band level can be controlled by the size of the core and the temperature.

In chapter 6, colloidal PbS/CdS heterorods are synthesised by successive cationic exchange steps, starting from CdS quantum rods. The resulting particles are evaluated by absorption spectroscopy, photoluminescence spectroscopy and TEM based techniques. The successive, complete Cd/Cu and Cu/Pb exchanges leads to the formation of PbS QRs. Thus formed PbS QRs are observed to be polycrystalline. The different crystallities observed to have grain boundaries and are seperated by (111) twin planes. The distance between different twin planes is comparable to the stacking fault observed in CdS QRs. The photoluminescence quan-

tum yield measured in PbS QRs is observed to be very low compared to 55% in PbS/CdS heterorods formed by partial exchange Cd/Pb. Instead of simple core/shell structures, this results in the formation of multiple dot-in-rod heterostructures, probably because each PbS segment in the original PbS QR is transformed into a single PbS/CdS unit. The number of PbS dots in a single rod depends on the original CdS rod length. Since further tuning is possible by limiting the extent of the final cationic exchange, this shows that successive cationic exchange is a versatile approach to form complex anisotropic heteronanostructures active in the IR. This opens new vistas in the development of applications in, *e.g.*, solar concentrators and QD-based near-IR light sources.

Contents

List of commonly used Acronyms

IR	infrared
UV	ultra violet
QDs	quantum dots
QRs	quantum rods
DPE	diphenyl ether
HPA	hexylphosponic acid
MeOH	methanol
BuOH	butanol
ODE	octadecene
OA	oleic acid
OLA	oleylamine
ODPA	octadecylphosponic acid
TDPA	tetradecylphosponic acid
TOP	tri-n-octylphosphine
TOPO	tri-n-octylphosphine oxide
TOPS	tri-n-octylphosphine sulfide
TOPSe	tri-n-octylphosphine selenide
EDX	energy dispersive X-ray (analysis)
(HR-)TEM	(high resolution) transmission electron microscopy
(HAADF-)STEM	high annular dark field scanning TEM
XRD	X-ray diffraction
ICP-MS	inductively coupled plasma mass spectrometry
ICP-OES	inductively coupled plasma optical spectrometry
RBS	Rutherford backscattering spectroscopy
a	lattice parameter

d	(mean) nanocrystal diameter
C	nanocrystal concentration
N	number of atoms per particle
T	absolute temperature
p	dipole moment
R	ratio
g	degeneracy
E_g	bulk semiconductor band gap
E_0	nanocrystal band gap
E_{LO}	longitudinal phonon energy
$A_{(410)}$	absorbance (at 410 nm)
$\mu_{(410)}$	intrinsic absorption coefficient (at 410 nm)
MG	Maxwell-Garnett (model)
f_{LF}	local field factor
α	absorption coefficient (for bulk)
f_{if}	oscillator strength
ϵ	molar extinction coefficient
$\epsilon_{(eff)}$	(effective) dielectric constant
$\epsilon_{R(I)}$	real (imaginary) part of the dielectric function
$n_{(eff)}$	(effective) refractive index
$k_{(eff)}$	(effective) extinction coefficient
n_s	refractive index of the solvent
f	volume fraction
V_{QD}	volume of the quantum dot
β	aspect ratio
Γ	peak width
Γ_{inh}	inhomogenous peak width
Γ_{LO}	exciton-LO phonon coupling coefficient
Γ_{AC}	exciton-acoustic phonon coupling coefficient
η	viscoity of the solvent
τ_{rot}	rotational relaxation time
τ_{tr}	cell transit time

Chapter I

General introduction

1.1 Colloidal quantum dots-an introduction

Colloidal quantum dots are nanostructures with sizes in the range of 2-20 nm and hence exhibit size quantization effect [1]. This makes them new fundamental building blocks for the new generation of electronics and photonics applications. Progress in colloidal nanocrystal synthesis over the past two decades has made available a wide range of metal, metal oxide and semiconductor nanocrystals with an exceptional control over their size, size dispersion and shape. [2] It all started with the seminal work of L.E.Brus [3,4] and A.L.Efros [5,6] with their theoretical investigation on few nanometer sized semiconducting colloids and semiconducting material grown on dielectric matrix respectively. They showed that with the change in size imparts change in their band gap energy resulting in new optical characteristics. This came into reality by the advent of hot injection method or organometallic approach by Murray et al. [7] to grow semiconducting nanocrystals. According to this method nucleation and growth is achieved by heating organometallic cation precursor in a non coordinating solvent and subsequently injecting cold anion precursor at elevated temperatures yielding in suitable nanocrystals. The wet chemical processing methods makes its cost, handling and imparting functionality effective and efficient. Since then many scientific groups have ventured into the research on colloidal nanocrystals resulting in better synthetic control and tune ability of size and shape.

The opto-electronic properties of nanocrystals has potenial to be used in numerous technological applications. Their sharp

emission and high quantum efficiencies enables to be used as flurophores for bio-tagging[8]. The surface of the nanocrystals can be functionalized for selective attachment with antibodies or peptides that can recognize certain specific proteins or cells which paves way for targeted drug delivery[9]. The colloidal nanocrystals have narrow emission width and spectral clarity which is suitable for making light sources[10]. IR lasers for telecommunication purposes are an interesting prospect and has been demonstrated with PbS QDs at low temperatures[11]. Luxury in automobile segment like IR imaging for navigation assistance in the night comes with a big price tag. With HgTe QDs it is possible to have efficient photo detection[12] in the IR at an affordable price. There is considerable effort in enhancing the efficiency of colloidal nanocrystal based solar cells[13] from 4% at present. Numerous possibilities associated with this class of materials paves way for more research initiatives.

1.2 Size confinement effect

In semiconducting material the physical properties are dictated by the composition of the material. However when the size of the material is reduced to few nanometers it results in the change of the physical properties. This phenomenon happens due to size confinement effect. In a bulk solid semiconducting material, the motion of the particles (electrons, holes, excitons etc) is not restricted by periodic boundary conditions. In a way the particles are not affected by the borders of the solid interms of wavefunction and energy. If however the dimension of the solid are reduced, the particles sense the borders and infinite extension of the solid in all three spatial coordinates does not hold anymore. In such situtations system is regarded to be quantum confined. This can also be explained by the particle in a box model. By solving the Schrödinger equation for a particle with mass m results in discrete energy levels with eigen energies E_n:

$$E_n = \frac{\pi^2 \hbar^2}{2mL^2}.n^2 \tag{1.1}$$

The equation 1.1 shows that on reducing the size (L) of the box results in an increase in the energy of the first level. On the contrary in bulk material the L is infinite and the energy

levels are continuous. If the system is confined in three dimensions then it is called a quantum dot. Where as a system confined in two or one dimension, it is called a quantum wire or a quantum well respectively. Similar to the solution of a particle in a box is the Bruce equation which gives solution for the colloidal spherical nanocrystal with radius R as

$$E = E_g + \frac{\hbar^2 \pi^2}{2\mu_{ex} R^2} - \frac{1.786 e^2}{\epsilon R} \tag{1.2}$$

Here E_g is the bulk band gap, μ_{ex} effective mass of exciton and the third term in the equation 1.2 corresponds to the coulomb interaction term of electron and holes. This shows that by tuning the size of the nanocrystal the bandgap can be engineered to have optical properties from UV to IR. Hence size confinement or size quantisation effect is the basis of exceptional optical properties in colloidal nanocrystals.

1.3 Hot injection synthesis

Hot injection synthesis is a robust bottom-up technique to synthesis nanocrystals which involves wet chemical processing. This means it does not require substrate to grow them unlike in other technique like molecular beam epitaxy, chemical vapour deposition *etc.* As they are colloids, the nanocrystal surface is encapsulated by a layer of surfactants or ligands which stearically stabilizes them. The wet chemical processing allows tailoring of functionality by ligand exchange and formation of QD thin films by techniques such as spin coating, drop casting, ink-jet printing and Langmuir-Blodgett deposition. The ease of processability and imparting functionality makes it cost efficient and opens new vistas for design and fabrication of opto-electronic devices.

The technique of nucleation and growth of colloidal nanocrystals was first demonstrated by Murray *et.al.*[7] with the synthesis of PbS nanocrystals. A typical synthesis is done with a mixture of cation precursor, organic surfactant, and non coordinating solvent. This mixture is then heated in an inert atmosphere and subsequently followed by injection of cold (room temperature) anion precursor yields in the formation of nanocrystals. The reaction mechanism is a two step process, in the first step, the precursors

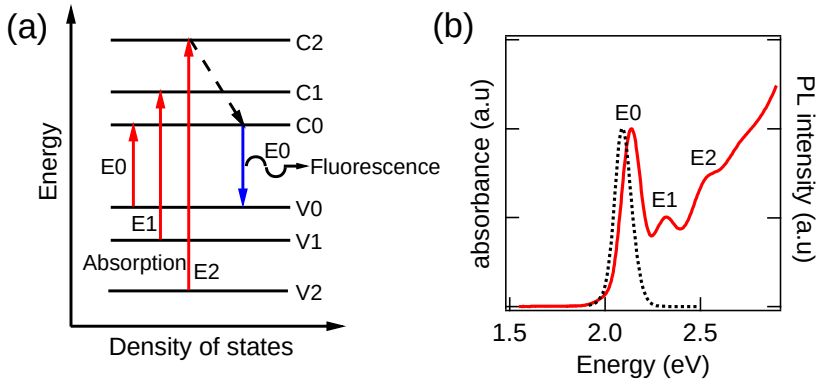

Figure 1.1: **(a)**Schematic diagram of absorption and emission process.**(b)** Absorption and emission spectrum of CdTe QDs represented with solid lines and dotted lines respectively.

transform to form supersaturated monomers. These then form nanocrystals and their growth is influenced by the presence of surfactants. In the growth regime surfactant molecules adsorbs and desorbs rapidly from the nanocrystal surface, enabling addition of monomers. The presence of monolayer of surfactants on the nanocrystal surface avoids aggregation and due to the strearic hindrance slows down the growth rate of nanocrystals. This controlled event of nucleation and growth is the salient feature of hot injection synthesis.

1.4 Absorption and emission of light

Semiconductor nanocrystals have a band gap, i.e forbidden gap between the conduction and the valence band. This gap is responsible for the interesting optical properties associated with it. When a photon is absorbed with energy equalent to the transition energy required for transition of an electron from top of the valence band to the bottom of the conduction band, it results in the formation of an electron-hole pair called the exciton. This exciton can annihilate with an emission of one photon which gives rise to fluorescence. Schematic diagram explainig the absorption and emission process is shown in figure 1.1(a). Absorption and emission spectrum of semiconductor quantum dots represents the electronic states and its transitions. In figure 1.1(b) shows an absorption and emission spectrum of an ensemble of CdTe QDs with

an average size of 4 nm. In the absorption all the electronic states that absorb are shown. The three prominent features appearing in CdTe absorption spectrum corresponds to the E_0, E_1 and E_2 transition. Where as fluorescence occurs only when bottom of the conduction and top of the valence band are involved in the transition. Hence the emission spectrum of CdTe involves E_0 transition only and hence the peak is narrower.

1.5 Nanorod synthesis

Nanorods are synthesized in a similar procedure as described for QDs by hot injection method. The shape control of nanocrystals is achieved by manipulation of the growth kinetics[2]. The synthesis of colloidal CdSe nanorods was first reported by Peng *et.al.*[14]. The possibility of shape control arises because intrinsically wurtzite CdSe is highly anisotropic with unique c axis. With this facet the surface energy associated is higher compared to other facets of the crystal. If the monomer concentration is high at the onset of the reaction the high energy facets grow faster compared to the low energy facets resulting in the formation of nanocrystals with rod like shape. To have better control on the shape and aspect ratio a mixture of phosphonic acids are used. The phosphonic acids bind with the facet along the c axis strongly compared to others. This facilitates the controlled growth of nanorods and figure 1.2(a) shows cartoon of shape evolution of nanorod. This kinetic growth mechanism of synthesis of CdSe QRs can be extended to other material systems like CdS[15] and TiO_2[16] *etc.*

The shape control imparts new dimension to the nanocrystals to be classified as one dimensional nanostructures. This is still in the quantum confinement regime as two out of the three dimensions are in the size range of less than 10 nm. The freedom in the one dimension makes QRs different from the QDs. This can be understood in terms of the electronic states by looking at the density of states(D(E)) which represents the number of electronic states in a unitary interval of energy. Figure 1.2(b) shows D(E) as a function of energy (E), in the case of QDs discrete states of energy are observed with a delta function. Where as in QRs, D(E) is proportional to $(E\text{-}E_0)^{\frac{-1}{2}}$, hence quasi-continues distribution of states is observed with a saw tooth like function. In terms

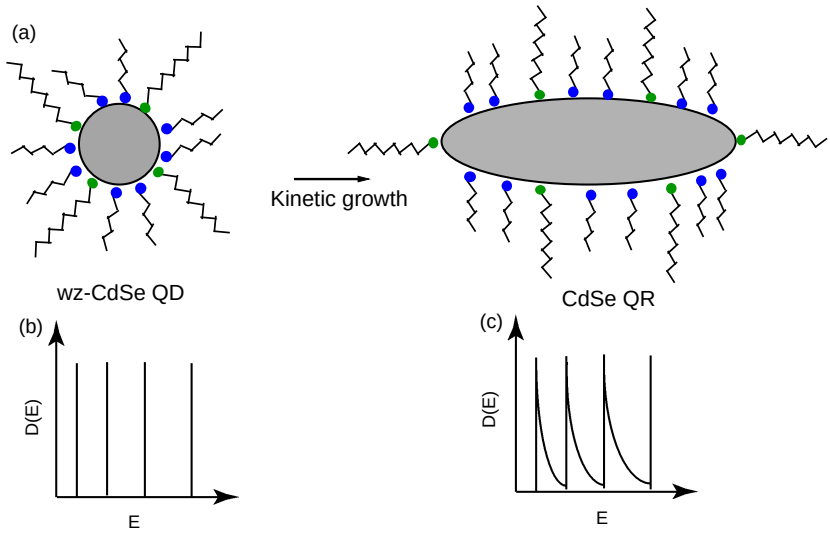

Figure 1.2: **(a)** cartoon of CdSe nanorod evloution from wz-CdSe core with long chain and short chain phosphonic acid ligands bound on the surface.Density of states of **(b)** quantum dot and **(c)** quantum rod.

of the optical properties the emission from QDs are quasi circularly polarized where as QRs are linearly polarized. In literature this is demonstrated by luminescence polarization experiment on single CdSe QR[17] and theoretically explained on the basis of fine structure of ground state excitons[18].

1.6 Heterostructures

A significant fraction of the organically stabilized core nanocrystals exhibit surface related trap states acting as fast non radiative de-excitation channels for photo generated charge carriers, there by reducing the fluorescence quantum yield. A strategy to overcome nanocrystal surface passivation is by growing shell of a different semiconductor material around it. In this process of protecting the core material results in the formation of heterostructures. The improved optical properties are directly related to the band alignment present in these heterostructures, *i.e* how the charge carriers are localized or delocalized in the core and shell material. So there are three possibilities arising now with the band alignment namely type I, type 1.5 and type II. Figure 1.2(a) shows schematic dia-

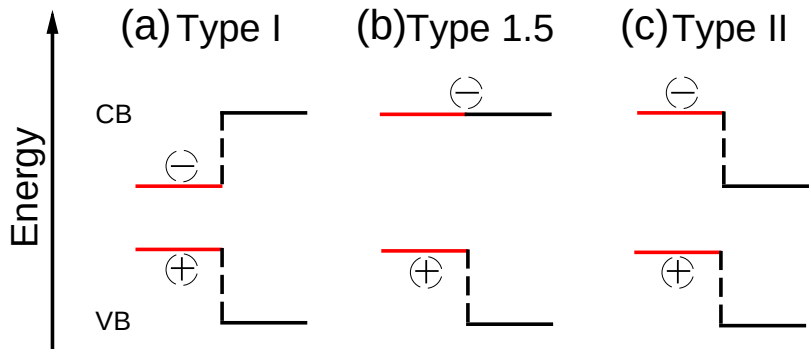

Figure 1.3: The schematic diagram representing the band alignment present in **(a)**type I system,**(b)**type 1.5 system and **(c)**type II system.

gram of type I system where the band energy of the core system is narrower compared to the shell with a higher band gap energy. This results in confinement of the electron and hole pair in the core of the material itself, which is suitable for applications like light sources and flurophores for tagging experiments. The figure 1.2(b),(c) shows schematic diagram of the type 1.5 and type II system where the band alignment is staggered. The type 1.5 arises when shell material is not able to localize the electrons with in the core of the material due to the energy band offset of the band gap and the electrons are delocalized over the entire hetero nanocrystal, where as the hole is confined in the core of the material. On the contrary in the type II, the band alignment is such that the electrons are localized in the shell and the holes are localized in the core of the material resulting in spatially separated charge pair. This system is suited for lasing and light harvesting applications. In a way by suitable choice of material size and shape of the core and the shell system one can engineer the band gap catering to desired opto-electronic applications. By this process fluorescence efficiency and stability against photo-oxidation of nanocrystals has significantly improved. There are different ways to synthesise heterostutures, among them the three prominent synthesis used often are discussed in the following.

SILAR method: SILAR stands for successive ion layer adsorption and reaction[19]. This shell growth technique is done by al-

ternatively injecting cationic and anionic precursors to the core nanocrystal solution at temperature below their growth temperature. Only half monolayer of material is deposited at a time. By this method monodisperse heterostructures can be synthesized for instance CdTe/CdSe[20,21], CdSe/ZnSe[22], CdSe/ZnTe[21] and ZnO/CdS[23] etc. While designing the reaction scheme for the SILAR the lattice mismatch at the interface of the desired materials should be minimum. Otherwise this can induce strain at the interface which can drastically reduce the photoluminescence quantum yield (PLQY) and can even trigger homogeneous nucleation event (formation of separate nuclei rather than heterostructure).

Cationic exchange: Is a process in which ionic nanocrystals can be used as starting material where the composition is altered by synthesis. The cation or the anion is substituted by another ion in the solution. This was demonstrated in literature with CdSe nanocrystals which readily converted to Ag_2Se nanocrystals efficiently by injecting an alcoholic solution of Ag^+ ions into a suspension of CdSe nanocrystals in toluene. The surface to volume ratio makes the entire nanocrystal lattice accessible for the solid state diffusion facilitating cationic exchange process. CdSe/Ag_2Se segmented QRs and PbS/CdS dot-in-rods have been synthesized wit this procedure[24]. The remarkable part about this synthesis procedure is it gives accessibility to make heterostructures based PbS and PbSe QRs which is not ordinarily possible due to their rock salt crystal structure. Hence cationic exchange process is a new route to synthesize complex heterosturctures.

Seeded growth approach: The method was demonstrated by synthesis of CdSe/CdS dot-in-rod heterostructure[25]. This method is similar to the hot injection method described for synthesis of QRs. The synthesis is based on the co-injection of appropriate precursors and pre synthesized spherical wurtzite CdSe nanocrystal seeds in a reaction flask that contains mixture of hot surfactants suited for growth of CdS nanocrystals. This facilitates in growth of CdS on CdSe seeds rather than not forming separate nuclei is due to heterogeneous nucleation requires very low activation energy compared to homogeneous nucleation. Thus formed heterorods have very narrow size distribution, high aspect ratio

tune ability, less stacking faults and a high PLQY. Now with this method CdSe/CdTe[26], ZnSe/CdS[25] heterorods can be prepared.

1.7 Structural characterization by TEM

TEM analysis is an indispensible tool for the characterization of nanocryatals. It gives valuable information on the size, morphology, crystal structure and chemical composition of the synthesized nanocrystals. The bright field (BF) and HR-TEM mode of imaging are the heart of TEM technique which are described in the following paragraphs.

Bright field imaging: In the bright field mode of the TEM, an objective aperture is placed on the back focal plane of the objective lens which allows only the direct beam to pass through. The direct beam interacts with the sample to form image. The image formed shows contrast due the mass-thickness and diffraction. This contrast happens as the electron beams gets scattered by a thick regions, heavy elements at large angles and by oriented crystalline material due to diffraction which does not pass through the small aperture and appears dark in the BF image. In our case in the examination of nanocrystals an additional aperture is inserted to further narrow down the path of electron beam which enhances diffraction contrast of the TEM images. Figure 1.4(a) shows the schematic diagram of the BF image formation and the corresponding BF image of ensemble of CdTe nanocrystals .

HR-TEM imaging: In this mode a large objective aperture has to be selected that allows the direct beam and the diffracted beam to pass through. The interference of the direct beam and the diffracted beam results in an image with phase contrast. In our case with a resolution of 0.8 A for a crystalline material oriented along a zone axis HR-TEM images of the lattice planes can be obtained. The atomic structure of the material can be directly examined and also gives information on defects and dislocations present in the material. Figure 1.4(b) shows schematic diagram of the image formation in HR-TEM mode and the corresponding example of an HR-TEM image of PbTe/CdTe heterostructure.

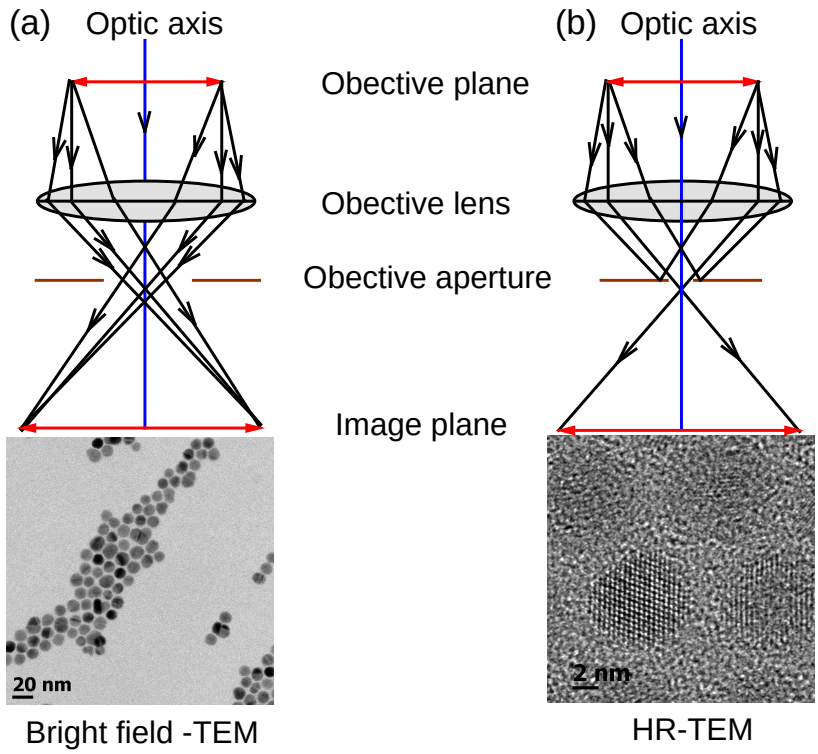

Figure 1.4: Schematic ray diagram illustrating imaging in (a) bright field mode and (b) HR-TEM mode.

1.8 Thesis outline

The goal of the thesis is to understand the linear optical properties emanating from QDs and anisotropic systems like the QRs. This goal is achieved by synthesizing particles and characterizing them (optically, elementally and structurally) to study them. This thesis revolves around the CdTe QDs, CdSe QRs, CdS QRs, CdSe/CdS core shell dot-in-rod and PbS/CdS core shell multiple dots in a rod systems as the central characters. QR systems when subjected to Electric field, how they react has been captured optically. There is been an effort to understand how complex core shell systems like multiple dots in a rod system structurally evolve and what influence they have on their optical properties. Now moving on to the brief break up details of what you will come across in the different chapters is as follows.

Chapter two 'light absorption by colloidal quantum dots-general concept'. This chapter gives an overview on quantitative analysis of light absorption by QDs in the context of Maxwell-Garnett model. The various physical quantities describing the optical properties of semiconducting nanocrystals are introduced in this chapter.

Chapter three 'size dependent optical properties of zinc blende-CdTe QDs'. CdTe QDs are interesting material as their emission can be tuned in the complete visible spectrum. This chapter deals with how these QDs can be synthesized and how to characterize them structurally (XRD, TEM), optically (absorption spectroscopy) and elementally (ICPMS, RBS). Starting from absorption spectrum how we can deduce the absorption coefficients, oscillator strengths and exciton life time is discussed in detail.

Chapter four 'optical anisotropy in CdSe and CdS QRs'. Moving on from QDs to QR systems shape anisotropy comes into picture and how does this alter the optical properties will be mainly dealt in this chapter. The absorption coefficients of CdSe QRs with different aspect ratios are determined experimentally and compared with theoretical values deduced in the framework of MG model taking anisotropy into account. The anisotropy effect is further substantiated by electro-optical measurements on CdSe and CdS QRs.

Chapter five 'direct determination of absorption anisotropy and wave function delocalization in CdSe/CdS core shell dot-in-rod'. In this chapter the focus is on how to experimentally determine the absorption anisotropy observed in CdSe/CdS core shell dot-in-rod systems which has been always assumed to explain the polarized emission observed in these systems. Another interesting attribute in this chapter is the nature of wave function delocalization observed. This is examined by temperature and time resolved spectroscopy on samples with constant shell thickness and varying the core size of the CdSe QDs.

Chapter six 'PbS-based quantum rods by cationic exchange, structural analysis'. The highlight of this chapter is the new heterostructure synthesis, how does it undergo structural changes

during synthesis to evolve to a complex system. How the structure influences the optical properties is described.

Bibliography

[1] A. L. Efros and M. Rosen, *The electronic structure of semiconductor nanocrystals*, Annu. Rev. Mater. Sci. **2000**, *30*, 475.

[2] Y. Yin and A. P. Alivisatos, *Colloidal nanocrystal synthesis and the organicinorganic interface*, Nature **2005**, *437*, 664.

[3] L. E. Brus, *Electron electron and electron-hole interactions in small semiconductor crystallites - the size dependence of the lowest excited electronic state*, J. Chem. Phys. **1984**, *80*, 4403.

[4] L. E. Brus, *Electronic wave-functions in semiconductor clusters - experiment and theory*, J. Chem. Phys. **1986**, *90*, 2555.

[5] A. L. Efros and A. L. Efros, *Interband absorption of light in a semiconductor sphere*, Sov. Phys. Semicond. **1982**, *16*, 772.

[6] A. I. Ekimov, A. L. Efros and A. A. Onushchenko, *Quantum size effect in semiconductor microcrystals*, Solid State Commun. **1985**, *56*, 921.

[7] C. Murray, D. J. Norris and M. G. Bawend, *Synthesis and characterization of nearly monodisperse CdE (E = S, Se, Te) semiconductor nanocrystallites*, J. Am. Chem. Soc. **1993**, *115*, 8706.

[8] I. Medintz et al., *Quantum dot bioconjugates for imaging, labelling and sensing*, Nat. Mater. **2005**, *4*, 435.

[9] W. Cai et al., *Peptide-labeled near-infrared quantum dots for imaging tumor vasculature in living subjects*, Nano Lett. **2006**, *6*, 669.

[10] E. Jang et al., *White-light-emitting diodes with quantum dot color converters for display backlights*, Adv. Mat **2010**, *22*, 3076.

[11] S. Hoogland et al., *A solution-processed 1.53 mum quantum dot laser with temperature-invariant emission wavelength*, Opt Express. **2006**, *14*, 3273.

[12] T. S. Rauch et al., *Near-infrared imaging with quantum-dot-sensitized organic photodiodes*, Nat. Photonics **2009**, *3*, 332.

[13] E. H. Sargent, *Colloidal quantum dot solar cells*, Nat. Photonics **2012**, *6*, 133.

[14] Z. A. Peng and X. Peng, *Nearly monodisperse and shape-controlled CdSe nanocrystals via alternative routes: nucle-*

ation and growth, J. Am. Chem. Soc. **2002**, *124*, 3343.

[15] Y. D. Li et al., *Nonaqueous synthesis of CdS nanorod semiconductor*, Chem. Mater. **1998**, *10*, 2301.

[16] M. Jun, Y.-W. Tedde et al., *Surfactant-assisted elimination of a high energy facet as a means of controlling the shapes of TiO2 nanocrystals*, J. Am. Chem. Soc. **2003**, *125*, 15981.

[17] J. T. Hu et al., *Linearly polarized emission from colloidal semiconductor quantum rods*, Science **2001**, *292*, 2060.

[18] A. Shabaev and A. L. Efros, *1D exciton spectroscopy of semiconductor nanorods*, Nano Lett. **2004**, *4*, 1821.

[19] J. J. Li et al., *Large scale synthesis of nearly monodisperse CdSe/CdS core/shell nanocrystals using air-stable reagents via successive ion layer adsorption and reaction*, Chem. Mater. **1998**, *10*, 2301.

[20] D. Dorfs et al., *Type-I and type-II nanoscale heterostructures based on CdTe nanocrystals: a comparative study.*, Small **2008**, *4*, 1148.

[21] S. Kim et al., *Type-II quantum dots:? CdTe/CdSe(core/shell) and CdSe/ZnTe(core/shell) heterostructures*, J. Am. Chem. Soc **2003**, *125*, 11466.

[22] S. A. Ivanov et al., *Type-II core/shell CdS/ZnSe nanocrystals:? synthesis, electronic structures, and spectroscopic properties*, J. Am. Chem. Soc. **2007**, *129*, 11708.

[23] F. Xu et al., *Long electron?hole separation of ZnO-CdS core?shell auantum dots*, J. Phys. Chem. C **2009**, *113*, 19419.

[24] J. M. Luther et al., *Synthesis of PbS nanorods and other ionic nanocrystals of complex morphology by sequential cationexchange reactions*, J. Am. Chem. Soc. **2009**, *131*, 16851.

[25] L. Carbone et al., *Synthesis and micrometer-scale assembly of colloidal CdSe/CdS nanorods prepared by a seeded growth approach*, Nano Lett. **2007**, *7*, 2942.

[26] H. McDaniel, J. M. Zuo and M. Shim, *Anisotropic strain-induced curvature in Type-II CdSe/CdTe nanorod heterostructures*, J. Am. Chem. Soc. **2010**, *132*, 3286.

Chapter II

Light absorption by colloidal quantum dots - general concept

2.1 Introduction

The size-dependent absorption of electromagnetic radiation by semiconductor nanocrystals or quantum dots (QDs) can reveal information on their most fundamental opto-electronic properties. It gives a first view on the quantization of their energy levels and it lies at the heart of various QD applications in photodetection [1], photovoltaics [2,3], color conversion for LEDs and displays [4–6] and fluorescent labeling [7]. Additionally the QD absorption spectrum enables a rapid screening of the basic QD properties, such as size, size dispersion and concentration in solution. This chapter gives a comprehensive overview of the quantitative analysis of light absorption by QDs, mainly within the context of the Maxwell-Garnett (MG) effective medium theory. After a brief introduction to the MG effective medium approximation and the local field approximation, the various quantities used to quantify light absorption by QDs are introduced on a systematic basis. These physical quantities will be occuring time and again in this thesis, hence they are briefly described in this chapter.

2.2 Light Absorption by colloidal QDs

In general for any material can be described by its complex dielectric function $\tilde{\epsilon}$ which is described as

$$\tilde{\epsilon} = \epsilon_R + i\epsilon_I \tag{2.1}$$

this inturn can be related to the complex refractive index of the material $\tilde{n} = n + i\kappa$ as

$$\begin{aligned} \epsilon_R &= n^2 - \kappa^2 \\ \epsilon_I &= 2n\kappa \end{aligned} \tag{2.2}$$

Now if the material absorbs light then the absorbance can be described as the logrithamic ratio of incident light I_0 and the transmitted light I_t as

$$A = \log\left(\frac{I_0}{I_t}\right) \tag{2.3}$$

If the medium of interest is characterized at a given wavelength λ by refractive index $\tilde{n}$, can be expressed as the attenuation of light intensity I(x) travelling a distance x as

$$I(x) = I_0 \mathrm{e}^{-\frac{4\pi\kappa}{\lambda}x} \tag{2.4}$$

This exponential decay of I(x) makes A per unit length an intrinsic property of the medium. Hence, we can define a thickness independent absorption coefficient α as follows

$$\alpha = \frac{\ln 10 \cdot A}{L} = \frac{4\pi\kappa}{\lambda} \tag{2.5}$$

This relation already couples the experimentally accessible A to a materials property, the extinction coefficient κ. For composite media *i.e* in our case QDs suspended in a solvent, this equation remains valid when replacing κ with an effective extinction coefficient κ_{eff}. The *absorption coefficient* of the composite is represented by μ, hence we obtain:

$$\mu = \frac{\ln 10 \cdot A}{L} = \frac{4\pi\kappa_{eff}}{\lambda} \tag{2.6}$$

In the following subsection we will see how the effective medium theory can relate the material properties to the light absorption by colloidal QDs.

2.3 The Maxwell-Garnett effective medium approach

A colloidal dispersion is a composite medium, containing both QDs and solvent. Its composition can be described by the QD volume fraction f, defined as the volume occupied by the QDs per unit of sample volume, or the amount concentration c of the QDs, which is the amount of QDs in mole per unit sample volume. Writing the (complex) dielectric function of the transparent solvent as $\epsilon_s = n_s^2$ and that of the QDs as $\tilde{\epsilon}$, the effective dielectric function $\tilde{\epsilon}_{eff}$ of this composite medium can be expressed using the Maxwell-Garnett mixing rule.[8,9] A convenient way to derive this is to look at the QDs as polarizable point dipoles in the environment of the solvent. In that case, $\tilde{\epsilon}_{eff}$ can be related to the polarizability a of an individual QD by means of the Clausius-Mossotti relation (N_A, Avogadro's number):

$$\frac{\tilde{\epsilon}_{eff} - \epsilon_s}{\tilde{\epsilon}_{eff} + 2\epsilon_s} = \frac{1}{3} c N_A a \tag{2.7}$$

For the specific example of spherical particles with a radius r, a is given by:

$$\begin{aligned} a &= 4\pi r^3 \beta \epsilon_s \\ \beta &= \frac{\tilde{\epsilon} - \epsilon_s}{\tilde{\epsilon} + 2\epsilon_s} \end{aligned} \tag{2.8}$$

Combining eqs 2.7 and 2.8 results in the well-known Maxwell-Garnett mixing rule:

$$\tilde{\epsilon}_{eff} = \frac{1 + 2\beta f}{1 - \beta f} \epsilon_s \tag{2.9}$$

In the case of a sufficiently dilute composite ($f \ll 1$), the real and imaginary part of $\tilde{\epsilon}_{eff}$ read:

$$\begin{aligned} \epsilon_{eff,R} &= \epsilon_s \\ \epsilon_{eff,I} &= \frac{9\epsilon_s^2}{|\tilde{\epsilon} + 2\epsilon_s|^2} f \epsilon_I \end{aligned} \tag{2.10}$$

Clearly, $\epsilon_{eff,R}$ is reduced to the real dielectric function of the solvent. $\epsilon_{eff,I}$ on the other hand finds an elegant interpretation within the concept of the *local field factor* f_{LF}, which appears in

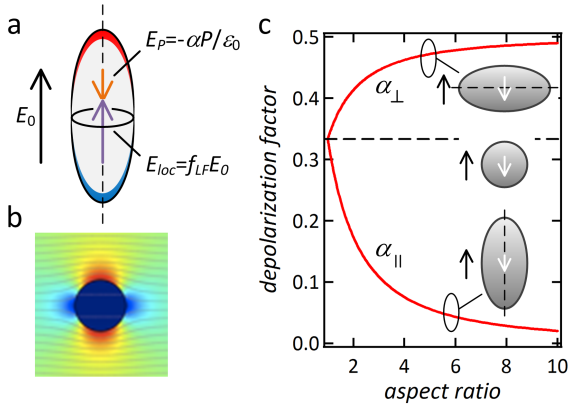

Figure 2.1: **(a)** In an ellipsoid, a (black) constant external field E_0 induces a (orange) constant, opposing depolarization field E_P, resulting in a (purple) local field E_{loc} different from the original driving field. The colored sides of the ellipsoid represent the induced (red) positive and (blue) negative polarization charges. The depolarization factor α relates E_P to E_0 and the local field factor f_{LF} relates E_{loc} to E_0. **(b)** (color) Intensity of the electric field (increasing from blue to red) and (grey) equipotential lines in and around a dielectric sphere ($_{core} >_s$) exposed to a constant (vertical) external field. **(c)** Depolarization factor as a function of aspect ratio for a prolate ellipsoid of rotation for fields ($\alpha_\parallel$) parallel and ($\alpha_\perp$) perpendicular to the long axis of the ellipsoid.[10] The dashed line indicates the depolarization factor for a sphere.

the electrostatic problem of a dielectric ellipsoid in a homogeneous external field E_0 (see Fig. 2.1). When E_0 is parallel to a major axis of the ellipsoid, the resulting polarization P of the ellipsoid is homogeneous and parallel to E_0. Adding the resulting depolarizing field $E_P = -\alpha P/\epsilon_0$, where α is the depolarization factor, to the external field yields the resulting (homogeneous) local field E_{loc} (Fig. 2.1):

$$E_{loc} = \frac{E_0}{(1-\alpha) + \alpha\tilde{\epsilon}/\epsilon_s} = f_{LF}E_0 \tag{2.11}$$

Here we have defined f_{LF} as the ratio between the external driving field E_0 and the resulting local field E_{loc}. In the case of a dielectric sphere, α amounts to $1/3$ and f_{LF} becomes:

$$f_{LF} = \frac{3\epsilon_s}{\tilde{\epsilon} + 2\epsilon_s} \tag{2.12}$$

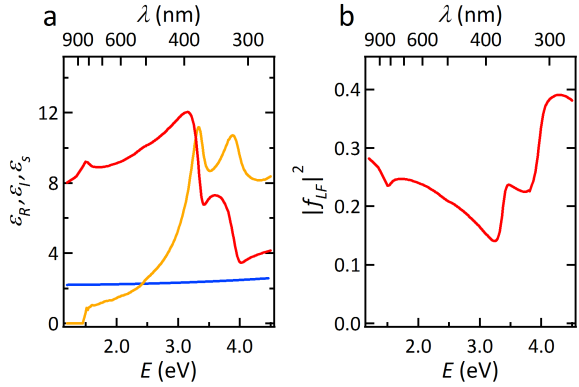

Figure 2.2: **(a)** (red) Real part $_R$ and (orange) imaginary part $_I$ of the dielectric function of CdTe and (blue) real part $_S$ of the dielectric function of toluene. **(b)** Local field factor for CdTe spheres dispersed in toluene.

Figure 2.2a shows ϵ_R and ϵ_I of CdTe,[11] together with ϵ_s of toluene. One sees that ϵ_s is considerable smaller than $|\tilde{\epsilon}|$, a typical situation for QDs dispersed in an organic solvent. Applying eq. 2.12, this implies that the local field factor is typically smaller than one, resulting in values in the range 0.15–0.4 in the case of CdTe (see Fig. 2.2b). Hence, dielectric screening will in general lead to a strong reduction of the local field inside a QD relative to an external electric field.

Returning to eq 2.10, one sees that $\epsilon_{eff,I}$ simply equals the imaginary part of the QD dielectric function ϵ_I, rescaled by the QD volume fraction f and $|f_{LF}|^2$ (local field approximation). Using the MG expressions for $\epsilon_{eff,R}$ and $\epsilon_{eff,I}$, an extinction coefficient κ_{eff} for the MG composite is obtained by considering that $\epsilon_{eff,I} = 2n_{eff}\kappa_{eff}$. Thus, eqs. 2.6 and 2.10 yield the absorption coefficient μ for a dispersion of QDs as:[12]

$$\mu = \frac{2\pi}{\lambda n_s}|f_{LF}|^2 f\epsilon_I = \frac{n}{n_s}|f_{LF}|^2 f\alpha \tag{2.13}$$

Comparing μ with the absorption coefficient α of the corresponding bulk material, we can already appreciate that the local field effect strongly modifies the absorption of a material when it is dispersed as spherical particles in another medium.

2.4 Effective medium based quantities used to describe light absorption

2.4.1 The intrinsic absorption coefficient.

Since μ increases proportionally to f, it makes sense to define an *intrinsic absorption coefficient* μ_i as:

$$\mu_i = \frac{\mu}{f} = \frac{2\pi}{\lambda n_s}|f_{LF}|_I^2 \tag{2.14}$$

As it only depends on the optical constants of the QDs and surrounding host, μ_i is a key materials property characterizing light absorption by QDs dispersed in a given solvent. As an example, Fig. 3.5 gives the absorption coefficient spectrum of bulk CdTe and of spherical particles with the dielectric function of bulk CdTe, dispersed in hexane. At low energies, a strong dielectric screening of the external electric field leads to an important reduction of the absorption as compared to bulk. Above 3 eV however, the MG effective medium theory predicts a continuous rise of the absorption with photon energy, in contrast to bulk PbS. This strong enhancement of the absorbance at high energy is related to a marked increase in f_{LF} at these energies.

Following equation 2.6, μ_i can be obtained from the measured absorbance of a sample once f is known:

$$\mu_i = \frac{\ln 10 \cdot A}{fL} \tag{2.15}$$

This is an important relation, since it shows that no information on QD size and shape is required to determine μ_i experimentally, we only need to know the total volume fraction f (i.e. the total number of atoms and the lattice constants) of the dispersed QDs. This strengthens role of μ as a starting point to quantify and understand the QD light absorption.

2.4.2 The molar absorption coefficient and absorption cross section.

For a medium composed of dispersed QDs with a concentration c, Beer's law states that A is proportional to c and the path length L. The proportionality constant is defined as the molar extinction or molar absorption coefficient ϵ:[13]

$$A = \epsilon c L \tag{2.16}$$

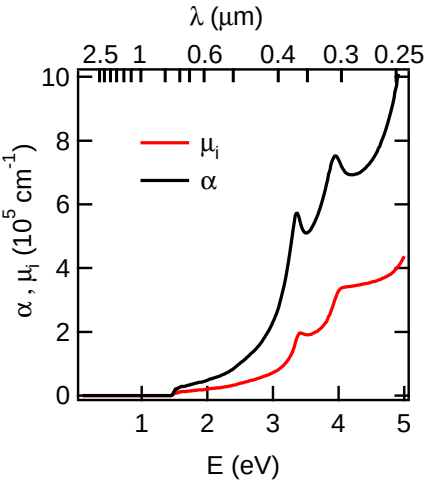

Figure 2.3: (black) Bulk absorption coefficient α_{CdTe} of bulk CdTe and (red) theoretical intrinsic absorption coefficient $\mu_{i,th,\mathrm{CdTe}}$ of nanometer sized spheres with the dielectric function of bulk CdTe dispersed in hexane.

Combining equations 2.15 and 2.16, ϵ can be related to μ_i:

$$\epsilon = \frac{\mu_i f}{\ln 10 c} = \frac{N_A V_{QD}}{\ln 10}\mu_i \tag{2.17}$$

Here, V_{QD} denotes the volume of a single QD and N_A is Avogadro's constant.

The *absorption cross section* σ of a single QD can be derived from ϵ, as the latter is correlated with the concentration of absorbers (in mol/m^{-3}), while the former is correlated with the number of absorbers per unit volume (in m^{-3}).[13] σ has units of area:

$$\sigma = \frac{\ln 10}{N_A}\epsilon = V_{QD}\mu_i \tag{2.18}$$

2.5 Quantum mechanical description of light absorption and emission

At the band-edge, the QD opto-electronic band structure consist of a discrete set of energy levels. Hence, the optical properties can be understood starting from the oscillator strength and corresponding exciton emission rate of a two-level system.

2.5.1 Rate of absorption and oscillator strength.

Most simply, quantum mechanics describes the absorption of light with an angular frequency ω as the removal of a quantum of energy $\hbar\omega$ from the radiation field, with a concomitant transition of the absorbing system from an initial state i to a final state f, with respective energies of E_i and E_f. The process is only possible if the condition $E_f - E_i = \hbar\omega$ is met. The transition rate W_{if}, *i.e.*, the transition probability per unit time, can be written as ($\mathcal{E}_{loc}(E)$, local electric field at energy $E = \hbar\omega$; $\mathbf{e}$, polarization vector of the light):[14]

$$W_{if} = \frac{e^2\pi}{\hbar} \left|\langle f|\mathbf{e}\cdot\mathbf{r}|i\rangle\right|^2 \frac{\mathcal{E}_{loc}(E)^2}{2} \tag{2.19}$$

For spherical particles dispersed in a dielectric medium, $\mathcal{E}_{loc}(E)$ is related to the spectral density $\rho_{inc}(E)$ of the incident radiation *via* the local field factor. This yields:

$$W_{if} = \frac{e^2\pi}{\epsilon_{0s}\hbar} \left|\langle f|\mathbf{e}\cdot\mathbf{r}|i\rangle\right|^2 |f_{LF}|^2 \rho_{inc}(E) = B_{if}\rho_{inc}(E) \tag{2.20}$$

Here, B_{if} represents the Einstein B coefficient of absorption. Equation 2.20 leads to an expression for the (energy integrated) absorption cross section of the transition, which corresponds to that of a dipole transition in a vacuum apart from corrections for the refractive index of the medium and the local field factor:[15]

$$\sigma_{if,\mathrm{eV}} = \frac{e\pi\omega}{3\epsilon_0 n_s c} \left|\langle f|\mathbf{r}|i\rangle\right|^2 |f_{LF}|^2 \tag{2.21}$$

The transition matrix element $\langle i|\mathbf{r}|f\rangle$ is related to the *oscillator strength* f_{if} of the transition:

$$f_{if} = \frac{2m\omega}{3\hbar} \left|\langle f|\mathbf{r}|i\rangle\right|^2 \tag{2.22}$$

The oscillator strength is a dimensionless number that compares the absorption of light by a quantum transition with a classical electronic oscillator of the same frequency. Using eq 2.22, f_{if} can be obtained from experimental data on the absorption cross section, or equivalently the intrinsic absorption coefficient. Specifically, when integrating μ_i over the QD band gap transition or first exciton peak, we obtain:

$$\mu_{i,gap,\mathrm{eV}} = \frac{e\pi\hbar}{2\epsilon_0 n_s c m} \frac{|f_{LF}|^2}{V_{QD}} f_{gap} \tag{2.23}$$

The oscillator strength of the band gap transition f_{gap} is an interesting quantity. Next to being a materials property, independent of the surrounding host, it is also closely related to the matrix element $\langle f|\mathbf{r}|i\rangle$ (equation 2.22), which forms the starting point to compare the experimentally determined f_{gap} with theoretical predictions.

2.5.2 Rate of spontaneous emission.

Similar to the absorption rate, the rate of spontaneous emission A_{fi} of a two-level system is related to f_{if} of the transition:

$$A_{fi} = \frac{e^2}{2\pi\varepsilon_0 c^3 m_e} n_s \left|f_{LF}\right|^2 \omega^2 f_{if} \tag{2.24}$$

However, for semiconductor QDs, the band gap transition generally consists of a set of closely spaced energy levels that reflect the degeneracy of the highest valence and lowest conduction QD levels. Correspondingly, f_{gap} is in reality a sum over the oscillator strengths $f_{gap,k}$ of these different exciton levels: $f_{gap} = \sum_k f_{gap,k}$. Typically, the band-edge exciton levels have a degeneracy $g = 64$ for lead chalcogenide (PbX, X=S, Se, Te) QDs, or $g = 8$ for cadmium chalcogenide (CdX) QDs. Assuming that all these band-edge exciton levels are in thermal equilibrium, the probability that an excited QD is in state $|k\rangle$ is given by Boltzmann statistics. Writing the excess energy of state $|k\rangle$ relative to the lowest energy exciton state as ΔE_k, we obtain an effective emission rate τ^{-1}:

$$\tau^{-1} = \frac{e^2}{2\pi\epsilon_0 c^3 m_e} n_s |f_{LF}|^2 \omega^2 \frac{\sum_k \exp\left(-\frac{\Delta E_k}{k_B T}\right) \cdot f_{gap,k}}{\sum_k \exp\left(-\frac{\Delta E_k}{k_B T}\right)} \tag{2.25}$$

In the high temperature limit ($k_B T \gg \Delta E_k$), equation 2.25 can be simplified into a function of f_{gap} and the degeneracy g of the first exciton level:

$$\tau^{-1} = \frac{e^2}{2\pi\varepsilon_0 c^3 m_e} n_s \left|f_{LF}\right|^2 \omega^2 \frac{f_{gap}}{g} \tag{2.26}$$

2.6 conclusions

The physical quantites defined and derived in this chapter are the tools to quantitatively describe the absorption of colloidal QDs. In the following chapters these quantities describe the cadmium based II-VI semiconductor materials. Further this analysis is extended to understand anisotropic systems like QRs and dot-in-rods.

Bibliography

[1] T. S. Rauch et al., *Near-infrared imaging with quantum-dot-sensitized organic photodiodes*, Nat. Photonics *3*, 332.

[2] J. M. Luther et al., *Schottky solar cells based on colloidal nanocrystal films*, Nano Lett. **2008**, *8*, 3488.

[3] K. W. Tang et al., *Colloidal-quantum-dot photovoltaics using atomic-ligand passivation*, Nat. Mater **2011**, *10*, 765.

[4] J. Ziegler et al., *Silica-coated InP/ZnS nanocrystals as converter material in white LEDs*, Adv. Mat. **2008**, *20*, 4068.

[5] E. Jang et al., *White-light-emitting diodes with quantum dot color converters for display backlights*, Adv. Mat **2010**, *22*, 3076.

[6] T. H. Kim et al., *Full-colour quantum dot displays fabricated by transfer printing*, Nat. Photonics **2011**, *5*, 176.

[7] I. Medintz et al., *Quantum dot bioconjugates for imaging, labelling and sensing*, Nat. Mater. **2005**, *4*, 435.

[8] J. C. Maxwell-Garnett, *Colors in metal glasses and in metallic films*, Philos. Trans. R. Soc. London **1904**, *19*, 385.

[9] J. C. Maxwell-Garnett, *Colors in metal glasses and in metallic solutions*, Philos. Trans. R. Soc. London **1906**, *19*, 237.

[10] J. A. Osborn, *Demagnetizing factors of the general ellipsoid*, Phys. Rev. **1945**, *67*, 351.

[11] S. Adachi, T. Kimura and N. Suzuki, *Optical properties of CdTe: experiment and modeling*, J. Appl. Phys. **1993**, *74*, 3435.

[12] D. Ricard, M. Ghanassi and M. C. Schanneklein, *Dielectric confinement and the linear and nonlinear-otical properties of semicondutor-doped glasses*, Opt. Commun. **1994**, *108*, 311.

[13] *IUPAC, Green Book, 2nd ed.: IUPAC Quantities, Units and Symbols in Physical Chemistry*, Blackwell Scientific Publications, Oxford **1993**.

[14] J. Weiner and H. Ping-Tong, *Light Matter Interaction*, John Wiley and Sons, New York **2003**.

[15] E. Merzbacher, *Quantum Mechanics (Wiley, New York, 1970)* .

Chapter III

Optical Properties of Zinc Blende CdTe Quantum Dots

3.1 Introduction

Absorption spectroscopy is a key technique for the characterization of colloidal nanocrystal dispersions. In the case of semiconductor nanocrystals or quantum dots (QDs), it gives access to the average QD diameter d_{QD} and the QD volume fraction f in solution. Numerous examples show that both quantities are essential for present day research activities involving colloidal QDs. Mapping the size dependence of electro-optical properties is widely used to understand QD properties and link them to theoretical modeling[1] ; the time-development of the amount of QD material formed – accessible *via* the volume fraction – is one of the starting points to analyze the kinetics and the mechanism of a QD synthesis[2]. Furthermore knowledge of QD concentrations is needed for the rational development of ligand exchange procedures[3,4] or reproducible cytotoxicity studies[5]. As a result, the availability of reliable sizing curves – linking d_{QD} to the QD band gap E_g – and absorption coefficients – enabling the calculation of QD volume fractions from an absorbance – is imperative for QD research.

Establishing experimental sizing curves typically relies on analysis of transmission electron microscopy (TEM) images. Here, operator-bias can be avoided by bringing together experimental data of different groups, as was done for CdSe[6], CdTe[6], PbSe[7] and PbS[8]. The determination of absorption coefficients (μ) is based on elemental analysis. This requires well-purified dispersions, which

can be verified by solution NMR[7]. On the other hand, an absorption coefficient determination can be checked for consistency since it was found for many materials that μ coincides with the value calculated for the bulk material using the Maxwell-Garnet model at short wavelengths[7–12]. Using this consistency check, extinction coefficients – a quantity closely related to μ – for CdSe QDs published by Yu *et al.*[13] for example where re-examined by Jasieniak *et al.*,[14] leading to considerably improved values.

Here, we present an analysis of the absorption coefficient of CdTe QDs. Together with CdSe and CdS, CdTe is one of the first materials synthesized using the hot injection approach[15]. By now, various approaches have been described to synthesize them,[16–18] control their size and shape[19] and incorporate them in heteronanocrystals[20]. Both the sizing curve[6,13] and size-dependent extinction coefficients[13] have been published. Although less widespread than CdSe, CdTe QDs are nowadays used in for example LEDs[21], bio-imaging[22] and photovoltaics[23]. Here, we combine UV-vis absorption spectroscopy, TEM imaging and elemental analysis to determine the absorption coefficients at short wavelengths and at the band gap transition. At short wavelengths, we find that size quantization is not entirely absent but still, wavelength regions exist where the absorption coefficient is size-independent and close to the bulk value. At the band gap transition, integrated absorption coefficients deviate markedly from published values and lead to largely size-independent oscillator strengths in the range 10-13. These results will strongly enhance the accuracy of volume fraction and concentration determination in future research on CdTe QDs.

3.2 Experimental

3.2.1 Synthesis

Three different procedures have been used to prepare zinc blende CdTe (zb-CdTe) QDs. For particles with a diameter of 4 to 6 nm, an adaptation of the procedure published by Dorfs *et. al.* is used[24](procedure A). The synthesis of smaller zb-CdTe QDs is based on a procedure specifically developed within the framework of this study (procedure B). The synthesis of large CdTe QDs is done by the multiple injection of precursors in the reaction mixture (procedure C), similar to what has been reported by Yu *et. al.*[13],

in collaboration with A. Omari (PCN).

Precursor preparation. In all procedures, the cadmium precursor was prepared by mixing CdO and tetradecylphosponic acid (TDPA) in a 1:3 molar ratio in a 25 mL three neck flask. After degassing the mixture for 1 h at 100 ℃ under a nitrogen flow, the CdO was dissolved under a nitrogen atmosphere at temperatures between 250 ℃ - 300 ℃ . The tellurium precursor was typically prepared by dissolving 1.5 mmol of tellurium in 10 mL of trioctylphosphine (TOP) at temperatures of about 80 ℃ and reaction time for an hour.

Procedure A: In a 25 mL three neck flask, 0.3 mmol of the Cd-TDPA precursor, 0.9 mmol of hexadecylamine (HDA) and 7.8 mL of ODE were degassed in nitrogen flow at room temperature and at 100 ℃ for 1h respectively. The temperature was raised to 280 ℃ under nitrogen atmosphere and subsequently 2 mL of a 0.022 M TOP-Te solution was injected. The temperature of the mixture was reduced and maintained at 260 ℃ for the growth of the nanocrystals. The temperature of the reacting mixture was quenched with a water bath. The product obtained was purified using toluene as the solvent and a mixture of isopropanol and methanol as the non-solvent in a nitrogen atmosphere. The purification step is repeated twice with the exception of precipitating with methanol alone. By varying the time of the reaction, CdTe QDs with sizes between 4 nm and 6 nm could be obtained.

Procedure B: A mixture of 0.2 mmol of CdO, 1 mmol of TDPA, 3.2 mmol of HDA, 2.4 mmol of steryl alcohol and 8 mL of ODE was heated up to 280 ℃ until the reaction mixture turned colorless. To this mixture, 2 mL of a 1 M TOP-Te solution was injected and the temperature was reduced to 260 ℃ for the growth of the nanocrystals. After a predefined time, the reacting mixture was quenched by injecting 5 mL of ODE. The resultant product was purified as described in the procedure A. This procedure CdTe QDs with sizes ranging from 2.8 nm to 4 nm.

Procedure C: This method makes use of the multiple injection of precursors to obtain large CdTe QDs. In a first step, similar to procedure A, a mixture of 0.3 mmol of the Cd-TDPA precursor,

0.8 mmol of HDA and 7.8 mL of ODE was heated up to 305 ℃ under nitrogen atmosphere. Next, 2 mL of a mixture of 3.8 mL of ODE, 0.7 mL of TOP and 0.1 mL of 1 M TOP-Te was injected and the growth temperature was maintained at 290 ℃ for 1 h. In a second step, additional precursors were added to the reaction mixture. For this, 4.5 mmol of the Cd-TDPA precursor was dissolved in 4 mL of ODE at 280 ℃ for 15 minutes and after cooling the mixture to 45 ℃ 1 mL of 1.5 M TOP-Te was added. Next, 2 mL of the above mixture was added with a syringe pump at a rate of 2 mL/h. Again, the reaction was quenched using a water bath and the product was purified in the same way as described in the procedure A.

The resultant nanocrystals were all washed three times and resuspended in toluene and stored in the dark in the glovebox in nitrogen atmosphere for four weeks. This was followed up by centrifugation and filtering (using 0.22 μm filter) to remove possible excess unreacted precursors and byproducts to ensure the pristine quality of nanocrystals in determining their optical properties.

3.2.2 Size determination.

The mean diameter d_{QD} of the CdTe QDs was determined from bright field TEM images recorded with a Cs corrected JEM-2200FS transmission electron microscope. The samples for TEM were prepared by drop casting a dilute suspension of CdTe QDs on a holey carbon film supported by a copper TEM grid. To improve the contrast, a high contrast aperture with Z-filter has been used. Based on the TEM images, the size histogram, mean diameter and size dispersion of the QDs has been determined by analyzing 100–150 particles for each sample.

3.2.3 Absorption coefficient determination.

Absorption coefficients were determined by combining elemental analysis with UV-vis absorption spectroscopy. The concentration of Cd was determined by inductively coupled plasma mass spectrometry (ICP-MS). This measurement and analysis was done at department of analytical chemisrty, Ghent University, by Karen Van Hoecke and prof. Frank Vanhaecke. ICP-MS samples were prepared by drying a known amount of CdTe QD suspension in a

nitrogen flow. The dried samples were digested in 500 μL of HNO_3 to be analyzed with a Perkin Elmer SCIEX elan 5000 ICP-MS. The Cd:Te ratio R is determined using Rutherford backscattering (RBS). This measurement and analysis was done at institute for nuclear and radiation physics, K.U.Leuven, by Qiang Zhao and prof. Andre Vantomme. RBS samples consisted of 10-15 nm thick films of CdTe QDs spin coated on Si substrates. The measurements were done with a 4 MeV He^+ ion beam and a NEC 5SDH-2 Pelletron tandem accelerator with a semiconductor detector at backscattering angles of 165° and 167.6°. For the absorption measurements, and identical amount of CdTe QDs as used for ICP-MS was dried under nitrogen flow and redispersed in toluene. The absorbance spectrum of the resulting dispersion was recorded with a Perkin Elmer Lambda 950 UV-vis spectrophotometer. Optical characterization by luminescence spectroscopy and time resolved photoluminescence spectroscopy was measured by Pieter Geiregat in collabration with prof. Rik Van Deun, coordination group, Ghent University. The measurements were done with Edinburgh instruments FLS90 spectrofluorimeter, using a Nd:YAG laser at 410 nm and a repetition rate of 18 MHz as the excitation source.

3.3 Results and discussion

3.3.1 Material characterization

Figure 3.1 gives the basic characteristics of 5.7 nm CdTe QDs synthesized following procedure 1. The TEM overview image (Fig. 3.1a) demonstrates that the resulting CdTe QDs are quasi-spherical with a narrow size dispersion of around 4% (Fig.3.1b). According to the x-ray diffractogram (Fig. 3.1c), the QDs used here have the zinc blende crystal structure and similar to PbSe, PbS and CdSe QDs,[7,8,25] the RBS spectrum shows that they are cation rich, with a Cd:Te ratio R of 1.10 in this case. As shown in Tab 3.1, these conclusions hold for all sizes. Only for the largest QDs ($8-10$ nm), crystal facets are more pronounced and the size dispersion increases to about 8%.

Figure 3.2a shows the UV-vis absorption spectra of 6 different batches of CdTe QDs. For all samples, the wavelength λ_{1S-1S} of the first exciton transition can be readily determined. Combining the resulting λ_{1S-1S} with TEM overview images of the different samples enables us to construct the CdTe sizing curve, which re-

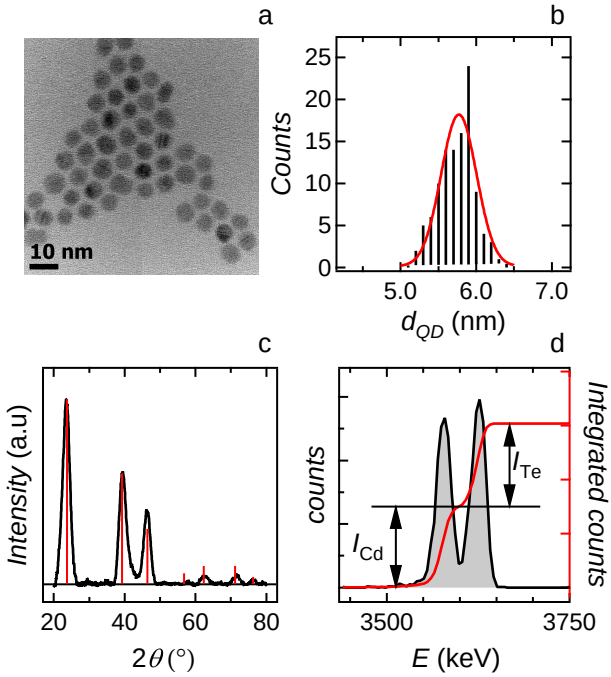

Figure 3.1: Basic characterization of 5.7 nm CdTe QDs synthesized according to procedure 1. (a) TEM overview image. (b) Size histogram, yielding a size dispersion of 4%. (c) (black line) XRD pattern of the CdTe QDs and (red bars) the reference diffractogram of zinc blende CdTe. (d) RBS spectrum indicating the backscattered intensity for Cd (I_{Cd}) and Te (I_{Te}), yielding a Cd:Te ratio of 1.10.

lates the band gap E_g – as calculated from λ_{1S-1S} – to d_{QD}. Figure 3.2b plots the different data points we obtain and compares them with sizing curves published before by Yu *et al.* and Donega *et al.*.[6,13] A good correspondence is overall obtained with the latter, with maximum deviations of about 0.3 nm. On the other hand, deviations up to 0.6 nm are found with the sizing curve of Yu *et al.*, especially in the range $d_{QD} = 3.5 - 6.5\,\mathrm{nm}$. Taking a value of 1.51 eV for the band gap of bulk CdTe,[26] we use the following best fit to our experimental data to link E_g to d_{QD} (black line in Fig. 3.2b):

$$E_0(d) = 1.51 + \frac{1}{0.048d^2 + 0.29d - 0.09} \tag{3.1}$$

We use the labels S1 to S12 to identify the different CdTe QD

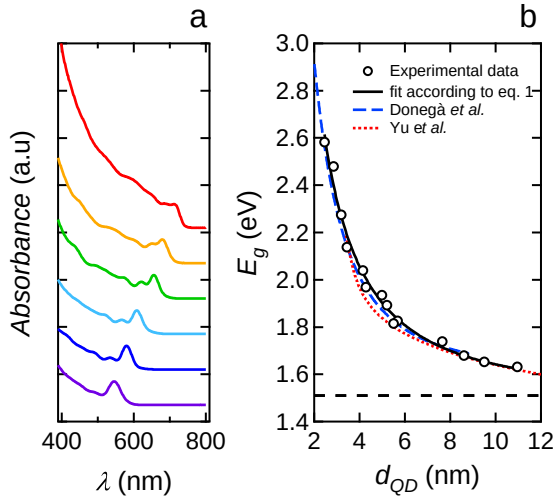

Figure 3.2: (a) Absorption spectra of QDs with diameter d_{QD} of (top to bottom) 7.65, 5.67, 5.20, 4.14, 3.73 and 3.19 nm.(b) Relation between CdTe QD band gap E_g and d_{QD}, including (markers) experimental data obtained here, (black) best fit according to 3.1, (red) sizing curve of Yu *et al.*[13] and (blue) sizing curve of Donega *et al.*[6].

batches used for the construction of the sizing curve. Figures 3.3 and 3.4 show TEM images of these different samples, together with a size histogram, the average diameter and the size dispersion.

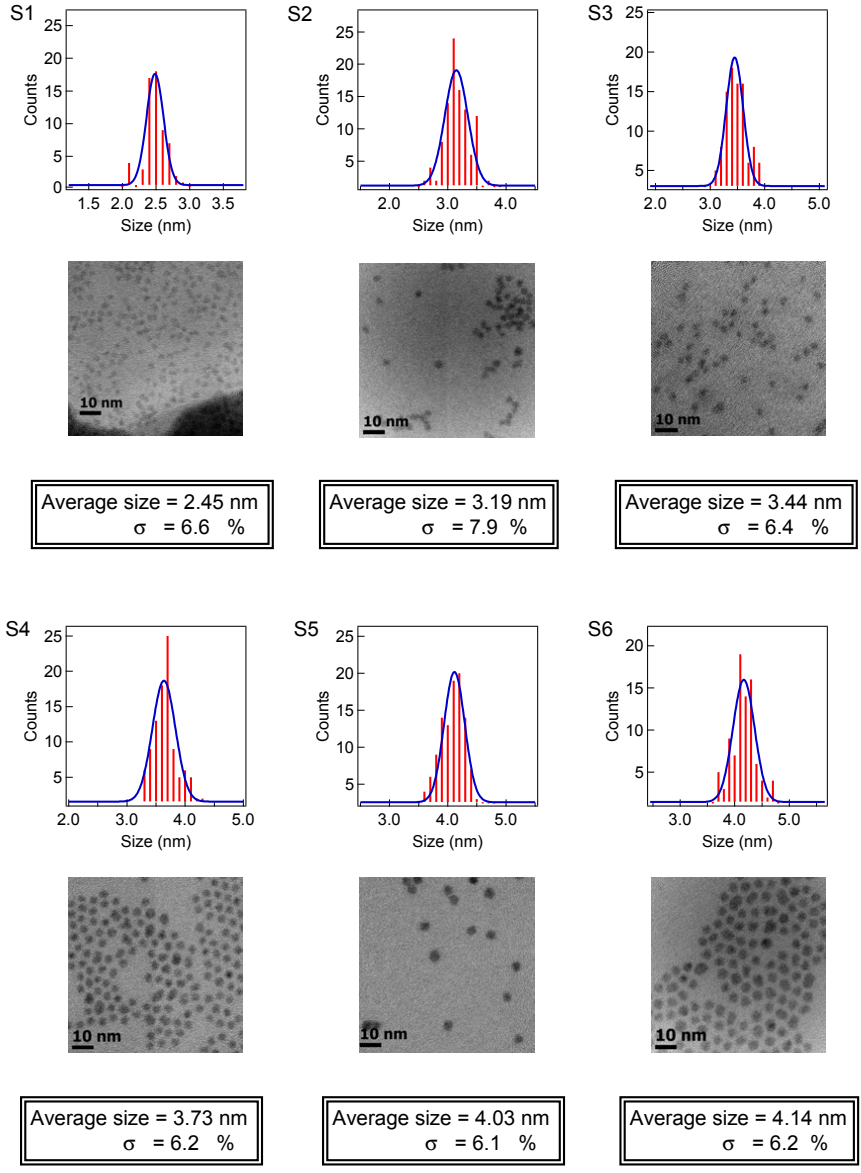

Figure 3.3: Size histogram and TEM images of samples S1-S6.

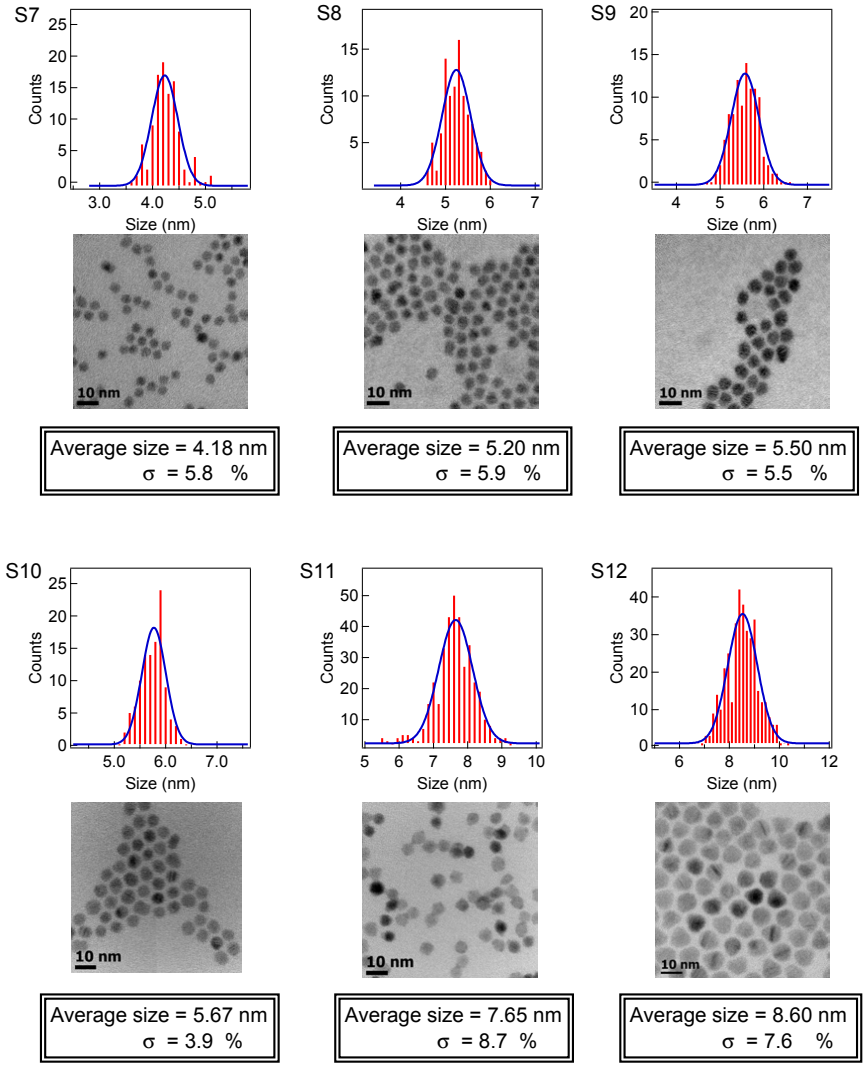

Figure 3.4: Size histogram and TEM images of samples S7-S12.

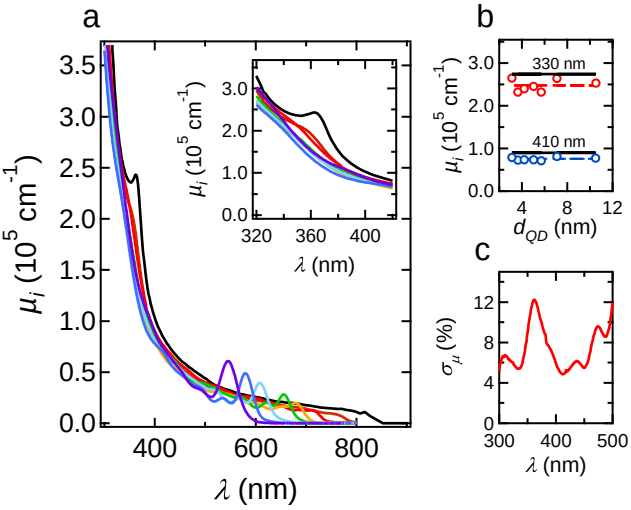

Figure 3.5: (a) Intrinsic absorption coefficient (μ_i) spectra of CdTe QDs of different sizes in toluene and (black line) intrinsic absorption coefficient (μ_{ith}) calculated for bulk CdTe according to *Eq.*3.4. (inset) zoom of the short wavelength range of the μ_i spectra. (b) μ_i at (blue markers) 410 nm and (red markers) 330 nm as a function of the CdTe QD diameter, together with (dashed lines) the respective average μ_i and (black lines) the corresponding bulk value. (c) Relative standard deviation on μ_i as a function of wavelength calculated using the 7 spectra shown in (a).

3.3.2 The intrinsic absorption coefficient at short wavelengths.

We quantify the absorbance of dispersed colloidal QDs in the first place by the intrinsic absorption coefficient μ_i, which relates the measured absorbance A of a QD dispersion to the QD volume fraction f in the dispersion:

$$\mu_i = \frac{\ln(10)A}{fL} \tag{3.2}$$

An advantage of using μ_i is that its value does not depend on the QD sizing curve, which means that f can be determined irrespective of errors on the size determination. This is important since knowledge of f often suffices to characterize a QD dispersion, for instance to determine the yield development of a QD synthesis. For CdTe QDs, f is related to the molar concentrations of Cd

(C_{Cd}) and Te (C_{Te}) according to (a: lattice parameter of CdTe zincblende unit cell):

$$f = \frac{a^3}{8} N_A \left(C_{\mathrm{Cd}} + C_{\mathrm{Te}}\right) = \frac{a^3}{8} N_A C_{\mathrm{Cd}} \left(1 + \frac{1}{R}\right) \tag{3.3}$$

As outlined in the methods section, we obtain C_{Cd} using ICP-MS and R using RBS measurements (Table 3.1 shows ICP-MS and RBS results). Figure 3.5a shows 7 different μ_i spectra determined by combining elemental analysis (yielding f) and absorption spectroscopy (yielding A) in toluene.

Label	Diameter (nm)	Cd(mmol/l)	$R_{Cd:Te}$	A_{410}	f (10^{-6})
S2	3.19	0.99	1.39	0.199	5.82
S4	3.73	2.10	1.13	0.429	1.35
S6	4.14	4.30	1.20	0.286	8.98
S8	5.20	2.27	1.14	0.466	14.56
S10	5.67	1.10	1.09	0.221	72.03
S11	7.65	0.87	1.12	0.297	8.45
S13	10.97	1.09	1.07	0.360	10.71

Table 3.1: Overview of the ICP-MS results of CdTe QD in combination with the RBS data on ratio of Cd:Te and reference absorbance at 410 nm (A_{410}), and the resulting volume fraction (f) of CdTe QDs .

Similar to previous studies on various QDs,[7–12] we find that the μ_i spectra tend to coincide at short wavelengths, especially in the wavelength ranges around 400 and below 340 nm. In the literature, this has always been interpreted as an absence of quantum confinement effects on higher energy conduction and valence band states. Moreover, excellent correspondence has been demonstrated between the experimental μ_i and a theoretical value $\mu_{i,th}$ calculated within the Maxwell-Garnett effective medium theory,[27] using the bulk dieletric function $\varepsilon_R + i\varepsilon_I$ of the QD material:

$$\mu_{i,th} = \frac{2\pi}{n_s \lambda} \left|f_{LF}\right|^2 \varepsilon_I \tag{3.4}$$

Here, n_s is the refractive index of the solvent and f_{LF} is the local field factor, *i.e.*, the ratio between the electric field outside and inside the QD. For spherical QDs, f_{LF} is given by ($\varepsilon_s = n_s^2$):

$$f_{LF} = \frac{3\varepsilon_s}{\varepsilon_R + i\varepsilon_I + 2\varepsilon_s} \tag{3.5}$$

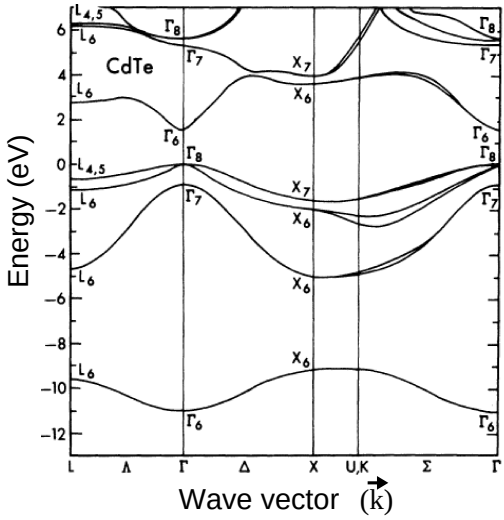

Figure 3.6: Band structure of bulk CdTe.

The bulk $\mu_{i,th}$ reference spectrum for CdTe in toluene is shown as the black line in Fig. 3.5. It clearly reproduces the overall increase of μ_i with decreasing wavelength and the wavelength regions where all μ_i spectra tend to coincide – around 410 and 320 nm – correspond to wavelengths where the bulk spectrum does not show particular features. Figure 3.5b shows $\mu_{i,410}$ and $\mu_{i,330}$ as a function of d_{QD}. One sees that both values are largely size-independent with an average value lower than $\mu_{i,th}$ by 16% and 24%, respectively. A similar deviation was found with zb-CdSe at wavelengths below 350 nm.[12]. As shown in Fig. 3.5c, the standard deviation on μ_i is lowest in the wavelength range 405–420 nm. Therefore, we propose to use the average absorption coefficient $\mu_{i,410}$ as obtained here for the determination of CdTe QD volume fractions in toluene dispersions:

$$\mu_{i,410} = 75500\,\mathrm{cm}^{-1} \tag{3.6}$$

The intrinsic absorption coefficient of bulk CdTe shows a pronounced feature at 365 nm, which corresponds to the E_1 transition that connects initial and final states along the Λ direction in the Brillouin zone (see Fig. 3.6).[28,29] Figure 3.5 shows that this feature is not present in the μ_i spectra of the smaller CdTe QDs. Only for the largest sizes, a shoulder develops in this wavelength range, which becomes more pronounced and shifts from shorter

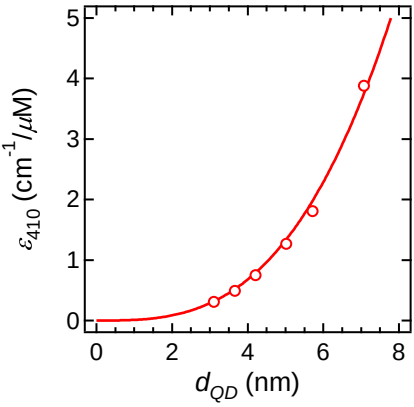

Figure 3.7: Representation of (markers) the molar extinction coefficient of CdTe QDs in toluene at 410 nm as a function of QD diameter and (full line) the cubic fit according to *Eq.*3.8.

wavelengths towards 365 nm with increasing size. This is a clear indication of size quantization effects in this particular region of the Brillouin zone, similar to what was found for the E_1 transition along the Σ direction in PbSe QDs[30,31]. Importantly, this persistence of size-quantization effects implies that normalization of CdTe QD spectra for relative comparison is only viable at those wavelengths where size effects on the absorption coefficient are minimal, *i.e.*, around 410 or 320 nm, respectively.

The molar extinction coefficient ϵ of dispersed colloidal CdTe QDs is obtained by making the product of μ_i and the volume of 1 mole of QDs:

$$\epsilon = \frac{\pi d_{QD}^3 N_A}{6\ln(10)}\mu_i \tag{3.7}$$

Since $\mu_{i,410}$ is independent of d_{QD}, we obviously find that ϵ_{410} scales proportionally to d_{QD}^3 (see Fig. 3.7). Writing d_{QD} in nanometer, a best fit to the experimental data yields (ϵ_{410} in cm^{-1}/μM):

$$\epsilon_{410} = 0.0105 \times d_{QD}^3 \tag{3.8}$$

3.3.3 The intrinsic absorption coefficient at the bandgap

In the literature, absorption or extinction coefficients are often reported at the band gap transition, typically in combination with a normalization procedures to account for peak broadening due to size dispersion.[13,32] A useful quantity in this respect is the energy integrated absorption coefficient $\mu_{i,gap}$ of the first exciton transition. This can be obtained either by using μ_i spectra obtained by determining f using elemental analysis (see Fig. 3.5) or by normalizing absorption spectra using the average value of $\mu_{i,410}$. In this way, $\mu_{i,gap}$ follows from the integrated absorbance A_{gap} of the first exciton absorbance peak:

$$\mu_{i,gap} = \frac{A_{gap}}{A_{410}} \mu_{i,410} \tag{3.9}$$

Typically, $\mu_{i,gap}$ is calculated by doubling the integrated low energy half of the first exciton peak.[7]

Figure 3.8 shows the resulting $\mu_{i,gap}$ obtained with both procedures. Opposite from $\mu_{i,410}$, $\mu_{i,gap}$ shows a marked increase with decreasing particle size. Since μ_i gives an absorbance per unit volume of material, this shows that for the same volume of CdTe, small QDs absorb more light at their bandgap transition than large QDs. The dependence of $\mu_{i,gap}$ on d_{QD} in the size range envisaged here ($3-10\,\mathrm{nm}$) can be well fitted to a power law. A best fit shows that $\mu_{i,gap}$ is about proportional to the inverse of the QD volume:

$$\mu_{i,gap} = 2.68\,10^7 \times d^{-2.75}\ (\mathrm{eVm}^{-1}) \tag{3.10}$$

Extinction coefficients at the band gap have been published before for CdTe QDs by Yu *et al.*.[13] In order to compare these results with the data obtained here, we have combined the extinction coefficients and the sizing curve of these authors to calculate a $\mu_{i,gap}$. To do this, ϵ values of Yu *et al.* are first converted to wavelength integrated molar extinction coefficient $\epsilon_{gap,\lambda}$ by normalizing the ϵ values by the reported standard peak width of 36 nm. The deduced $\epsilon_{gap,\lambda}$ values can be readily transformed into energy integrated molar extinction coefficient $\epsilon_{gap,eV}$ by the relation:

$$\epsilon_{gap,eV} = \frac{eE_0(d)^2}{hc} \epsilon_{gap,\lambda} \tag{3.11}$$

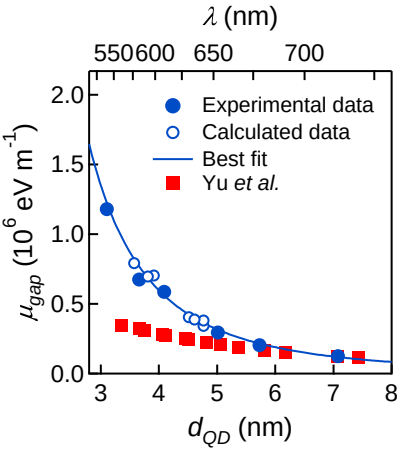

Figure 3.8: The energy integrated intrinsic absorption coefficient μ_{gap} as a function of QD diameter (bottom axis, calculated according to *Eq.*3.1) and λ_{1S-1S} (top axis), showing data obtained by (filled blue circles) elemental analysis and (open blue circles) normalization of mu_i at 410 nm. The blue line is a best fit according to 3.10 and the red squares represent the data according to Yu *et al.*.[13]

The resulting value of ϵ_{gap} is then used to calculate $\mu_{i,gap}$ as a function of size using Yu *et al.*'s expression for the sizing curve:

$$\mu_{i,gap} = \frac{6ln(10)}{\pi d^3 N_A}\epsilon_{gap} \tag{3.12}$$

Figure 3.8 gives the resulting values as a function of λ_{1S-1S} (upper horizontal axis) and d_{QD} calculated according to the sizing curve proposed here (lower horizontal axis). Depending on the actual size, the resulting $\mu_{i,gap}$ according to Yu *et al.* is up to 3 times smaller than the values reported here. Since our values correspond to a $\mu_{i,410}$ that is within 16% of the bulk value, we conclude that the use of the extinction coefficients proposed by Yu *et al.* for volume fraction and concentration determination of CdTe QD dispersions may give considerable errors and is therefore not recommended.

3.3.4 Oscillator strength and lifetime

The oscillator strength of an electronic transition from an initial (i) to a final (f) state compares the power absorbed by the electronic

transition to that of a classical dipole oscillator with the same resonance frequency. It is an intrinsic property of an electronic transition – closely related to the $i \rightarrow f$ transition dipole matrix element. The oscillator strength f_{exc} related to the first exciton transition can be calculated from the experimental $\mu_{i,gap}$ according to (ϵ_0: permittivity of the vacuum; c: speed of light; m_e: electron mass; $\hbar$: Planck's constant):[7]

$$f_{exc} = \frac{2\epsilon_0 n_s c m_e}{e\pi\hbar} \frac{1}{|f_{LF}|^2} \frac{\pi d_{QD}^3}{6} \mu_{i,gap} \tag{3.13}$$

Figure 3.9(a) shows the resulting f_{exc} as a function of d_{QD} calculated using the bulk dielectric function of CdTe at the wavelength of the respective band gap transition. As could be expected from the almost cubic dependence of $\mu_{i,gap}$ on $1/d_{QD}$, f_{if} is largely constant in the diameter range $3-7\,\mathrm{nm}$, varying only between 10 and 13. In this respect CdTe QDs differ significantly from CdSe QDs, where the oscillator strength shows a pronounced size dependence and drops to values of around 5 in the $2-4\,\mathrm{nm}$ size range.[12]. On the other hand, a similar size-independent oscillator strength was found for InAs QDs.[10]

The oscillator strength of an electronic transition is related to the decay rate τ^{-1} of the excited state by spontaneous emission. Summing over all accessible exciton states j – presumed to be in thermal equilibrium – τ^{-1} reads (k_B: Boltzmann's constant; T: absolute temperature):

$$\tau^{-1} = \frac{e^2}{2\pi\epsilon_0 c^3 m_e} n_s |f_{LF}|^2 \omega^2 \frac{\sum_j f_{ij} e^{-\frac{\Delta\epsilon_{ij}}{k_B T}}}{\sum_j e^{-\frac{\Delta\epsilon_{ij}}{k_B T}}} \tag{3.14}$$

Here, $\Delta\epsilon_{ij}$ denotes the energy difference between the exciton state j and the lowest energy exciton state. When $\Delta\epsilon_{ij} \ll k_B T$, the spontaneous emission rate can be rewritten as (g: total number of exciton states accessible):

$$\tau^{-1} = \frac{e^2}{2\pi\epsilon_0 c^3 m_e} n_s |f_{LF}|^2 \omega^2 \frac{\sum_j f_{ij}}{g} = \frac{e^2}{2\pi\epsilon_0 c^3 m_e} n_s |f_{LF}|^2 \omega^2 \frac{f_{exc}}{g} \tag{3.15}$$

Figure 3.9(b) plots the resulting predicted lifetime τ, calculated taking $g = 8$,[34] together with experimental data measured on samples (S4–S5) and literature data[33]. Experimental life times

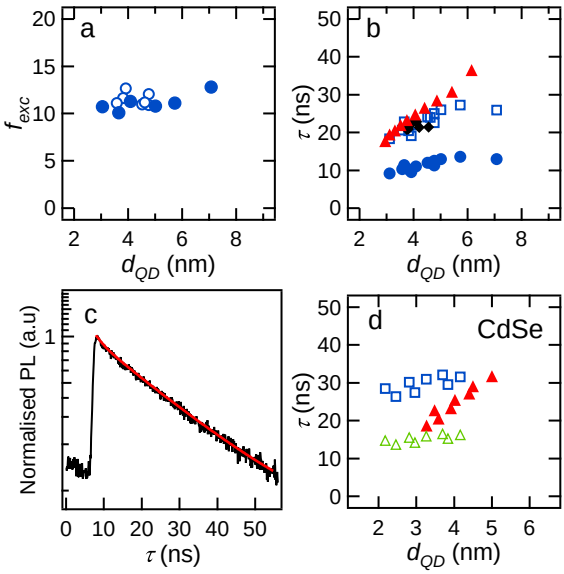

Figure 3.9: (a) Oscillator strength f_{exc} of the first exciton transition in CdTe QDs, based on (filled blue circles) elemental analysis and (open circles) normalization of μ_i at 410 nm. (b) Spontaneous emission lifetime calculated according to *Eq.*3.15 using (filled blue circles) $g = 8$ and (open blue squares) $g = 16$ and (filled red triangles) experimental data according to Van Driel *et al.*.[33].(c) Representation of (black) time-resolved photoluminescence trace of CdTe QDs and (red) best fit using a single exponential decay funtion. (d) Spontaneous emission lifetime of CdSe QDs calculated according to *Eq.*3.15 (open blue squares) $g = 16$, (open green triangles)$g = 8$ and (filled red triangles) experimental data according to Van Driel *et al.* or (black markers) measured on samples S4 and S5.[33].

were obtained by time-resolved photoluminescence measurements (see Fig. 3.9c), which could be fitted to a single exponential.

In the diameter range $3-7$ nm, the predicted lifetimes slightly increase from 9 to 13 ns with increasing d_{QD}. These lifetimes are 2 to 3 times smaller than the experimental ones, which range from about 20 to 40 ns over the same diameter range. An explanation of this difference could be that instead of an equal occupation probability of all 8 exciton levels, a dark exciton state is preferentially occupied. However, opposite of the data shown in Fig.3.9b, this should lead to a better correspondence between predicted and measured lifetimes for larger QDs, which have a concomitantly lower energy splitting between the different exciton

levels. Alternatively, the measured lifetimes will exceed the predicted values when additional dark exciton states, not accounted for in the $g = 8$ assumption, are accessible. This is not unlikely given the small energy spacing between the $1S_{3/2}$ and $1P_{3/2}$ hole states[35], which would mean that a manifold of 16 instead of 8 exciton states are readily accessible for the first exciton. As shown in Fig. 3.9b, the assumption of $g = 16$ leads to an excellent correspondence between measured and predicted lifetimes, especially for the smaller sizes.

To substantiate this argument, we extended this approach to CdSe QDs, where a lifetime can also be predicted based on oscillator strengths found in literature[12]. In this case, the measured data seemingly fit in between the predicted lifetimes based on $g = 8$ and $g = 16$. This suggests that for the smallest sizes, only the $1S_{3/2}$ hole states are accessible to the exciton. With increasing size, also higher energy hole states – most likely the $2S_{3/2}$ states[36] – can be occupied at room temperature, raising the effective degeneracy to 16.

3.4 Conclusions

We have analyzed the basic optical properties – sizing curve, absorption coefficient, oscillator strength of the band gap transition – of CdTe QDs by combining UV-vis absorption spectroscopy, TEM, ICP-MS and RBS measurements. At 410 nm, we retrieve a largely size-independent intrinsic absorption coefficient μ_i. The resulting value is close to what is expected for bulk CdTe and can be used for determining the volume fraction of spherical CdTe QDs in colloidal dispersions. Despite the size-independent μ_i at 410 nm, we observe persistent quantum confinement effects on the E_1 transition, which appears less pronounced and blueshifted in CdTe QDs relative to its bulk value of 365 nm.

Around the band gap, we find an integrated absorption coefficient μ_{gap} that scales proportionally to the inverse of the QD volume. Especially for the smaller diameters, significant deviations are found as compared to widely used literature values. The corresponding oscillator strength f_{exc} is almost size-independent in the diameter range 3–7 nm. Radiative lifetimes predicted based on f_{exc} are in line with experimental results and published values if a 16-fold degeneracy for the first exciton is assumed.

Bibliography

[1] V. Klimov, editor, *Semiconductor and Metal Nanocrystals, Synthesis and Electronic and Optical Properties*, Marcel Dekker: New York **2004**.

[2] S. Abe et al., *Tuning the postfocused size of colloidal nanocrystals by the reaction rate: from theory to application*, ACS Nano **2012**, *6*, 42–53.

[3] D. V. Talapin, J.-S. Lee and E. V. Kovalenko, M. V.and Shevchenko, *Prospects of colloidal nanocrystals for electronic and optoelectronic applications*, Chem. Rev. **2010**, *110*, 389458.

[4] J. S. Owen et al., *Reaction Chemistry and Ligand Exchange at Cadmium-Selenide Nanocrystal Surfaces*, J. Am. Chem. Soc. **2008**, *130*, 12279–12281.

[5] S. J. Soenen et al., *Cellular toxicity of inorganic nanoparticles: common aspects and guidelines for improved nanotoxicity evaluation*, Nano Today **2011**, *6*, 446465.

[6] C. de Mello Doneg and R. Koole, *Size dependence of the spontaneous emission rate and absorption cross section of CdSe and CdTe quantum dots*, J. Phys. Chem. C **2009**, *113*, 6511–6520.

[7] I. Moreels et al., *composition and size-dependent extinction coefficient of colloidal PbSe quantum dots*, Chem. Mater. **2007**, *19*, 6101–6106.

[8] I. Moreels et al., *Size-dependent optical properties of colloidal PbS quantum dots*, ACS nano **2009**, *3*, 3023–3030.

[9] C. A. Leatherdale et al., *On the absorption cross section of CdSe nanocrystal quantum dots*, J. Phys. Chem. B **2002**, *106*, 7619–7622.

[10] P. Yu et al., *Absorption cross-section and related optical properties of colloidal InAs quantum dots.*, J. Phys. Chem. B **2005**, *109*, 7084–7087.

[11] P. Lommens et al., *The growth of Co:ZnO/ZnO core/shell colloidal quantum dots: changes in nanocrystal size, concentration and dopant coordination.*, ChemPhysChem **2008**, *9*, 484–491.

[12] K. R. Capek et al., *Optical properties of zincblende cadmium selenide quantum dots*, J. Phys. Chem. C **2010**, *114*, 6371–

6376.

[13] W. W. Yu et al., *Experimental Determination of the Extinction Coefficient of CdTe, CdSe, and CdS Nanocrystals*, Chem. Mater. **2003**, *15*, 2854–2860.

[14] J. Jasieniak et al., *Re-examination of the size-dependent absorption properties of CdSe quantum Dots*, J. Phys. Chem. C **2009**, *113*, 19468–19474.

[15] C. B. Murray, D. J. Norris and M. G. Bawendi, *Synthesis and characterization of nearly monodisperse CdE (E = sulfur, selenium, tellurium) semiconductor nanocrystallites*, J. Am. Chem. Soc. **1993**, *115*, 8706–.

[16] Z. A. Peng and X. Peng, *Formation of high-quality CdTe, CdSe, and CdS nanocrystals using CdO as precursor.*, J. Am. Chem. Soc. **2001**, *123*, 183–184.

[17] D. V. Talapin et al., *A novel organometallic synthesis of highly luminescent CdTe nanocrystals*, J. Phys. Chem. B **2001**, *105*, 2260–2263.

[18] S. F. Wuister et al., *Highly luminescent water-soluble CdTe quantum dots*, Nano Lett. **2003**, *3*, 503–507.

[19] W. W. Yu, Y. A. Wang and X. Peng, *Formation and stability ofsize-, shape-, and structure-controlled CdTe nanocrystals: ligand effects on monomers and nanocrystals*, Chem. Mater. **2003**, *15*, 4300–4308.

[20] S. Kim et al., *Type-II quantum dots: CdTe/CdSe(core/shell) and CdSe/ZnTe(core/shell) heterostructures.*, J. Am. Chem. Soc. **2003**, *125*, 11466–11467.

[21] Y. W. Lin, W. L. Tseng and H. T. Chang, *Using a layer-by-layer assembly technique to fabricate multicolored-light-emitting films of CdSe@CdS and CdTe quantum dots*, Adv. Mater. **2006**, *18*, 1381–1386.

[22] X. Michalet et al., *Quantum dots for live cells, in vivo imaging, and diagnostics.*, Science **2005**, *307*, 538–544.

[23] J. H. Bang and P. V. Kamat, *Quantum dot sensitized solar cells. A tale of two semiconductor nanocrystals: CdSe and CdTe.*, ACS nano **2009**, *3*, 1467–1476.

[24] D. Dorfs et al., *Type-I and type-II nanoscale heterostructures based on CdTe nanocrystals: a comparative study.*, Small **2008**, *4*, 1148–1152.

[25] B. Fritzinger et al., *Utilizing self-exchange to address the bind-*

ing of carboxylic acid ligands to CdSe quantum dots., J. Am. Chem. Soc. **2010**, *132*, 10195–10201.

[26] P. Horodysky and P. Hlidek, *Free-exciton absorption in bulk CdTe: temperature dependence*, Phys. Status Solidi B **2006**, *243*, 494–501.

[27] D. Ricard, *Dielectric confinement and the linear and nonlinear optical properties of semiconductor-doped glasses*, Opt. Comm. **1994**, *108*, 311–318.

[28] J. R. Chelikowsky and M. L. Cohen, *Nonlocal pseudopotential calculations for electronic-structure of eleven diamond and zinc-blende semiconductors*, Phys. Rev. B **1976**, *14*, 556–582.

[29] S. Adachi, T. Kimura and N. Suzuki, *Optical properties of CdTe: experiment and modeling*, J. Appl. Phys. **1993**, *74*, 3435.

[30] Z. Hens et al., *Effect of quantum confinement on the dielectric function of PbSe*, Phys. Rev. Lett. **2004**, *92*, 3–6.

[31] R. Koole et al., *Optical investigation of quantum confinement in PbSe nanocrystals at different points in the brillouin zone.*, Small **2008**, *4*, 127–133.

[32] L. Cademartiri et al., *Size-dependent extinction coefficients of PbS quantum dots.*, J. Am. Chem. Soc. **2006**, *128*, 10337–10346.

[33] A. van Driel et al., *Frequency-dependent spontaneous emission rate from CdSe and CdTe nanocrystals: influence of dark states*, Phys. Rev. Lett. **2005**, *95*, 1–4.

[34] A. Efros et al., *Band-edge exciton in quantum dots of semiconductors with a degenerate valence band: dark and bright exciton states.*, Phys. Rev. B **1996**, *54*, 4843–4856.

[35] A. Efros and M. Rosen, *Quantum size level structure of narrow-gap semiconductor nanocrystals: Effect of band coupling*, Phys. Rev. B **1998**, *58*, 7120–7135.

[36] D. J. Norris and M. G. Bawendi, *Measurement and assignment of the size-dependent optical spectrum in CdSe quantum dots*, Phys. Rev. B **1996**, *53*, 16338.

Chapter IV

Absorption anisotropy in CdSe and CdS quantum rods

4.1 Introduction

Literature studies confirm that the absorption coefficient μ of colloidal QDs can be understood within the framework of the Maxwell Garnett effective medium theory. This implies that the screening of the electric field by the QD, as expressed by the local field factor f_{LF}, is an essential factor determining μ (local field approximation). The local field approximation has also been applied to 1D nanowires, where it predicts that μ takes different values for light polarized parallel ($\mu_{\parallel}$) and perpendicular ($\mu_{\perp}$) to the long axis of the wire. In the case of InP nanowires (NWs), the observation of polarized emission and emission excitation has been accordingly interpreted in terms of anisotropic local field factors.[2] In addition, it has been shown for CdSe and CdTe NWs that absorption anisotropy leads to an enhanced absorption coefficient even if the wires are randomly dispersed.[3,4] Rod-like colloidal semiconductor nanocrystals combine the properties of both QDs and nanowires. Like QDs, they are considerably smaller than the wavelength of light, such that the local field approximation applies, and similar to nanowires, they have anisotropic optical properties.[5] Polarized emission and emission excitation have been demonstrated by single rod measurements on CdSe QRs[6]. Opposite to the emission properties, experimental data on the absorption anisotropy of colloidal QRs and their possible correspondence to the predictions of the local field approximation are rare. In the studies that address

QR absorption, the local field approximation is either assumed to hold[7] or the possibility of absorption anisotropy is not addressed[8]. This gap in the literature forms the starting point for this investigation, which is is carried out in three steps:

- Developing an experimental method to determine the absorption coefficient anisotropy of colloidal quantum rods.
- Analysis of absorption anisotropy of single component CdSe and CdS quantum rods.
- Determination of absorption coefficients of randomly dispersed quantum rods and interpretation of the results in terms of absorption anisotropy.

The first objective is achieved by combining absorption spectroscopy with the alignment of quantum rods in solution by means of electric fields. The second objective involves the synthesis of CdSe and CdS QRs of different aspect ratio and analyzing them using the setup developed. The third objective involves the combination of elemental analysis using ICP-MS, imaging using TEM, and UV-vis absorption spectroscopy.

4.2 Synthesis

For the present work five different aspect ratios of CdSe rods (sample —S1-S5) were synthesised and a single sample of CdS rods (sample S6) was made following the procedures outlined below.

Procedure 1: Sample S1 and S3 were synthesised according to a slightly modified literature procedure reported by Gur et al.[9]. According to this procedure in a 25 mL flask a mixture of 0.71 g of tetradecylphosphonic acid (TDPA), 0.16 g of hexylphosphonic acid (HPA), 3 g of trioctylphosphine oxide (TOPO) and CdO were heated under vacuum at 120 ℃ for 1 h in the schlenk line, subsequently the mixture is heated upto 300 ℃ under nitrogen atmosphere. To this reaction mixture 0.489 g of trioctylphosphine selenide (TOP-Se) (1.16 g Se is dissolved in 7.2 g TOP at 80 ℃ for half an hour on stirring) is swiftly injected with a syringe. This results in drop in temperature of the reaction mixture to 280 ℃ and this growth temperature is maintained till the end of the reaction.

The reaction was quenched after desired time and 5 mL of toluene is added. The CdSe QRs thus obtained are purified by addition of 5 mL of isopropanol as a non-solvent. The precipitated QRs are recovered by centrifugation and decantation. The remaining QR pellet is then resuspended in toluene and the purification is repeated twice to have pristine quality of QRs.

Procedure 2. Samples S2 and S4 were synthesized according to a modified literature procedure[10]. A mixture of 0.086 g of CdO, 3.00 g of TOPO, 0.29 g of octadecylphosphonic acid (ODPA) and 0.08 g of HPA was degassed under vacuum at 120 ℃ for 1 hour. Next, the mixture was heated to 350 ℃ under a nitrogen atmosphere and a mixture of 0.12 g Se dissolved in 1.5 g of TOP was quickly injected. The nanocrystals were allowed to grow for a given time, the reaction was quenched and toluene was added. The nanocrystals are purified in the same way as described in procedure 1.

Procedure 3. Sample S5 was synthesized according to a literature procedure[11]. A mixture of 0.1687 g of cadmium acetate, 5.7 g of TOPO, 0.5 g of TDPA and 0.12 g of HPA was degassed under a nitrogen flow at 120 ℃ for 1 hour. Next, the mixture was heated to 340 ℃ under a nitrogen atmosphere and a mixture of 0.09 g of Se dissolved in 3.6 g of TOP was quickly injected. The reaction was quenched after 6 minutes and was purified as described in procedure 1 except for the isopropanol is replaced by methanol as the non-solvent.

Procedure 4. CdS QRs were synthesized according to a literature procedure[10]. In sample S6, first CdS core QDs with diameter of 3.5 nm was synthesized. For this, a mixture of 0.10 g CdO, 3.29 g of TOPO and 0.60 g of ODPA was degassed under vacuum at 120 ℃ for one hour. Next, the mixture was heated to 320 ℃ under nitrogen atmosphere and a mixture of 0.17 g of bis(trimethylsilyl) sulfide [$(TMS_2)S$] and 3 g of tri-n-butylphosphine (TBP) was quickly injected. The reaction was quenched after 2 minutes and was purified as described in procedure 3. The rods were prepared from a mixture of 0.09 g of CdO, 3 g of TOPO, 0.3 g of ODPA and 0.08 g of HPA which was degassed under vacuum at 150 ℃ for one hour. Next, the mixture was heated to 350 ℃ under nitrogen

atmosphere and 1.8 mL of TOP was injected. Subsequently at the same temperature 0.12 g of S in 1.8 mL of TOP and 100 μL of the cores was injected to the reaction mixture. The reaction was quenched after 8 minutes and was purified as described in procedure 3.

Sample name	Procedure	Reaction time (min)	Length (nm)	Breadth (nm)	Aspect ratio
S1	1	2	25.1±3.2	5.3±0.6	4.8±0.8
S2	2	6	19.0±1.8	8.6±1.0	2.2±0.3
S3	1	5	34.2±5.7	6.7±0.6	5.1±1.0
S4	2	3	24.6±2.2	6.9±0.7	3.6±0.5
S5	3	6	33.6±3.7	8.9±1.1	3.8±0.6
S6	4	8	13.4±1.4	4.2±0.9	3.2±0.5

Table 4.1: Characteristics of wz-CdSe QRs (S1-S5) and wz-CdS QR (S6) used in this work.

4.3 Materials characterisation

4.3.1 Structural Characterisation

The crystal structure of the synthesized QRs us examined by powder X-ray diffraction (XRD). For the XRD measurement the sample is prepared by drying the QR suspension under a nitrogen flow and resuspending the dry powder in a mixture of 2 parts of hexane and 4 parts of heptane. Subsequent drop casting of the QR suspension on a 1 cm^2 glass plate completes the sample preperation. The XRD measurement on sample S5 and sample S6 shows that the CdSe QRs and CdS QRs have the expected wurtzite crystal structure (shown in Fig.4.1). The combination of broad and narrow reflections is a typical feature of rod-like nanocrystalline material. The synthesized QRs have been further examined with TEM. The TEM micrographs confirm the formation of QRs and enable us to determine their dimensions (length and breadth). Figure 4.2 shows overview images of the different batches of CdSe QRs synthesized.

4.3.2 Elemenetal composition

The QR absorption coefficients can be determined with the knowledge of QR volume fraction in the measured dispersion. To deter-

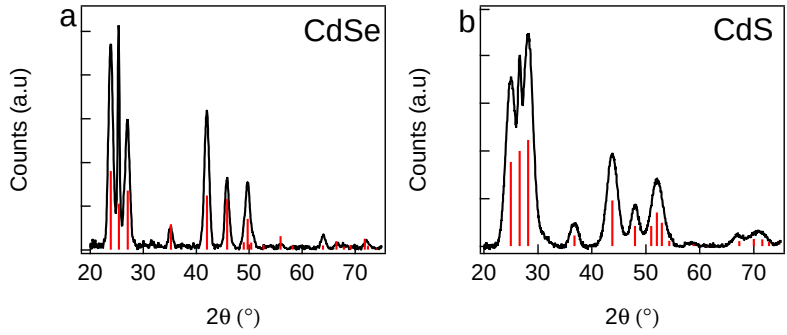

Figure 4.1: XRD spectrum of **(a)** CdSe QRs (sample S5) and **(b)** CdS QRs (sample S6).

mine the volume fractions, the elemental composition of the CdSe QR batches S1 to S4 has been measured using inductively coupled plasma optical spectrometry (ICP-OES). This measurement and analysis was done at department of analytical chemisrty, Ghent university by Sien Compernolle and Frank Vanhaecke. QR samples for ICP-OES have been prepared by drying 100 μL of CdSe QR suspension in a nitrogen flow. The dried samples are digested in 500 μL of HNO_3 to be analyzed using a spectro Acros ICP-OES. An identical amount of respective QR dispersions as used for ICP-OES measurements were dried under a nitrogen flow and resuspended in a known amount of heptane for UV-vis analysis.

4.4 Theoretical framework

In chapters II and III we came across the absorbance A of a QD dispersion which can be quantified by the intrinsic absorption coefficient μ_i. Within the Maxwell Garnett model, the absorption coefficient can be written in terms of the refractive index n_s of the solvent and the dielectric function $\varepsilon = \varepsilon_R + i\varepsilon_I$ of the dispersed particles[18]:

$$\mu_{i,th} = \frac{2\pi\varepsilon_I}{n_s\lambda}|f_{LF}|^2 \tag{4.1}$$

For various materials, such as InAs,[12] wz- and zb-CdSe,[13,14] PbS,[15] PbSe,[16] ZnO,[17] and zb-CdTe (Chapter III), it has been shown that μ_i is independent of the QD size at energies well above the bandgap energy. Moreover, using the dielectric function for

Figure 4.2: Absorption spectra and TEM images of samples S1-S6.

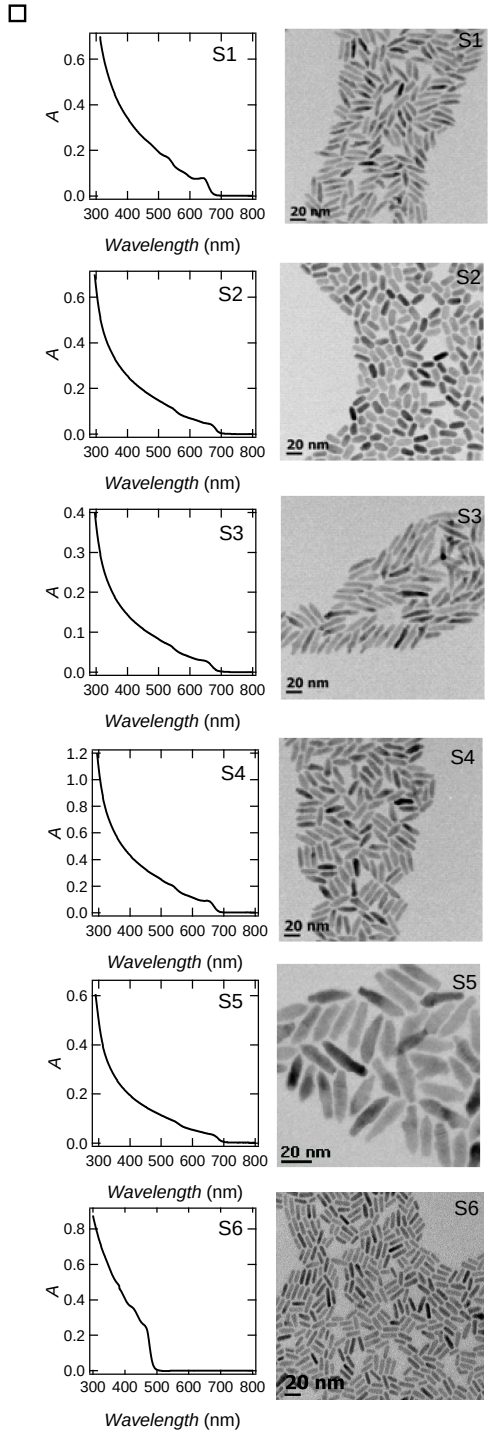

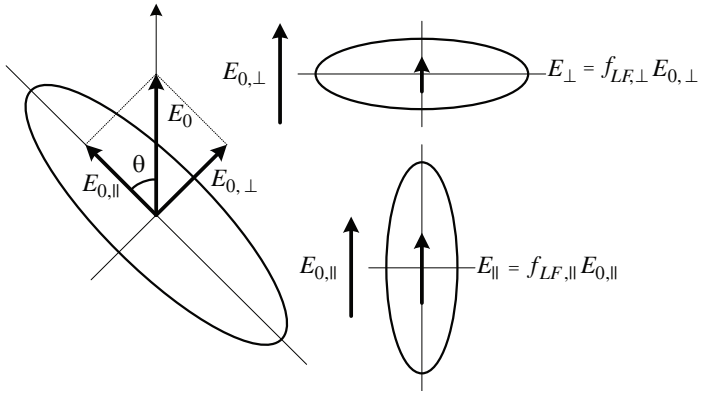

Figure 4.3: A spheroid will screen the components of the external electric field E_0 parallel ($E_{0,\parallel}$) and perpendicular ($E_{0,\perp}$) to its long axis in a different way. This leads to different internal fields $E_\parallel = f_{LF,\parallel} E_{0,\parallel}$ and $E_\perp = f_{LF,\perp} E_{0,\perp}$ and therefore different absorption coefficients (in the case of $\varepsilon > \varepsilon_s$).

the corresponding bulk material in eq. 4.1 generally leads to a good agreement between experimental and theoretical absorption coefficients for dispersed QDs at these high photon energies.

In eq. 4.1, the local field factor f_{LF} gives the ratio between the (optical) electric field outside (E_0) and inside (E) a QD. With α the depolarization factor of the QD and ε_s the square of n_s, f_{LF} reads:

$$f_{LF} = \frac{\varepsilon_s}{(1-\alpha)\varepsilon_s + \alpha\varepsilon} \tag{4.2}$$

Equation 4.1 shows that $\mu_{i,th}$ strongly depends on $|f_{LF}|$, *i.e.*, on the screening of the external field by the QD. With spherical objects, the depolarization factor is isotropic, amounting to 1/3 regardless of the direction of the electric field with respect to the particle. With anisotropic shapes, this is no longer true. Prolate spheroids for instance have different depolarization factors for fields parallel ($\alpha_\parallel$) and perpendicular ($\alpha_\perp$) to their long axis. As shown in Fig. 4.3, this results in a different screening of parallel and perpendicular fields and thus different local field factors $f_{LF,\parallel}$ and $f_{LF,\perp}$. Therefore, the absorption coefficient will depend on the angle θ between the external (optical) electric field and the long axis of the spheroid (see Fig. 4.3):

$$\mu_{i,th} = \frac{2\pi\varepsilon_I}{n_s\lambda}|f_{LF,\parallel}|^2\cos^2\theta + \frac{2\pi\varepsilon_I}{n_s\lambda}|f_{LF,\perp}|^2\sin^2\theta \tag{4.3}$$

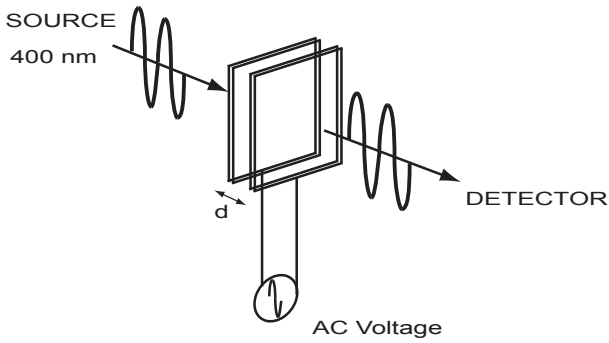

Figure 4.4: Representation of the experimental setup constituting of an optical cell composed of two ITO coated glass plates separated by d= 16 μm spacers. The cell can be subjected to an AC voltage and is housed in a UV-vis spectrophotometer.

Here, the absorption coefficients for light polarized parallel and perpendicular to the long axis of the rod are defined as:

$$\mu_{i,\parallel} = \frac{2\pi\varepsilon_I}{n_s\lambda}|f_{LF,\parallel}|^2 \tag{4.4}$$

$$\mu_{i,\perp} = \frac{2\pi\varepsilon_I}{n_s\lambda}|f_{LF,\perp}|^2 \tag{4.5}$$

According to eq. 4.2, f_{LF} increases when α goes down if $\varepsilon > \varepsilon_s$, a typical situation for semiconductor nanocrystals in an apolar solvent, Hence, for a prolate spheroid, $f_{LF,\parallel}$ will be larger than $f_{LF,\perp}$,[19] implying an increase of the absorbance for optical electric fields parallel to the long axis and a reduction for perpendicular fields.

4.5 Electro-optical measurements of quantum rods

4.5.1 Setup

To determine the absorption coefficient anisotropy of colloidal quantum rods, we use a setup where a QR dispersion is sandwiched between two parallel, transparent electrodes. In this way,

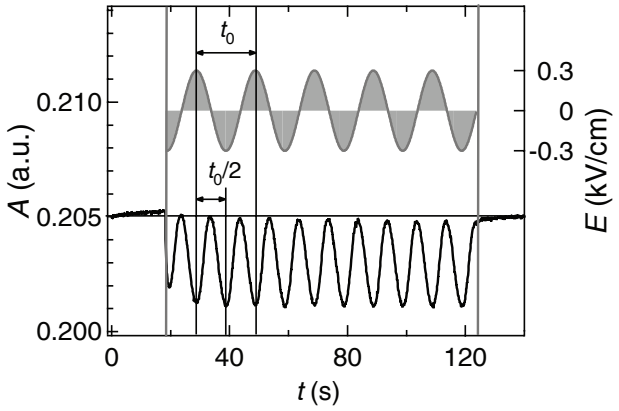

Figure 4.5: (top trace) Representation of the 50 mHz oscillating electric field applied over a dispersion of QRs. The time t_0 corresponds to 20 s. (bottom trace) Resulting change in absorbance measured with 3.8 aspect ratio CdSe QRs.

the absorbance of the dispersion can be measured as a function of an electric field – used to align the QRs – applied across this cell (see Fig. 4.4). In practice, the cell is constructed by two glass plates coated with indium tin oxide (ITO) on one side and held together with a glue containing 16 μ m spacers. For each cell, the actual distance d between the electrodes is determined by interferometry. The optical cell is placed in a UV-vis spectrophotometer (Perkin-Elmer lambda 35) and the absorbance is measured at a wavelength of 400 nm and at first exciton peak. As the sampling rate of the spectrophotometer is 0.1 s, we either use low frequency alternating fields and measure the actual absorbance as a function of time or high frequency fields (0.5–10 kHz), leading to a measured absorbance which is a time average over many periods of oscillation. The QR samples are suspended in dodecane for the measurements, as its boiling point is higher compared to toluene or heptane.

4.5.2 Low frequency AC field measurements

Figure 4.5 shows the change in absorbance of sample S5 when an AC field with a frequency f of 50 mHz and an amplitude E of 0.3 kV/cm is applied over a dispersion of CdSe QRs in dodecane. Two important observations follow from this experiment.

First, with the electric field applied, the absorbance is always lower than the absorbance without electric field. Second, the absorbance changes at a frequency of $2 \times f$. Both observations are in line with the idea that (a) the electric field aligns the QRs with their long axis parallel to the field and (b) the measured change in absorbance reflects the orientation dependence of the QR absorption coefficient. Indeed, with the electric field applied along the propagation direction of the light, QRs align themselves with their long axis perpendicular to the optical electric field. As $f_{LF,\parallel} > f_{LF,\perp}$ for a prolate spheroid in a low dielectric constant environment, this leads to a reduction of the absorbance. In addition, the QR absorbance only depends on the angle θ between its long axis and the optical electric field. Therefore, the change in absorbance may depend on the magnitude of the electric field, but not on its sign. As a result, the absorbance oscillates at the double frequency of the electric field.

4.5.3 Frequency dependence

To corroborate the link between the absorbance changes and the alignment of the QRs, we further studied A as a function of E. For this purpose, low frequency fields are not ideal. As shown in the literature, even in dodecane, a fraction of the QRs carries an electric charge, implying that an applied electric field induces drift of the QRs towards the electrodes.[20] To prevent accumulation of the QRs at the electrodes, the period of oscillation should be shorter than the cell transit time $\tau_{tr} = d/\mu E$, *i.e.*, the time it takes for a single rod with mobility μ to cross the cell. For the S5 rods in a 16 μm cell, the cell transit time is about 10 ms for fields of 50 kV/cm. Therefore, we switch to higher frequency fields to measure the average $\langle A \rangle$ of the absorbance.

Figure 4.6 shows $\langle |\Delta A|/A(0) \rangle$ measured on sample S4 as a function of f, keeping E constant at 96.8 kV/cm. One sees that with increasing frequency, the response strongly drops once the frequency exceeds 20 kHz. This drop can be understood by considering the rotational relaxation time τ_{rot} of the rods about their short axis. Within the Debye-Perrin[21] model, τ_{rot} is expressed as :

$$\tau_{rot} = \frac{C}{2k_B T} \tag{4.6}$$

Here, k_B is the Boltzmann constant, T is the absolute temperature

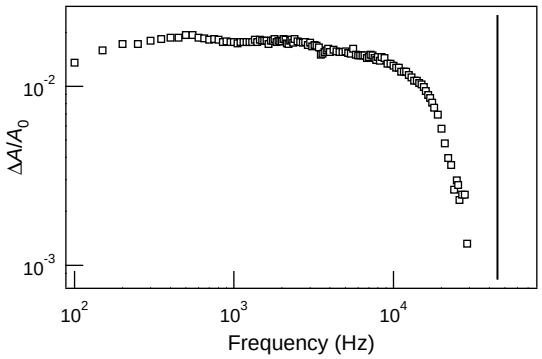

Figure 4.6: Relative shift in absorbance measured as a function of the frequency f of the aligning field using a constant amplitude E of 96.8 kV/cm. The vertical line is drawn at 45 kHz, corresponding to $1/2\pi\tau_{rot}$ for the sample analysed here (S4).

and C is the rotational friction coefficient, which reads for a prolate spheroid:

$$C = \frac{32\pi\eta}{3}\frac{a^4 - b^4}{(2a^2 - b^2)S - 2a} \tag{4.7}$$

In this expression, η represents the viscosity of the solvent, while a and b stand for the the length of minor and major half axis of the spheroid. The quantity S is linked to a and b according to:

$$S = \frac{2}{(\sqrt{a^2 - b^2})} ln \frac{a + \sqrt{a^2 - b^2}}{b} \tag{4.8}$$

Taking a ligand shell thickness of 2 nm, the relaxation time τ_{rot} calculated for the QRs used here amounts to 3.6 μs (sample S4) and 7.3 μs (sample S5), respectively. This results in a critical frequency $1/2\pi\tau_{rot}$ of 45 kHz and 22 kHz respectively. The value of 45 kHz for sample S4 corresponds reasonably well with the observed drop in $\langle|\Delta A|/A(0)\rangle$ at frequencies above 20 kHz. Hence, to ensure that the alignment of the QRs follows the applied AC field, the applied frequency should be smaller than $1/\tau_{rot}$. This means that the quantitative analysis of absorption changes is limited to AC frequencies between of $1/\tau_{tr}$ and $1/\tau_{rot}$.

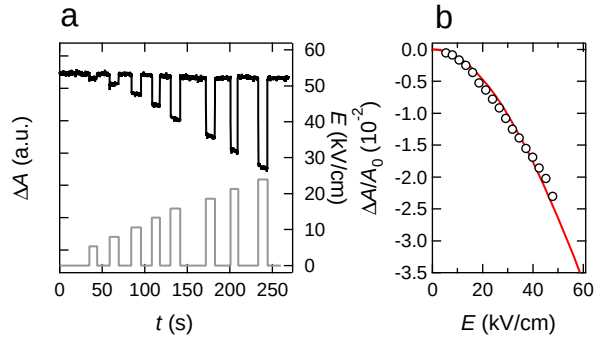

Figure 4.7: **(a)** (bottom trace) Amplitude of a 800 Hz E-field applied over a QR dispersion at 400 nm(S5). (top trace) Resulting change of the absorbance. **(b)** (markers) Resulting relative change of the absorbance as a function of field strength and (full line) predicted change of $\langle|\Delta A|/A(0)\rangle$ according to eq. 4.11 using a dipole moment of 333 D.

4.5.4 High frequency AC field measurements

Figure 4.7a shows a time trace of $\langle A\rangle$ when an 800 Hz electric field with amplitudes as indicated is switched on and off as a function of time measured at 400 nm . In line with the previous measurements (Fig. 4.5), we find that the absorbance drops upon application of an electric field, with a higher electric field yielding a larger change of the absorbance. In Fig. 4.7b, the effect of an electric field on the QR absorbance is plotted more quantitatively as $\langle|\Delta A|/A(0)\rangle$ *vs.* E. An element worth noticing here is that, while the overall trend is an increase of $\langle|\Delta A|/A(0)\rangle$ with E, we find that at low field strengths, the slope $d\langle|\Delta A|/A(0)\rangle/dE$ tends to zero.

4.5.5 Quantitative analysis of the high frequency results

For AC fields with $f \gg 1/\tau_{tr}$, accumulation of the rods at the electrodes can be neglected. Hence, as long as f is sufficiently smaller than $1/2\pi\tau_{rot}$, we can presume that the rods align according to Boltzmann statistics. An analytic expression for the absorption coefficient of an ensemble of QRs as a function of E can be dereived based on Boltzmann statistics. This is obtained by integrating the expression for the intrinsic absorption coefficient (eq. 4.3) over all possible orientations of the long axis of the

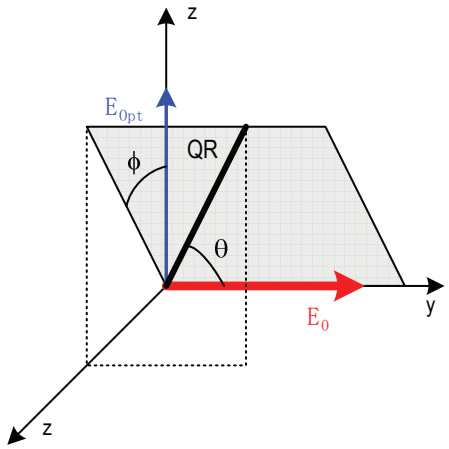

Figure 4.8: Orientation of a QR (black) relative to the applied electric field E_0 (red, y-axis) and the optical electric field (blue, z-axis) and definition of the angles θ and ϕ.

QR and the optical field. Importantly, an orienting electric field is applied perpendicular to the plane of polarization of the optical field. Therefore, QR orientations are weighed by a Boltzmann factor that contains the exponent $pE\cos(\theta)/k_BT$. Here, p is the dipole moment of the QR, E the orienting electric field, θ the angle between the long axis of the QR and the orienting electric field, k_B is Boltzmann's constant and T the absolute temperature.

Defining the orientation of the rod relative to the optical field and the aligning field using the angles ϕ and θ as shown in Fig. 4.8, the components of the optical field parallel and perpendicular to the long axis of the QR are given by:

$$E_{\parallel} = \cos\phi \sin\theta E_0$$

$$E_{\perp} = \sqrt{1 - \cos^2\phi \sin^2\theta} E_0$$

Since the absorbance is proportional to the electric field squared, the intrinsic absorption coefficient $\mu_i(\theta, \phi)$ of the rod for a given orientation can be written as:

$$\mu_i(\theta, \phi) = \mu_{i,\parallel} \cos^2\phi \sin^2\theta + \left(1 - \cos^2\phi \sin^2\theta\right) \mu_{i,\perp} \qquad (4.9)$$

In the case of an orienting electric field applied as shown in Fig. 4.8, each orientation will be weighted with a corresponding

Boltzmann factor. This yields:

$$\mu_i = \frac{\int_0^{2\pi}\int_0^{\pi}\left[\mu_{i,\parallel}\cos^2\phi\sin^2\theta + \left(1-\cos^2\phi\sin^2\theta\right)\mu_{i,\perp}\right] e^{\frac{pE\cos\theta}{k_BT}}\sin\theta d\theta d\phi}{\int_0^{2\pi}\int_0^{\pi} e^{\frac{pE\cos\theta}{k_BT}}\sin\theta d\theta d\phi} \tag{4.10}$$

In the above expression, the integrals over ϕ and θ can be readily solved, yielding ($\mathcal{E} = pE/k_BT$)):

$$\mu_i = \mu_{i,\perp} + \left(\mu_{i,\parallel} - \mu_{i,\perp}\right)\left[\frac{\cosh(\mathcal{E})}{\mathcal{E}\sinh(\mathcal{E})} - \frac{1}{\mathcal{E}^2}\right] \tag{4.11}$$

Based on eq. 4.11, we can calculate $\langle|\Delta A|/A(0)\rangle$ provided $\mu_{i,\perp}$, $\mu_{i,\parallel}$ and p are known. Using the bulk dielectric function of wz-CdSe, this leaves us with the QR dipole moment as the only adjustable parameter. The full line in Fig. 4.7b represents the predicted values for $\langle|\Delta A|/A(0)\rangle$, using a dipole moment of 1.1×10^{-27} C m, *i.e.*, 330 D. This value is fully in line with published literature data[22], which confirms that CdSe QRs have anisotropic absorption coefficients that can be understood simply from the anisotropy of the local field factors.

4.5.6 Assessment of the method

The excellent agreement between experiment and theory obtained with a realistic value of the QR dipole moment demonstrates that the approach presented here enables a direct measurement of absorption anisotropy of colloidal QRs. The quantitative analysis of $\langle|\Delta A|/A(0)\rangle$ as a function of E depends on two parameters, *i.e.*, the dipole moment p and the ratio $\gamma = \mu_{i,\perp}/\mu_{i,\parallel}$ between the perpendicular and the parallel absorption coefficients. At high field strengths, $\langle|\Delta A|/A(0)\rangle$ reaches a limiting value that only depends on γ:

$$\lim_{E\to\infty}\langle\frac{|\Delta A|}{A(0)}\rangle = \frac{1-\gamma}{1+2\gamma} \tag{4.12}$$

This means that, in principle, both p and γ can be reliably determined by the experimental method proposed here. For CdSe QRs with an aspect ratio of 3.8, the limiting value of γ amounts to about 0.5. However, for the highest field strengths used here, for which pE is about equal to thermal energy, a relative change in absorbance of only 2-3% is predicted and measured. This means that the experiment in Fig. 4.7b only shows the beginning of the

absorbance change, and in this case p and γ cannot be reliably determined together from a single trace. Increasing the field strength is difficult. It raises τ_{tr}, which leads to irreversible changes of the absorbance with time. This limits the quantitative analysis to a situation where either p or γ are known. Interestingly, with the 50 mHz field used in Fig. 4.5, an absorbance drop by 2-3 % is achieved with considerably lower field strengths. Since in this case, $f \ll 1/\tau_{tr}$, this may reflect the much stronger alignment of the CdSe QRs at the electrodes.[10]

4.5.7 Absorption anisotropy at the bandgap transition in CdSe and CdS quantum rods

To determine absorption anisotropy at the first exciton absorbance using the method developed here, the dipole moment of the QRs must be known. Therefore, we first measure $\langle|\Delta A|/A(0)\rangle$ at short wavelengths, where $\gamma = \mu_{i,\perp}/\mu_{i,\parallel}$ can be calculated using bulk optical constants. Figures 4.9a and c show $\langle|\Delta A|/A(0)\rangle$ at 400 nm as a function of field strength for CdS and CdSe rods with aspect ratios of 3.2 (sample S6) and 5.1 (sample S3), respectively. Using γ values calculated using the bulk optical constants of wurtzite CdS and CdSe an excellent correspondence of the experimental data and eq. 4.11 is found for dipole moments of 87 D and 180 D, respectively (see table 4.3 for calculated absorption coefficients).

At the bandgap transition, a similar decrease of $\langle|\Delta A|/A(0)\rangle$ with increasing field strength is observed for both samples and its magnitude is similar to measurements at short wavelengths (Fig. 4.9b). Since the dipole moment is the same at short and at long wavelengths, an excellent quantitative agreement between the measurements and eq. 4.11 is obtained. By keeping the dipole moment fixed and taking the value for γ calculated using bulk optical constants to be $\gamma = 0.27$ and $\gamma = 0.30$ for CdS and CdSe QRs respectively. This shows the shift in absorbance measured at short wavelengths and at the band gap is mainly due to the local field anisotropy.

Sample	λ	n_s	$n_\parallel$	$k_\parallel$	$n_\perp$	$k_\perp$	$\mu_{i,\parallel}$	$\mu_{i,\perp}$
	(nm)						(10^7 m^{-1})	(10^6 m^{-1})
CdSe(S3)	400	1.52	2.77	0.57	2.75	0.53	1.59	4.22
CdSe(S3)	652	1.49	2.79	0.25	2.76	0.28	0.72	2.19
CdS(S6)	400	1.52	2.61	0.46	2.55	0.44	1.76	5.04
CdS(S6)	458	1.51	2.66	0.40	2.58	0.38	1.34	3.61

Table 4.2: Absorption coefficients $\mu_{i,\parallel}$ and $\mu_{i,\perp}$ calculated in dodecane using the bulk dielectric function of wz-CdSe and wz-CdS.

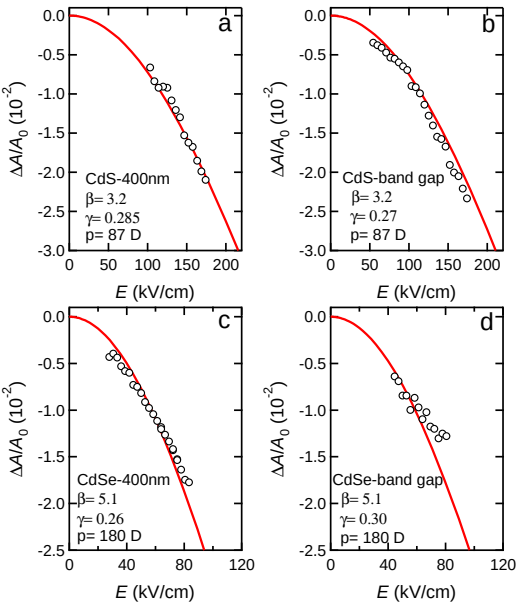

Figure 4.9: **(a)** (markers) Resulting relative change of the absorbance as a function of field strength and (red line) calculated change of $\langle|\Delta A|/A(0)\rangle$ according to eq. 4.11 for $p = 87$ D and $\gamma = 0.285$ at 400nm for an aspect ratio β of 3.2 CdS QRs.**(b)** (markers) Relative change of absorbance at the band edge, (red line) calculated change using the same vlaues for p and $\gamma = 0.27$ as in (a).**(c),(d)** The same as(a),(b) for CdSe QRs with β= 5.1.

4.6 Determination of absorption coefficient of CdSe quantum rods

When no electric fields are applied across a QR dispersion, one can assume that they are randomly distributed. In that case, averaging the absorption coefficient over all possible orientations simply yields:

$$\mu_i = \frac{1}{4\pi}\int_0^{2\pi}\int_0^{\pi}\left[\mu_{i,\parallel}\cos^2\phi\sin^2\theta + \left(1-\cos^2\phi\sin^2\theta\right)\mu_{i,\perp}\right]\sin\theta d\theta d\phi \tag{4.13}$$

This results in an expression for the intrinsic absorption coefficient $\mu_{i,0}$ of randomly aligned QRs as a weighted average over $\mu_{i,\perp}$ and $\mu_{i,\parallel}$:

$$\mu_{i,0} = \frac{2}{3}\mu_{i,\perp} + \frac{1}{3}\mu_{i,\parallel} \tag{4.14}$$

Hence, opposite to colloidal QDs, the intrinsic absorption coefficient of QRs is not a constant, yet depends on the aspect ratio of the rods. This also implies that QRs do not have the same intrinsic absorption coefficient as QDs, which can be considered as QRs with an aspect ratio of one. To verify this, we synthesized CdSe QR samples with 4 different aspect ratios and combined TEM imaging with elemental analysis by inductively coupled mass spectrometry. In this way, we could calculate the volume fraction of QRs in solution, and therefore obtain $\mu_{i,0}$ from the absorbance measured (see table 4.3). In Fig. 4.10a, the line with the markers shows $\mu_{i,0}$ thus determined for 3.6 aspect ratio QRs dispersed in heptane, next to theoretical curves calculated using the bulk dielectric function of wz-CdSe for (grey background) QDs and (full

Sample name	Cd (mg/l)	Se (mg/l)	A_{300}	dilution	$\mu_{i,300}$ (10^7 m^{-1})
S1	1488.15	963.28	0.856	30	2.75
S2	411.70	272.80	0.639	10	2.44
S3	612.25	397.45	0.368	30	2.87
S4	1888.08	1235.88	1.083	30	2.72

Table 4.3: Overview of the ICP-OES results of QR samples S1 to S4 in combination with the absorbance at 300 nm (A_{300}), the dilution of the respective UV-vis sample relative to the ICP-OES sample and the resulting intrinsic absorption coefficient $\mu_{i,300}$ at 300 nm.

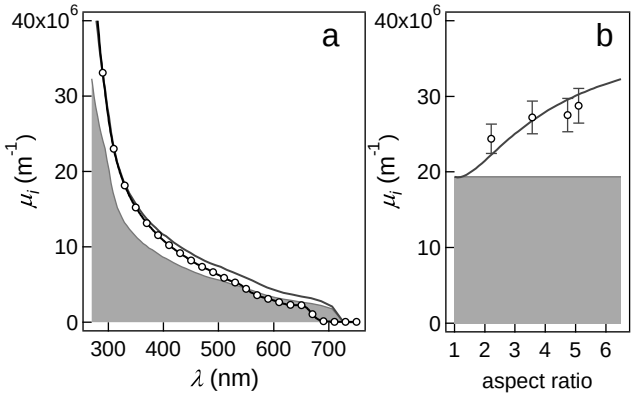

Figure 4.10: **(a)** (line with markers) Spectrum of the intrinsic absorption $\mu_{i,0}$ for 3.6 aspect ratio wz-CdSe QRs in heptane (sample S4). (full line) theoretical $\mu_{i,0}$ of 3.6 aspect ratio wz-CdSe QRs in heptane and (grey background) theoretical $\mu_{i,0}$ of wz-QDs in heptane. **(b)** (markers) Experimentally deterimend $\mu_{i,0}$ at 300 nm for CdSe QR in heptane (samples S1-S4). (full line) theoretical $\mu_{i,0}$ of wz-CdSe QRs in heptane at 300 nm and (grey background) idem for wz-CdSe QDs.

line) 3.6 aspect ratio QRs. We see that at wavelengths below 500 nm, the experimental $\mu_{i,0}$ exceeds the theoretical curve of wz-CdSe QDs and coincides with the theoretical $\mu_{i,0}$ for 3.6 aspect ratio QRs at wavelengths of about 300 nm. Figure 4.10b shows a comparison between the theoretical and experimental $\mu_{i,0}$ values at 300 nm of QRs with different aspect ratio. Despite the scatter on the experimental values, the data show that the experimental $\mu_{i,0}$ of the QRs exceed the value of QDs by 21 to 43% for aspect ratios increasing from 2.3 to 5.4. Moreover, the experimental values largely coincide with the $\mu_{i,0}$ calculated for QRs using eq. 4.14. In contrast with existing literature, we therefore conclude that the intrinsic absorption coefficient of colloidal QRs is not a constant equal to that of colloidal QDs of the same material.[8] Due to the anisotropy of the local field factors, it markedly increases with increasing aspect ratio, making QRs in general stronger absorbers than QDs. A similar conclusion followed from the analysis of the absorption coefficient of CdSe nanowires.[4]

4.7 Conclusions

We introduce and assess an experimental method to analyze absorption anisotropy of dispersed rod-like colloidal nanocrystals, in which the absorbance of the dispersion is measured while aligning the nanocrystals using an electric field. Using alternating electric fields high enough to prevent charge accumulation at the electrodes and low enough to ensure rotational relaxation, we demonstrate that the resulting change in absorbance as a function of field strength can be quantified by a model based on Boltzmann statistics. The method is validated using CdSe and CdS quantum rods, where we find a difference between the absorption coefficient at 400 nm and at bandgap for fields polarized parallel and perpendicular to the rod axis that is fully in line with the predictions of the local field approximation. The absorption anisotropy implies that randomly dispersed CdSe quantum rods have a larger absorption coefficient than CdSe quantum dots.

Bibliography

[1] D. V. Talapin et al., *Prospects of colloidal nanocrystals for electronic and optoelectronic applications*, Chem. Rev. **2010**, *110*, 389–458.

[2] J. Wang et al., *Highly polarized photoluminescence and photodetection from single Indium Phosphide nanowires*, Science **2001**, *293*, 1455–1457.

[3] V. Protasenko, D. Bacinello and M. Kuno, *Experimental determination of the absorption cross-section and molar extinction coefficient of CdSe and CdTe nanowires*, J. Phys. Chem. B **2006**, *110*, 25322–25331.

[4] J. Giblin and M. Kuno, *Nanostructure absorption: a comparative study of nanowire and colloidal quantum dot absorption cross sections*, J. Phys. Chem. Lett. **2010**, *1*, 3340–3348.

[5] R. Krahne et al., *Physical properties of elongated inorganic nanoparticles*, Phys. Rep. **2011**, *501*, 75–221.

[6] X. Chen et al., *Polarization spectroscopy of single CdSe quantum rods*, Phys. Rev. B **2001**, *64*, 245304.

[7] H. Htoon et al., *Light amplification in semiconductor nanocrystals: quantum rods versus quantum dots*, Appl. Phys. Lett. **2003**, *82*, 4776–4478.

[8] E. Shaviv, A. Salant and U. Banin, *Size dependence of molar absorption coefficients of CdSe semiconductor quantum rods*, Chem. Phys. Chem. **2009**, *10*, 1028–1031.

[9] I. Gur et al., *Air-stable all-inorganic nanocrystal solar cells processed from solution*, Science **2005**, *310*, 462–465.

[10] L. Carbone et al., *Synthesis and micrometer-scale assembly of colloidal CdSe/CdS nanorods prepared by a seeded growth approach*, Nano Lett. **2007**, *7*, 2942–2950.

[11] P. T. K. Chin et al., *Energytransfer and polarizedemission in Cadmium Selenide nanocrystal solids with mixed dimensionality*, Adv. Funct. Mater. **2007**, *17*, 3829–3835.

[12] P. R. Yu et al., *Absorption cross-section and related optical properties of colloidal InAs quantum dots*, J. Phys. Chem. B **2005**, *109*, 7084–7087.

[13] C. Leatherdale et al., *On the absorption cross section of CdSe nanocrystal quantum dots*, J. Phys. Chem. B **2002**, *106*, 7619–7622.

[14] R. K. Capek et al., *Optical properties of zincblende cadmium selenide quantum dots*, J. Phys. Chem. C **2010**, *114-119*, 6371.

[15] I. Moreels et al., *Size-dependent optical properties of colloidal PbS quantum dots*, ACS Nano **2009**, *3*, 3023–3030.

[16] I. Moreels et al., *Composition and size-dependent extinction coefficient of colloidal PbSe quantum dots*, Chem. Mater. **2007**, *19*, 6101–6106.

[17] P. Lommens et al., *The growth of Co : ZnO/ZnO core/shell colloidal quantum dots: Changes in nanocrystal size, concentration and dopant coordination*, Chem. Phys. Chem. **2008**, *9*, 484–491.

[18] D. Ricard, M. Ghanassi and M. C. Schanneklein, *Dielectric confinement and the linear and nonlinear-otical properties of semicondutor-doped glasses*, Opt. Commun. **1994**, *108*, 311–318.

[19] J. Osborn, *Demagnetizing factors of the general ellipsoid*, Phys. Rev. **1945**, *67*, 351–358.

[20] M. Cirillo et al., *Thermal charging of colloidal quantum dots in apolar solvents: a current transient analysis*, ACS Nano **2011**, *5*, 1345–1352.

[21] P. F. Perrin, *Mouvement brownien d'un ellipsoide (I). Dispersion dielectrique pour des molecules ellipsoidales*, J. Phys. Radium **1934**, *10*, 497– 511.

[22] L. Li and A. Alivisatos, *Origin and scaling of the permanent dipole moment in CdSe nanorods*, Phys. Rev. Lett. **2003**, *90*.

Chapter V

Anisotropy in CdSe/CdS dot-in-rod

5.1 Introduction

Combining different materials at the nanoscale to form heterostructures creates opportunity to manipulate the wave function and other material properties[1,2]. These nanostructures can be prepared by multistep synthesis where pre-synthesised nanocrystals are used as seeds for nucleation and growth of the inorganic phase. Significant progress has been acheived in this respect by the pioneering work of Talapin *et.al.* with the synthesis of core-shell nanocrystals by combining two different semiconductors in the form of concentric core and rod shaped shell[3]. The process of making mixed dimensional heterostructures was further popularised by Manna *et.al.* by demonstrating greater synthetic control[4]. One example of such a heterostructured system is CdSe/CdS dot-in-rods. It consists of a CdSe QD core which is zero dimensional system encapsulated in a rod shaped CdS shell which is a one dimensional system. Much attention has been given to this class of material as their band alignment can be tuned from type I to quasi type II by tunning the size of the QD core size. The quantum yield observed in these systems can be upto 75 % which makes them attaractive[3] for applications such as LED[5], bio-imaging[6] *etc.* Literature reveals that these systems exhibit highly polarised emmision emanating from the first exciton transition, which is an interesting attribute to this system. This gives rise to the question whether these systems also exhibit polarised

absorption at the first exciton transition which has not been demonstrated so far. In this regard, electro-optical measurements can give insight on this aspect which forms the fundamental basis for this investigation. In this chapter the focus is to determine the absorption anisotropy in CdSe/CdS QR system by extending the experimental formalism used to determine absorption anisotropy in CdSe QRs as described in chapter IV. The key advantage of this system is that we can probe at the first exciton transition, which has a clear absorption feature unlike that of CdSe QRs. The reliability and consistency of the electro-optical measurement technique is examined. In addition, the excellent synthetic control and extensive characterization by TEM paved the way to probe the wave function delocalization of CdSe/CdS dot-in-rods by time and temperature resolved spectroscopy. This work is done in collaboration with Gabriele Raino (IBM research) and a summary of this work constitutes a considerable part of this chapter.

5.2 Synthesis

In this work seven batches of CdSe/CdS core shell nanorods (labelled S1-S7) are synthesized according to a reported literature procedure[4]. Taking the example of sample S1, first CdSe core QDs with diameter of 3.7 nm are synthesised. For this, a mixture of 0.12 g of CdO, 6 g of TOPO and 0.56 g of ODPA was degassed under vacuum at 120 °C for 1 hour. Next, the mixture was heated upto 350 °C under nitrogen atmosphere and a mixture of 0.116 g of Se and 0.72 g of TOP was quickly injected. The reaction was quenched after 30 seconds and purified three times by using toluene and isopropanol as the solvent and the non-solvent respectively, followed by centrifugation and decantation. The concentration of the synthesized CdSe cores is deduced by using the sizing curve and molar extinction coefficients reported by Jasieniak *et al.*[7].

The core/shell dot-in-rod is prepared from a mixture of 0.057 g of CdO, 3 g of TOPO, 0.29 g of ODPA and 0.08 g of HPA which is degassed under vacuum at 120 °C for 1 hour. Next, the mixture is heated to 350 °C under nitrogen atmosphere and 1.8 mL of TOP is injected. Subsequently at the same temperature 0.12 g of S in 1.8 mL of TOP and 300 μL of cores with concentration of 239 μM is injected in the reaction mixture. The reaction is

	S1	S2	S3	S4	S5	S6	S7
Core size (nm)	3.7	2.5	3.4	2.2	2.5	2.9	3.3
Core con (μM)	239	1148	744	270	14486	976	143
CdO (g)	0.057	0.057	0.057	0.18	0.06	0.086	0.06
TOPO (g)	3	3	3	6	3	3	3
ODPA (g)	0.29	0.29	0.29	0.57	0.29	0.29	0.29
HPA (g)	0.08	0.08	0.08	0.16	0.08	0.08	0.08
TOP (g)	1.5	1.5	1.5	3	1.5	1.5	1.5
S (g)	0.12	0.12	0.12	0.12	0.7	0.12	0.7
time (min)	8	6	8	6	8	8	8

Table 5.1: Synthetic procedure for CdSe/CdS QRs used in this work.

quenched after 8 minutes with toluene and purified with the same procedure as described earlier for the cores. The samples S2-S7 are synthesised according to the procedure mentioned above. The synthetic parameters are summarised in the table 5.1.

5.3 Structural Characterisation

We analyse the crystal structure and the morphology of the synthesised CdSe/CdS dot-in-rods using XRD and TEM techniques. The XRD diffractogram shown in Fig. 5.1a confirms the formation of CdSe/CdS QRs with wurtzite crystal structure. The dimensions and the morphology of thus formed QRs is investigated in detail with TEM. The table 5.2 summarises the dimensions of the rods used in this work. Figure 5.1b and c shows TEM and HR-TEM image of CdSe/CdS dot-in-rods (sample S7) respectively. The ensemble representative TEM images of all the samples are given in Fig. 5.2.

Sample name	Length (nm)	Breadth (nm)	β
S1	24.2 $\pm$3.9	5.6 $\pm$0.7	4.3
S2	12.1 $\pm$1.6	3.7 $\pm$0.6	3.2
S3	24.2 $\pm$2.0	4.9 $\pm$0.7	4.8
S4	37.6 $\pm$2.3	4.7 $\pm$0.5	8
S5	27.3 $\pm$3.3	4.8 $\pm$0.5	5.6
S6	29.9 $\pm$2.3	4.5 $\pm$0.5	6.6
S7	29.3 $\pm$2.4	4.1 $\pm$0.4	7.1

Table 5.2: Dimensions of CdSe/CdS QRs used in this work.

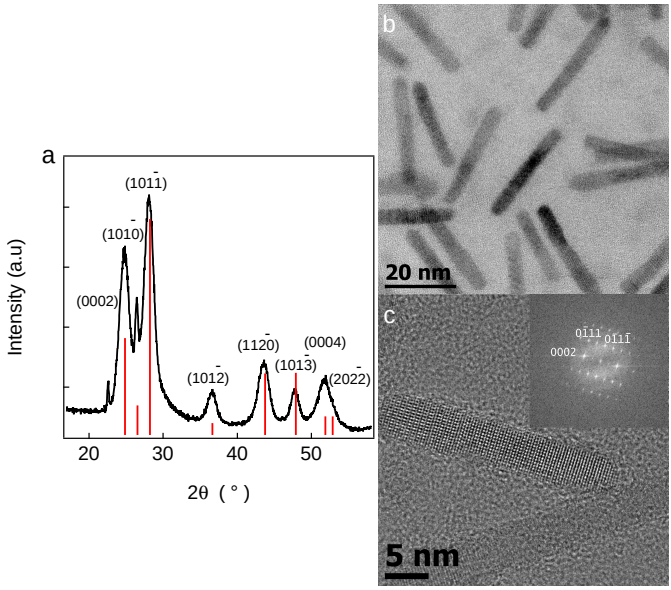

Figure 5.1: **(a)** Shows XRD diffractogram confirming wurtzite crystal structure. **(b)** TEM image of ensemble of CdSe/CdS dot-in-rods sample S7. **(c)** Corresponding HR-TEM image and the inset shows FFT of the image.

5.4 Optical Characterisation

UV-Vis absorption spectroscopy is the basic characterisation tool for the examination of the synthesized CdSe/CdS dot-in-rods. Figure 5.2 shows absorption spectrum of CdSe core and CdSe/CdS dot-in-rods corresponding to sample S4. The absorption spectrum of CdSe/CdS dot-in-rods is observed to be dominated by CdS absorption below 500 nm. The absorption spectrum corresponding to all the samples used in this work are shown in Fig. 5.4. Further optical characterization by luminescence spectroscopy and time resolved photoluminescence spectroscopy elucidating the carrier dynamics is highlighted towards the end of this chapter. The photoluminescence were measured with frequency doubled Ti:sapphire mode locked laser with pulses of about 150 fs duration at 400 nm and with a repetition rate of 80 MHz. The time-integrated photoluminescence was recorded by a CCD-coupled grating spectrometer. Time resolved photoluminescence was recorded by an avalanche photodiode with a time correlated single-photon counting module and the time resolution is 100 ps.

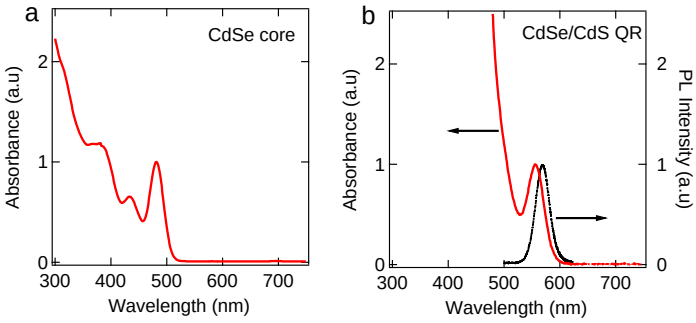

Figure 5.2: **(a)**UV-vis absorption spectrum of CdSe core. **(b)** Absorption and emmision spectrum of CdSe/CdS dot-in-rods (sample S4).

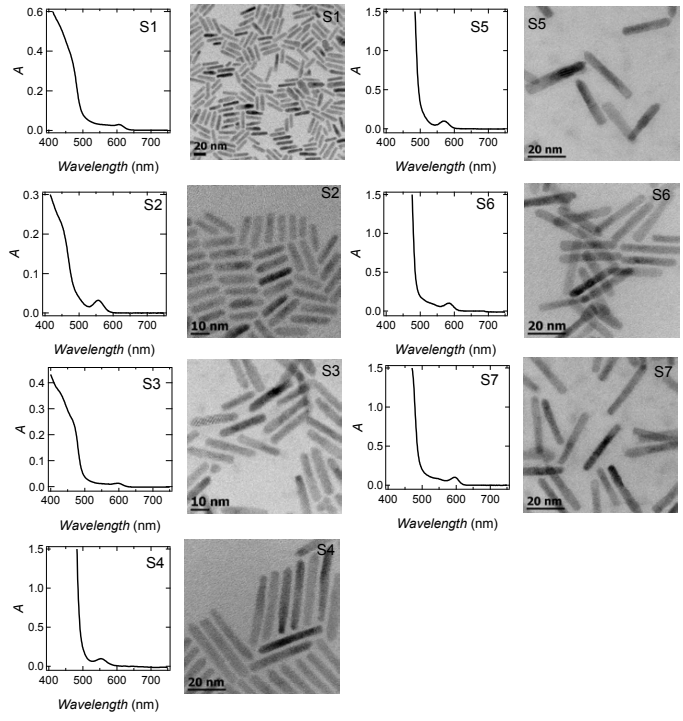

Figure 5.3: Absorption spectrum and TEM images of samples S1-S7.

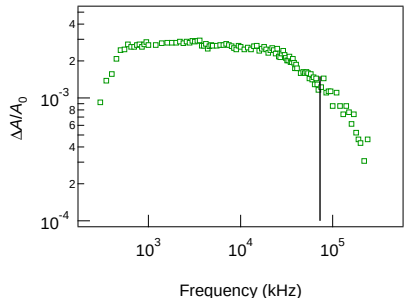

Figure 5.4: Relative change of the absorbance $\langle|\Delta A|/A(0)\rangle$ of sample S1 as a function of the frequency of the applied alternating field with an amplitude of 50 kV/cm. The vertical black line indicates $1/2\pi\tau_{rot}$.

5.5 Electro-Optical Measurements

The setup and the theoretical background of the measurement technique is described in section 4.5 of chapter III. In the measurements, the change in absorbance at 400 nm and at the band gap are measured as function of applied ac voltage pulse to determine the absorption anisotropy in the CdSe/CdS dot-in-rods.

5.5.1 Frequency Dependence

To obtain meaningful changes in absorbance upon rod alignment, the frequency of the aligning field must be between the rotational relaxtion time τ_{rot} and translation relaxtion time τ_{tr}. Figure 5.4 shows the change in absorbance of sample S1 as a function of frequency f, at a constant electric field with an amplitude of 50 kV/cm. With increasing frequency, the response drops drasticaly above 50 kHz. This effect is understood on the basis of the Debye-Perrin model (described in section 4.5 of chapter III). Based on the data given in table 5.2, we calculate a rotational correlation time for the rods analyzed here of 2 μs, which corresponds to a critical frequency of 73 kHz. This agrees well with the measured cut-off of the response.

5.5.2 AC field measurements at 400nm

To determine the absorption anisotropy at the first exciton transition from the change in absorbance as a function of field strength,

the dipole moment of these dot-in-rods must be known. Therefore, we first measure $\langle|\Delta A|/A(0)\rangle$ at short wavelengths, where $\gamma = \mu_{i,\perp}/\mu_{i,\parallel}$ can be calculated using bulk optical constants. Figures 5.5a, c and e show $\langle|\Delta A|/A(0)\rangle$ at 400 nm as a function of field strength for CdSe/CdS dot-in-rods with aspect ratios of 3.2 (sample S2), 4.3 (sample S1) and 4.8 (sample S3), respectively. In all cases, the measured variation is highly similar to that of the CdSe QRs as shown in Fig. 5.5b. Again, we analyse these curves using the eq 5.1, as described in chapter IV($\mathcal{E} = pE/(k_BT)$).

$$\mu_i = \mu_{i,\perp} + \left(\mu_{i,\parallel} - \mu_{i,\perp}\right)\left[\frac{\cosh(\mathcal{E})}{\mathcal{E}\sinh(\mathcal{E})} - \frac{1}{\mathcal{E}^2}\right] \tag{5.1}$$

Since the absorption of the dot-in-rods at 400 nm is dominated by the CdS, we use $\mu_{i,\perp}$ and $\mu_{i,\parallel}$ values calculated with the bulk optical constants of wurtzite CdS. In that case, a good agreement between experiments and theory is found for dipole moments of (S1) 117 D,(S2) 174 D and (S3) 252 D, respectively.

5.5.3 AC field measurements at the bandgap

At the first exciton transition, a similar decrease of $\langle|\Delta A|/A(0)\rangle$ with increasing field strength is observed for each of the samples, yet its magnitude is 1.5 to 2.5 times larger than at short wavelengths (Fig. 5.5b). Since the dipole moment is the same at short and at long wavelengths, this implies that the absorption anisotropy is considerably larger at the first exciton transition. In fact, for all samples, excellent quantitative agreement between the measurements and eq. 5.1 is obtained by keeping the dipole moment fixed and taking $\gamma = 0$, which indicates that $\mu_\perp \ll \mu_\parallel$ at the band gap transition.

For absorbers dispersed in a medium with refractive index n_s, the energy integrated absorption cross section $\sigma_{if,\mathrm{eV}}$ – which corresponds in the case of a QD or a QR to the product of the absorption coefficient and the QD or QR volume – of an electronic transition between an initial state $|i\rangle$ and a final state $|f\rangle$ is given by[8](e, charge on the electron; ω, angular frequency of the incident light; ϵ_0, permittivity of the vacuum; c, speed of light; $\mathbf{e}$, polarization vector of the incident light; $\mathbf{r}$, position vector):

$$\sigma_{if,\mathrm{eV}} = \frac{e\pi\omega}{\epsilon_0 n_s c}\left|\langle f|\mathbf{e}\cdot\mathbf{r}|i\rangle\right|^2 f_{LF}^2 \tag{5.2}$$

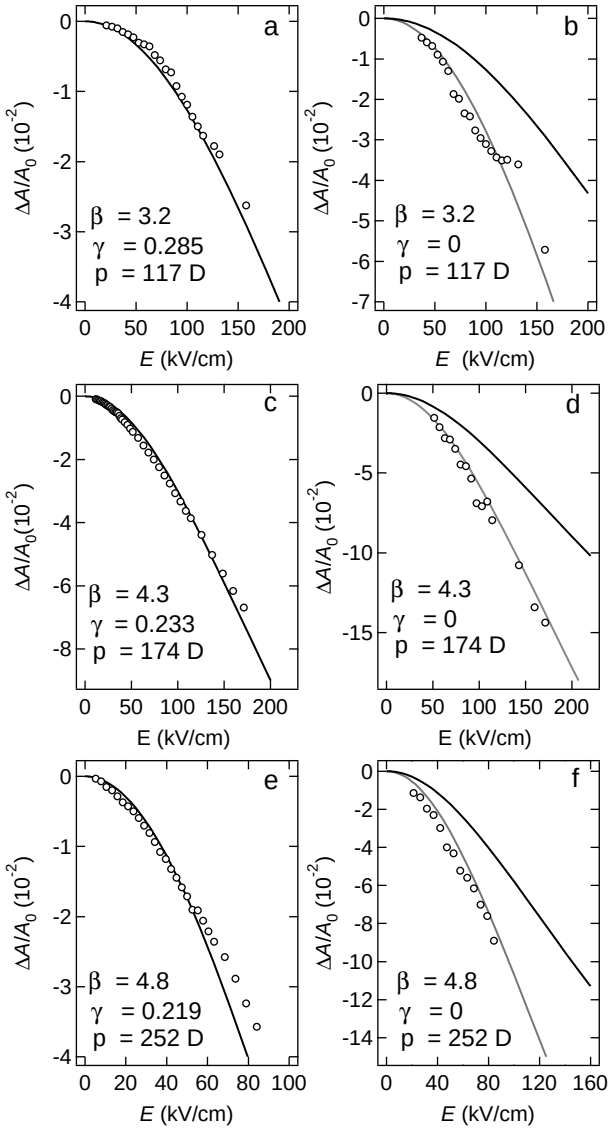

Figure 5.5: **(a)** (markers) Resulting relative change of the absorbance as a function of field strength and (black line) calculated change of $\langle|\Delta A|/A(0)\rangle$ according to eq. 5.1 for $p =$ 117 D and $\gamma = 0.285$ at 400nm for an aspect ratio β of 3.2 dot-in-rod. **(b)** (markers) Relative change of absorbance at the band edge, (black line) calculated change using the same vlaues for p and γ as in (a) and (grey line)calculated change taking $p = 174$ D and $\gamma = 0$. **(c),(d)** The same as(a),(b) for CdSe/CdS dot-in-rods with β= 4.3. **(e),(f)** The same as(a),(b) for CdSe/CdS dot-in-rods with β= 4.8.

One sees that two factors can lead to absorption anisotropy. First, anisotropic local field factors will lead to a dependence of $\sigma_{if,\mathrm{eV}}$ on the orientation of the rod relative to the optical electric field. As shown here, this suffices to understand absorption anisotropy at short wavelengths for CdSe QRs or CdSe/CdS dot-in-rods. Second, the transition matrix element $\langle f|\mathbf{e}\cdot\mathbf{r}|i\rangle$ can be orientation dependent. Clearly, this additional source of anisotropy is needed to explain why the variation of $\langle|\Delta A|/A(0)\rangle$ with applied field strength at the bandgap of the CdSe/CdS dot-in-rods can only be fitted by setting $\gamma = 0$. More precisely, defining the long axis of a QR as the z axis, the results obtained here show that $\langle f|z|i\rangle \gg \langle f|x|i\rangle$ for the band gap transition of CdSe/CdS dot-in-rods.

5.6 The temperature and the time-resolved spectoscopic study

In literature the band alignment and its influence on the radiative recombination process in dot-in-rods posses an open question. The optical measurements suggest a type 1.5 alignment in which the electron wavefunction is delocalised over the entire rod where as the hole wavefunction is localised in the core of the system[9–11]. On the contrary, ab initio quality charge patching method calculations resulted in type II band alignment[12]. In contrast, the scanning tunneling spectroscopy[13] and optical measurements[14,15] combined with the envelopefunction theoretical calculation results suggest a conduction band offset of ΔE=0.3 eV with a possibility to change from type I to type 1.5 configuration by tuning the core size. There is an essential need in understanding and control of the band alignment in dot-in-rods for prospective devcie fabrication. This is addressed in way by the temperature and time-resolved spectroscopic investigation of the wavefunction delocalisation in CdSe/CdS dot-in-rods. For this Photoluminescence(PL) as a function of temperature and time-resolved PL as a function of temperature are measured.

5.6.1 Photoluminescence as a function of temperature

PL intensity- The intensity of the PL spectrum was investigated as a function of temperature T for sample S4. The Figure 5.6a shows the PL spectrum and Fig. 5.6b shows the PL intensity observed at different temperatures. The observed PL intensity shows no considerable drop in intensity, which implies the strong suppression of the thermally activated recombination process. This can be due to the reduced density of defect states at the interface which acts as trap centers for non radiative decay process. In contrast, PL intensity of the CdSe/ZnS QDs reported in literature decreases with the increase in temperature. The use of CdS shell compared to ZnS shell lowers the lattice mismatch and hence minimises the occurrence of defect states. Therefore heterostructure configuration like CdSe/CdS system can suppress the temperature induced PL quenching.

PL Peak energy- Figure 5.6c shows results obtained by fitting single Gaussian function to the PL spectrum. The PL peak energy shifts to lower energies with increase in the temperature. This is attributed to the lattice deformation potential and exciton-phonon coupling leading to smaller energy band gap. The experimental data fits well with empirical Varshni's law for the band gap $E_g(T) = E_g(T = 0) - \alpha T^2/(T + \beta)$ as shown in Fig. 5.6c. The fitting parameter ($\alpha = 5 \times 10^{-4} eV/K; \beta = 250K$) on first approximation is similar to the bulk band gap of CdSe material[16,17]. This implies the emission originates mainly from electrons and holes near the band edge of the CdSe cores.

PL peak width- The temperature dependence of PL peak width has been fitted using exciton-phonon model, which has been successfully used for similar heterostructures before[16,17]. According to this model the peak width $\Gamma(T) = \Gamma_{inh} + \Gamma_{AC}T + \Gamma_{LO}(exp(-E_{LO}/(kT)) - 1)$, where Γ_{inh} is the inhomogeneous width, Γ_{AC} the exciton-acoustic phonon coupling coefficient,Γ_{LO} the exciton-LO phonon coupling coefficient, E_{LO} the LO phonon energy, and k the Boltzmann constant. The fitting parameters (Γ_{inh} =40 meV, Γ_{AC} =5 meV, Γ_{LO} =18 meV,E_{LO} =30 meV) are similar to the reported literature values[16,17].

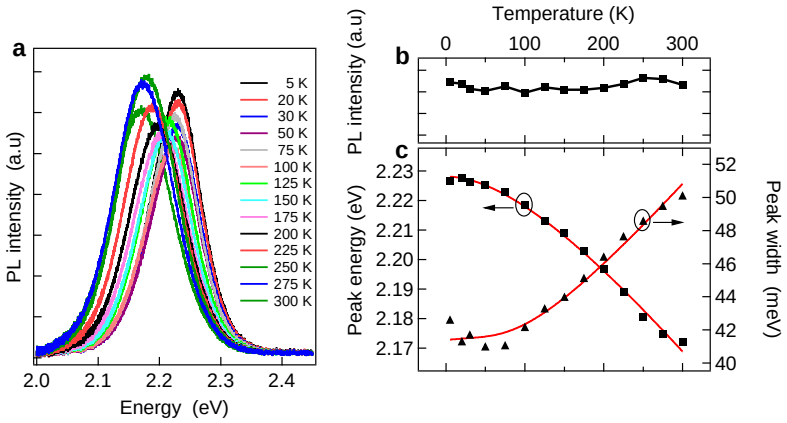

Figure 5.6: **(a)** The measured PL spectrum at different temperatures. **(b)** Integrated PL intensity *vs* temperature with no appreciable PL quenching observed. **(c)** Temperature dependence of PL peak energy (squares) and width (triangles). The solid lines are fits using the Varshni's law and the exciton-phonon model for the temperature variation of the energy and width, respectively.

The PL spectrum as function of temperature for CdSe/CdS dot-in-rod heterostructures shows no presence of defect states/dislocations at the interface and the PL emission originates from the charge carriers near the band edge of the CdSe cores.

5.6.2 Time-resolved Photoluminescence as function of temperature

This techinque gives insight on the decay process in the CdSe/CdS dot-in-rod heterostructures. The time-resolved PL spectrum as a function of temperature is shown in Fig. 5.7. The traces fit with single exponential function, suggesting single effective state contributes to the radiative recombination process. The observed lifetime increases with the temperature. On the contrary, in CdSe/ZnS QDs, the lifetime decreases with an increase in temperature and the decay process becomes strongly non-exponential. To explain the increase in the lifetime of dot-in-rods with the temperature, the investigation was extended to a set of samples with core diameters ranging from 2.2 nm to 3.3 nm (sample S4–S7)while keeping the shell thickness and shape same.

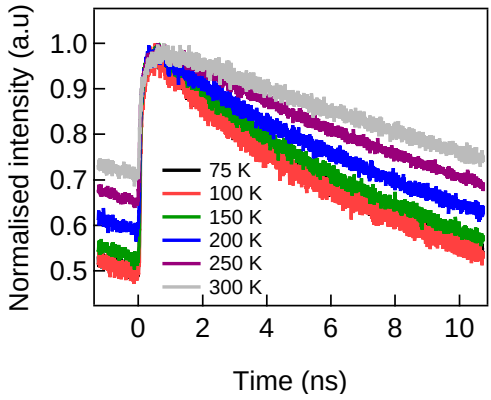

Figure 5.7: Time-resolved PL measurements *vs* temperature. A clear increase in exciton lifetime is observed.

The figure 5.8 summarises all the experimental results. In Fig. 5.8a, the energy difference of exciton absorption peak of CdSe core only and core-shell structure is plotted as function of core diameter. A stronger red shift is observed for cores with a smaller diameter. In addition, the room temperature exciton lifetime is plotted as function of the core size (see Fig. 5.7b). The heterostrutures with smaller cores are observed to have longer lifetime. If the CdSe/CdS dot-in-rods behaved as a simple CdSe core QDs, then an opposite trend would be observed, *i.e* a decrease in radiative lifetime with decrease in core size as the oscillator strength decreases (Fig. 3.9d shows radiative lifetime of CdSe QDs as function of their size). Therefore this can be understood interms of charge delocalization of the electron wave function in shallow potential well that is formed by CdSe/CdS heterostructure. In other words, smaller core exhibit larger electron delocalization and hence show longer radiative lifetimes.

The Fig. 5.8c shows exciton lifetime as a function of temperature in the range 75 K to 300 K for samples S4–S7. A clear size dependent radiative life time is observed. Particularly at 75 K, the lifetime changes from 16 ns to 8 ns for 2.2 nm to 3.3 nm core size samples respectively. This drop in factor of 2 is in agreement with a computed electron-hole overlap based on the envelope function approximation with an band offset of $\Delta E \approx 0.3$ eV between the CdSe and CdS conduction band[14]. Besides in all the samples the exciton lifetime increases with the temperature. This

behaviour cannot be explained neither on the basis of defect states nor on the basis of higher energy states with different oscillator strength. If this was the case then one would expect the PL to be quenched at higher temepratures because of trapping process and a non-exponential decay process in the latter case. Nontheless, it is well-known that the temperature alters the valence and the conduction band energies in semiconductors and semiconductor nanocrystals. This occurs due to the interaction of the lattice vibrations and a volume change. As a consequence the band offset is also temperature dependent. The experimentally observed increase in the lifetime infers to the increased electron delocalization resulting from a reduction of conduction band offset with an increase in temperature.

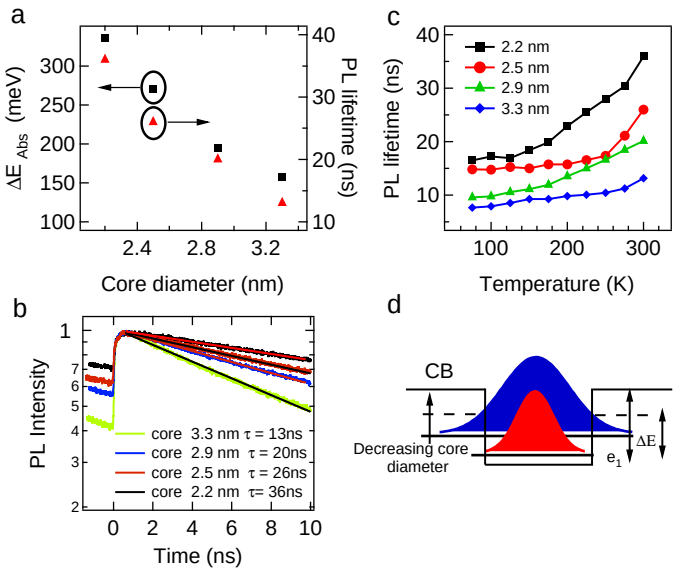

Figure 5.8: **(a)** (squares) Energy difference ΔE_{Abs} between first exciton peak of CdSe core only and CdSe/CdS heterostructure sructure together with (triangles) the PL lifetime as function of core diameter, measured at room temperature.**(b)** Shows the time-resolved PL traces for samples S4–S7 measured at room temperature.**(c)** Temeprature dependence of PL lifetime for all core diameters studied.**(d)** Schematic representation of the expected conduction band configuration, i.e, the change in the energy levels for different core diameters;the different degree of wave function delocalization together with the decrease of conduction band offset (ΔE) as a function of temperature.

5.7 Conclusions

Using electro-optical measurements, we have analyzed absorption anisotropy of dispersed CdSe/CdS dot-in-rods, in which the absorbance of the disperssion is measured while aligning the QRs by using alternating electric fields. Based on a quantitative analysis of the absorption change as a function of field strength, we find that the absorption at the bandgap is almost fully polarized, with a vanishing absorption coefficient for fields polarized perpendicular to the long axis of the rods. The nature of wave function delocalization in CdSe/CdS dot-in-rods has been investigated by temperature-resolved and time-resolved spectroscopy. We observed that the thermally induced PL quenching is absent, which enables to study the radiative decay process directly and its effects on the wave function delocalization. The radiative lifetime increases with decreasing CdSe core size has been observed, this is caused by different degree of localization of the electronic wave function. Besides this the radiative lifetime also increases with temperature due to the change in the band offset. This change in lifetime, quantitatively agrees with a conduction band offset of 0.3 eV, as reported in literature[13,14]. These results indicate that the degree of electron delocalization in the lowest conduction band level can be controlled by the size of the core and the temperature.

Bibliography

[1] P. D. Cozzoli, T. Pellegrino and L. Manna, *Synthesis, properties and perspectives of hybrid nanocrystal structures*, Chem. Soc. Rev. **2006**, *35*, 1195.

[2] N. Liu, B. S. Prall and V. I. Klimov, *Hybrid gold/silica/nanocrystal-quantum-dot superstructures: synthesis and analysis of semiconductor-metal interactions*, J. Am. Chem. Soc. **2006**, *128*, 15362.

[3] D. V. Talapin et al., *Highly emissive colloidal CdSe/CdS heterostructures of mixed dimensionality*, Nano Lett. **2007**, *7*, 2942.

[4] L. Carbone et al., *Synthesis and micrometer-scale assembly of colloidal CdSe/CdS nanorods prepared by a seeded growth approach*, Nano Lett. **2007**, *7*, 2942.

[5] Y. W. Lin, W. L. Tseng and H. T. Chang, *Using a layer-by-layer assembly technique to fabricate multicolored-light-emitting films of CdSe@CdS and CdTe quantum dots*, Adv. Mater. **2006**, *18*, 1381.

[6] X. Michalet et al., *Quantum dots for live cells, in vivo imaging, and diagnostics.*, Science **2005**, *307*, 538.

[7] J. Jasieniak et al., *Re-examination of size-dependent absorption properties of CdSe auqntum dots*, J. Phys. Chem. C **2009**, *113*, 19468.

[8] E. Merzbacher, *Quantum Mechanics (Wiley, New York, 1970)* .

[9] J. Muller et al., *Wave function engineering in elongated semiconductor nanocrystals with heterogeneous carrier confinement*, Nano Lett. **2005**, *5*, 2044.

[10] J. Muller et al., *Monitoring surface charge movement in single elongated semiconductor nanocrystals*, Phys. Rev. Lett. **2004**, *93*, 167402.

[11] M. G. Lupo, *Ultrafast electron-hole dynamics in core/shell CdSe/CdS dot/rod nanocrystals*, Nano Lett. **2008**, *8*, 4582.

[12] Y. Luo and L. W. Wang, *Electronic structures of the CdSe/CdS core-shell nanorods*, ACS Nano **2010**, *4*, 91.

[13] D. Steiner et al., *Determination of band offsets in heterostructured colloidal nanorods using scanning tunneling spectroscopy*, Nano Lett. **2008**, *8*, 2954.

[14] A. Sitt et al., *Multiexciton engineering in seeded core/shell nanorods: transfer from type-I to quasi-type-II regimes*, Nano Lett. **2009**, *9*, 3470.

[15] G. Morello et al., *Intrinsic optical nonlinearity in colloidal seeded grown CdSe/CdS nanostructures: photoinduced screening of the internal electric field*, Phys. Rev. B **2008**, *78*, 195313.

[16] D. Valerini et al., *Temperature Dependence of the Photoluminescence Properties of Colloidal CdSe/ZnS Core/Shell Quantum Dots Embedded in a Polystyrene Matrix*, Phys. Rev. B **2005**, *71*, 235409.

[17] P. Jing et al., *Temperature-dependent photoluminescence of CdSe-core CdS/CdZnS/ZnS-multishell quantum dots.*, J. Phys. Chem. C **2009**, *113*, 13545.

Chapter VI

PbS-based quantum rods by cationic exchange, structural analysis

6.1 Introduction

Heterostructure with dot-in-rod configuration combines the mixed dimensional properties of zero dimensional and one dimensional system with tunable anisotropic opto-electronic properties. A fine example of such a material system is heterogeneous CdSe/CdS dot-in-rods[1,2]. These materials display, excellent polarized photoluminescence (PL) tunable from green to red with high quantum efficiencies[3] of about 75% . Their homogeneity arising from exceptional synthetic control allows them to be assembled in close-packed ordered arrays.[4] However, with bulk bandgaps of 1.74 eV (CdSe) or 2.40 eV (CdS), cadmium chalcogenide (CdX) QRs are mainly of interest for applications involving visible light. In this chapter, we extend the PL wavelength range of colloidal QRs to the near-IR by demonstrating the formation of efficiently emitting heteronanorods that feature multiple PbS dots in a single CdS rod. Heterostructures based on lead chalcogenide materials are attractive proposition in near IR applications and are of great technological importance.

In the case of CdX, rod growth is made possible by the combination of an anisotropic crystal structure (wurtzite) and specific surface ligands (phosphonic acids).[5] However the synthesis of QRs

active in the near-IR (800-3000 nm) has proved to be more challenging. Lead chalcogenides (PbX), the most widely used near-IR quantum dots (QDs), have a cubic crystal structure. In that case, rod or wire growth has only been achieved with indirect methods such as chelation of the precursors[6], heterogeneous seeding[7], cationic exchange[8] and oriented attachment of QDs[9]. PbS QRs have been successfuly synthesised by cationic exchange. This reaction involves two steps, in the first step the CdS QRs are exchanged to form Cu_2S QRs and in the second step Cu_2S QRs are exchanged to form PbS QRs. This gives an advantage as the enormous variety of sizes, aspect ratios, and materials accessible via CdX QR synthesis can be transferred to PbX QRs.

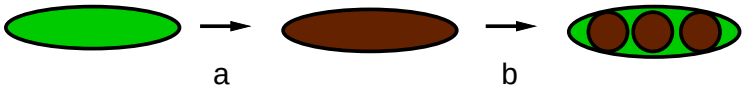

Figure 6.1: Schematic diagram of formation of PbS/CdS multiple dot-in-rod heterostructure(a) CdS rod is converted to PbS rod by cationic exchange.(b) PbS rod is partially exchanged to form PbS/CdS multiple dot-in-rod heterostructure

In this study, we take PbS QRs formation by cationic exchange as a starting point. By exposing PbS QRs to a cationic solution of Cd results in the fomation of PbS/CdS multiple dot-in-rods. We examine the formation of complex PbS/CdS multiple dot-in-rods from the starting material by high resolution transmission electron microscopy (HR-TEM) and high annular dark field scanning transmission electron microscopy (HAADF-STEM). This enables direct visualization of the crystallographic properties of PbS/CdS multiple dot-in-rods and evaluation of the cationic exchange reaction. In this chapter, sample A and sample B refers to multiple dot-in-rods with dimensions of 3.7 nm x 28 nm and 5 nm x 16.5 nm respectively. The sample A is used in explaining the work done here and is compared with the sample B towards the end of this chapter. The synthesised QRs used in this entire work has been prepared by Yolanda Justo (PCN).

6.2 Experimental

6.2.1 Synthesis

CdS QRs - CdS QRs were synthesized according to a literature procedure[2]. In sample A, first CdS core QDs with a diameter of 3.5 nm are synthesized. For this, a mixture of 0.10 g CdO, 3.29 g of TOPO and 0.60 g of ODPA was degassed under vacuum at 120 °C for one hour. Next, the mixture was heated to 320 °C under nitrogen atmosphere and a mixture of 0.17 g of bis(trimethylsilyl) sulfide [$(TMS_2)S$] and 3 g of tri-n-butylphosphine (TBP) was quickly injected. The reaction mixture is quenched after 2 minutes and purified three times by using toluene and methanol as solvent and non solvent respectively, followed by centrifugation and decantation. The rods are prepared from a mixture of 0.09 g of CdO, 3 g of TOPO, 0.3 g of ODPA and 0.08 g of HPA which is degassed under vacuum at 150 °C for one hour. Next, the mixture is heated to 350 °C under nitrogen atmosphere and 1.8 mL of TOP is injected. Subsequently at the same temperature 0.12 g of S in 1.8 mL of TOP and 100 L of the cores are injected to the reaction mixture. The reaction mixture is quenched after 8 minutes with toluene, purified as described for CdS cores and resuspended in 5 mL of toluene.

Cationic exchange: from CdS QRs to PbS QRs The exchange reaction is done in two steps based on the procedure reported by Luther *et al.*[8]. In the primary step CdS QRs are converted to Cu_2S QRs by injecting tetrakis(acetonitrile)copper(I) hexafluoro phosphate dissolved in methanol to a dispersion of CdS QRs in toluene at room temperature under nitrogen atmosphere. The reactant mixture is prepared in a way that the Cu:Cd is in excess of 20:1. Thus formed Cu_2S QRs are washed twice with methanol and resuspended in toluene. In the second step the Cu_2S QRs are converted to PbS QRs. For this Cu_2S QRs are injected in a mixture of 0.8 mM of lead (II) acetate trihydrate in methanol and 1.6 mM of TBP in toluene to react at 0 °C for half an hour. The PbS QRs thus formed are washed twice with methanol and resuspended in toluene to be stored under nitrogen atmosphere.

PbS/CdS multiple dot-in-rod A mixture of 8 mmol CdO, 32 mmol of OA and 73 mmol of diphenyl ether (DPE) is heated to

200 °C under nitrogen atmosphere for half an hour. Subsequently it is injected to the PbS QRs suspension at lower temperatures while keeping the Cd to Pb content with an excess of 10:1. The reaction mixture was quenched after certain time with a mixture of 1 mL of butanol and 2 mL of methanol. Thus obtained PbS/CdS QRs are washed twice with methanol and resuspended in toluene.

6.2.2 TEM Characterization

HR-TEM and EDS analysis was carried out with a JEOL 2200-FS microscope equipped with a Cs corrector for the objective lens. TEM samples were prepared by drop casting a dilute suspension ($\pm 1\,\mu$L) of the QR sample in toluene on a carbon-coated TEM grid. To improve the contrast, a high contrast aperture with Z-filter has been used. Based on the TEM images, mean diameter and mean length of the QRs is determined by analyzing 100–150 particles for each sample. The HR-STEM investigation and analysis was done at EMAT, Antwerp university, by Bart Goris and prof. Sara Bals. The annular dark field HR-STEM images were recorded with an aberration corrected FEI-Titan 50-80 transmision electron microscope.

6.3 CdS and PbS quantum rods

6.3.1 Basic materials characterization

The cationic exchange experiment was conducted using CdS QRs with a mean diameter of 3.7 nm and a length of 28 nm. Figure 6.2a shows a representative TEM image of CdS QRs, demonstrating their regular shape and monodispersity. During the intermediate exchange step, the Cu_2S QRs formed contain clusters at the tips as shown in Fig.6.2b. Finally, the PbS QRs formed on complete exchange have an irregular, wavy shape (see Fig.6.2c). The XRD diffractogram shown in Fig.6.2d, e confirms the formation of CdS QRs with wurtzite crystal structure and PbS QRs with rock salt crystal structure, respectively.

Absorption spectroscopy allows to monitor the cationic exchange process more closely during synthesis. The cationic exchange reaction is initiated with CdS QRs (with dimensisons 3.7 nm x 28 nm), which has a absorption peak around 500 nm. This absorption feature corresponds to the first exciton bandgap tran-

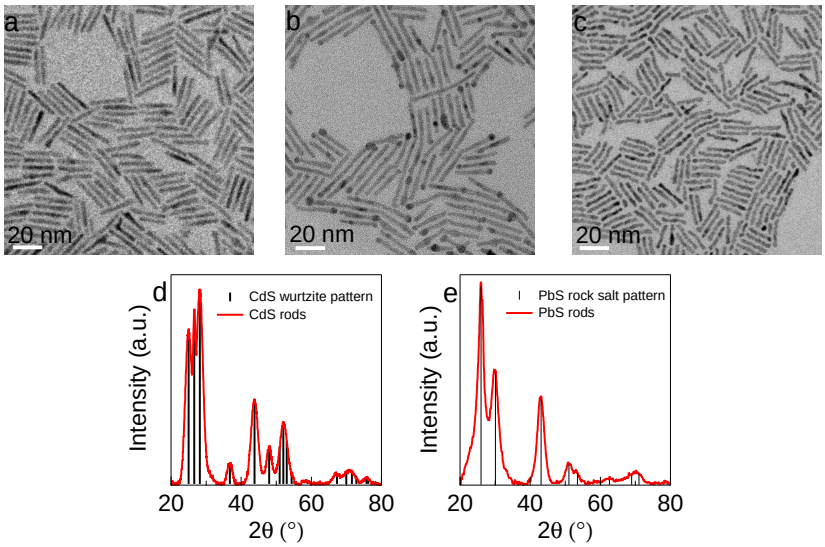

Figure 6.2: Overview of TEM images of (a) starting CdS QRs, (b) intermediate Cu_2S QRs and (d) final PbS QRs. XRD pattern of (e) CdS QRs and (f) PbS QRs.

sition. As the cationic exchange reaction progresses, on exchange of Cd by Cu the absorption spectrum loses its feature, which is due to the formation of Cu_2S intermediate QRs (also confirmed by TEM see Fig.6.2b). Finally, after the exchange of Cu by Pb, an absorption feature is retrieved in the near IR corresponding to the PbS bandgap transition.

6.3.2 Analysis of the initial CdS QRs

CdS QRs were examined by HR-TEM. Multiple wurtzite/zincblende stacking faults in successive (0001) planes perpendicular to the c-axis are observed. Stacking fault is a planar defect in crystals. This happens when the normal stacking sequences which is ABABAB for a hexagonal closed packed system changes to ABABCBC over a few atomic spacing. Figure 6.4 shows the schematic representation of a stacking fault along the (0001) plane. The observed stacking faults in CdSe QRs is shown in Fig.6.4.

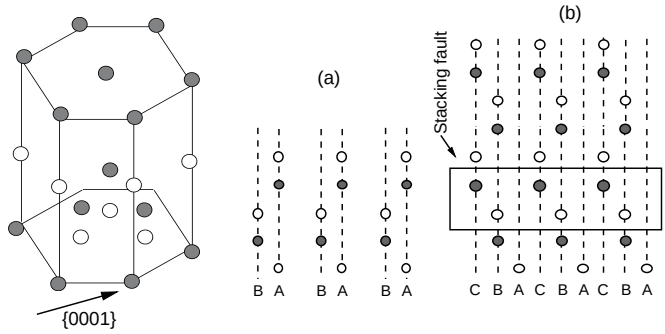

Figure 6.3: Shows wurtzite crystal structure viewed along (0001) direction (where white spheres–Cd atoms, grey spheres–S atom) (a) normal stacking squence and (b) In the presence of wurtzite/zincblende stacking fault.

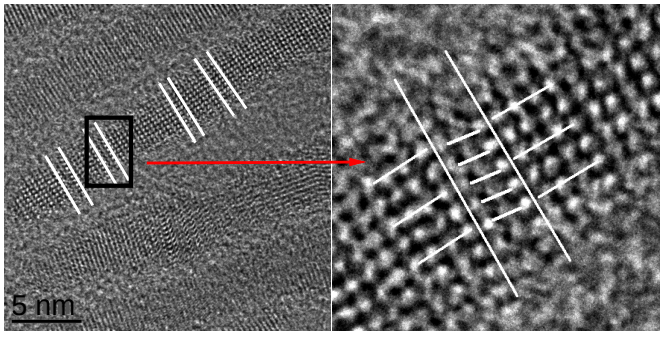

Figure 6.4: HR-TEM image of CdS rods with stacking faults marked between the lines

6.3.3 Analysis of the fully exchanged PbS QRs

The fully exchanged PbS QRs is represented with a HR-TEM image along the [110] zone axis in Fig.6.5. The QRs are observed to have different crystallite segments and hence are polycrystalline. The different crystallite segments observed in HR-TEM image (in Fig.6.5) corresponds to the same [110] zone axis as evident from the ⟨110⟩ unit cell highlighted in the Fig.6.5 with an inplane rotation between the planes. On taking a closer look at the HR-TEM image grain boundries are observed between different crystallites seperated by (111) twin planes. Twin planes occur due to twining which is a planar crystal defect occuring due to stacking fault continued over a large number of lattice planes. The distance between the twin planes observed in PbS QR is comparable to the

distance between the stacking faults observed in initial CdS QRs. A similar observation on the morphology of PbS QRs synthesised by cationic exchange was reported by Luther *et al.* in literature[8]. According to his theory, Pb^{+2}-Cu^{+1} exchange front moves along the nanocrystal during the reaction, these displacement causes misalignment of the long axis of PbS segment which gives rise to the wavy shape of the rods. The reaction front can start at one or both the ends and when reaction front meet on complete exchange results in the formation of grain boundaries. Here, HR-TEM indicates that the PbS QRs can be composed of more than two segments(see Fig.6.5). In the example given, five segments can be discerned, but their actual number changes depend on, *e.g.*, the length of the QR. This indicates that the exchange can also start at the sides of the QRs. Possibly this is driven by stacking faults in the original CdS rods.

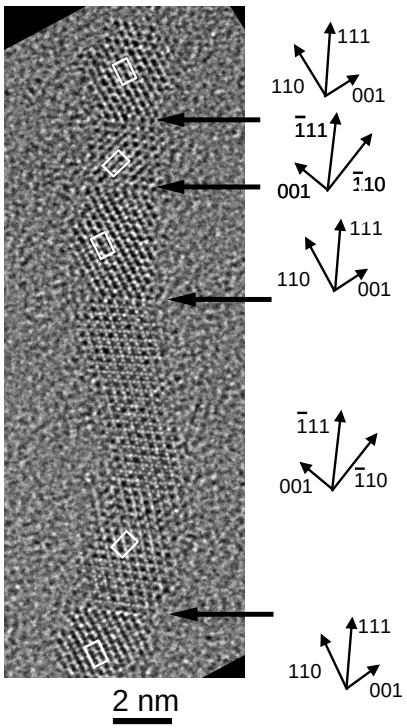

Figure 6.5: HR-TEM image of a PbS QR in [110] zone axis. The five segements in the QR are indicated with arrows and the corresponding crystal orientation is given next to it.

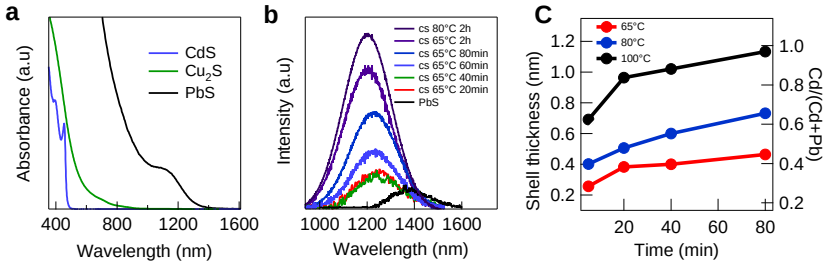

Figure 6.6: (a) Absorption spectrum of CdS,Cu_2S and PbS QRs during the course of cationic exchange (b) Evolution of the PL spectrum with reaction time for an exchange reaction at 65 ℃, and final PL spectrum for an exchange reaction at 80 ℃(sample A rods) Evolution of the ratio Cd/(Pb+Cd) and the nominal CdS shell thickness as a function of the reaction time for different reaction temperatures (sample A rods). (c) Evolution of the PL spectrum with reaction time for an exchange reaction at 65 C, and final PL spectrum for an exchange reaction at 80 ℃(sample A rods).

6.4 PbS/CdS multiple dot-in-rod

6.4.1 Basic material characterization

The main drawback of the PbS QRs is their low photoluminescence quantum yield (PLQY) of about 9%. In the case of PbX QDs, growth of a CdX shell by cationic exchange has been proposed as a way to enhance and stabilize the PLQY.[10,11] In line with this result, a suspension of PbS QRs in toluene was exposed to an excess of Cd oleate at elevated temperature for successive exchange. Elemental analysis by TEM-EDX shows that this leads to a progressive replacement of Pb by Cd, which is more pronounced the longer the reaction time or the higher the temperature (see Fig.6.6c). For exchange temperatures of 65–100 ℃ , 45–95% of the Pb atoms are replaced by Cd, corresponding to a nominal shell thickness of 0.4–1.2 nm, respectively. As compared to the original PbS QRs, the PL spectrum of the PbS/CdS heterorods shifts to shorter wavelengths, and, more importantly, the PLQY increases sharply. After 120 min of shell growth, it reaches 45 or 55% if the exchange is done at 65 or 80 ℃, respectively.

6.4.2 STEM-HAADF analysis

The morphology of the QRs was studied in detail using STEM-HAADF, since the STEM-HAADF signal intensity increases with the atomic weight of the element probed. With core/shell PbS/CdS heterorods, this should result in images showing a bright (PbS) core and a darker (CdS) shell. This is not what is observed. For sample A, with the final Pb-for-Cd exchange done at 65 °C, the overview image (Fig.6.7a) already shows that each rod is composed of a series of brighter and darker segments, featuring 4 to 5 bright parts. Figure 6.7b demonstrates that the bright segments are embedded in the darker rod. We interpret this as an evidence for the formation of multiple PbS dots in a single CdS rod. Similar results are obtained when starting from CdS rods with different aspect ratios (5nm x 16.5 nm). A HR-STEM image (Fig.6.7c) shows that the polycrystallinity of the original PbS QRs is maintained in the PbS/CdS heterorods. Especially in the case of sample B rods, STEM-HAADF indicates that each PbS crystallite is transformed into a single PbS/CdS segment (see Fig.6.7d). This indicates that the multiple dot-in-rod heterostructures form because the cationic exchange proceeds quickly along the (defect-rich) interfaces between the original PbS segments. Importantly, this suggests that the morphology of these multiple dot-in-rod heterostructures can be tuned by adjusting the size of the PbS segments in the original PbS rods. Possibly, these reactive interfaces account for the difference with PbX rods made by oriented attachment, where partial Pb/Cd exchange rarely leads to multiple dot-in-rods.[12] Averaging 150 embedded PbS dots (sample A), we find an effective average diameter of 3.7 nm, with a size dispersion of 15%. Similar results with less homogeneous PbS dots, are obtained with a Pb-for-Cd exchange at 80 °C.

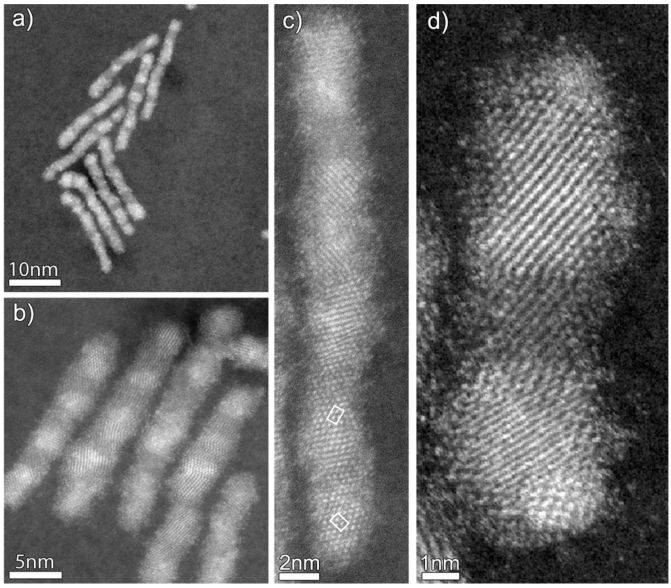

Figure 6.7: STEM-HAADF images of PbS/CdS rods showing multiple PbS QDs inside the rods recorded on (a-c) sample A and (d) sample B. The white rectangles in (c) indicate the ⟨110⟩ unit cell.

6.5 conclusions

Colloidal PbS/CdS heterorods have been synthesized by successive cationic exchange steps, with a high PLQY in the near-IR out of CdS quantum rods. The resulting particles are evaluated by TEM based techniques. The successive, complete Cd/Cu and Cu/Pb exchanges lead to polycrystalline PbS QRs with a limited PLQY. A final Cd/Pb partial exchange raises the PLQY up to 55%. Instead of simple core/shell structures, this results in the formation of multiple dot-in-rod heterostructures, probably because each PbS segment in the original PbS QR is transformed into a single PbS/CdS unit. The number of PbS dots in a single rod depends on the original CdS rod length. Since further tuning is possible by limiting the extent of the final cationic exchange,[8] this shows that successive cationic exchange is a versatile approach to form complex anisotropic heteronanostructures active in the IR. This opens new vistas in the development of applications in, *e.g.*, solar concentrators and QD-based near-IR light sources.

Bibliography

[1] D. V. Talapin et al., *Highly emissive colloidal CdSe/CdS heterostructures of mixed dimensionality*, Nano Lett. **2003**, *3*, 1677.

[2] L. Carbone et al., *Synthesis and micrometer-scale assembly of colloidal CdSe/CdS nanorods prepared by a seeded growth approach*, Nano lett. **2007**, *7*, 2942.

[3] D. V. Talapin et al., *Highly emissive colloidal CdSe/CdS heterostructures of mixed dimensionality*, Nano Lett. **2007**, *7*, 2942.

[4] M. Zanella et al., *Self-assembled multilayers of vertically aligned semiconductor nanorods on device-scale areas*, Adv. Mater. **2011**, *23*, 2205.

[5] X.G.Peng et al., *Shape control of CdSe nanocrystals*, Nature **2000**, *404*, 59.

[6] E. Lifshitz et al., *Synthesis and characterization of PbSe quantum wires, multipods, quantum rods, and cubes*, Nano Lett. **2003**, *3*, 857.

[7] K. T. Yong et al., *Shape control of PbSe nanocrystals using noble metal seed particles*, Nano Lett. **2006**, *6*, 709.

[8] J. M. Luther et al., *Synthesis of PbS nanorods and other ionic nanocrystals of complex morphology by sequential cationexchange reactions*, J. Am. Chem. Soc. **2009**, *131*, 16851.

[9] W.-K. Koh et al., *Synthesis of monodisperse PbSe nanorods: a case for oriented attachment*, J. Am. Chem. Soc. **2010**, *132*, 3909.

[10] J. M. Pietryga et al., *Utilizing the lability of lead selenide to produce heterostructured nanocrystals with bright, stable infrared emission*, J. Am. Chem. Soc. **2008**, *130*, 4879.

[11] K. Lambert et al., *PbTe—CdTe core—shell particles by cation exchange, a HR-TEM study*, Chem. Mater. **2009**, *21*, 778.

[12] M. Casavola et al., *Anisotropic cation exchange in PbSe/CdSe core/shellnanocrystals of different geometry*, Chem. Mater. **2012**, *24*, 294.

Chapter VII

General Conclusions

This work, starting from colloidal quantum dots (QDs) to hetero quantum rods (QRs) highlights their synthesis, strutural analysis and optical properties. This chapter summarises all the results.

In chapter 3, optical properties of CdTe QDs are investigated. CdTe QDs are synthesised by the hot injection method. The synthesised QDs are examined by X-ray diffraction (XRD), which confirms the formation of zinc blende crystal structure. Their mean diameter and size dispersion is determined by transmission electron microscopy (TEM) measurements. UV-vis absorption spectra clearly shows a blue shift of the band gap with respect to bulk CdTe. Combining the band gap and the mean diameter of the CdTe QDs a sizing curve is constructed. The concentration of the CdTe QDs is determined by inductively coupled plasma mass spectrometry (ICP-MS) and Rutherford backscattering spectroscopy (RBS) measurements. Combining concentration, absorbance and mean diameter data, the absorption coefficients of CdTe QDs are calculated and compared with the literature data. We observe at 410 nm, intrinsic absorption coefficient μ_i is size-independent. The resulting value is close to the expected value for bulk CdTe determined by using Maxwell-Garnett model and can be used for determining the volume fraction of spherical CdTe QDs in colloidal dispersions. Despite the size-independent μ_i at 410 nm, we observe persistent quantum confinement effects on the E_1 transition, which appears less pronounced and blueshifted in CdTe QDs relative to its bulk value of 365 nm.

Around the band gap, we find an integrated absorption coefficient μ_{gap} that scales proportionally to the inverse of the QD volume. Especially for the smaller diameters, significant deviations are found as compared to widely used literature values. The corresponding oscillator strength f_{exc} is calculated from the μ_{gap} and is almost size-independent in the diameter range 3–7 nm. Radiative lifetimes predicted based on f_{exc} are in line with experimental results and published values if a 16-fold degeneracy for the first exciton is assumed.

In chapter 4 and chapter 5, the absorption anisotropy in CdSe QRs, CdS QRs and CdSe/CdS dot-in-rods are investigated. The QRs are synthesised by the hot injection synthesis. The synthesised QRs are exmained by XRD which confirms the formation of QRs with wurtzite crystal structure. The dimensions of the QRs are deduced by TEM measurements. In the case of synthesised CdSe QRs dispersed in heptane, the experimental absorption coefficient μ at 400 nm is determined by combining UV-vis absorption spectroscopy and elemental analysis. The results show that absorption coefficient μ at 400 nm is in line with the theoretical values calculated in the frame work of Maxwell-Garnett model using local field approximatiom. The absorption coefficient of colloidal CdSe QRs is neither a constant nor equal to that of colloidal CdSe QDs. Due to the anisotropy of the local field factors, it markedly increases with increasing aspect ratio, making QRs in general stronger absorbers than QDs of the same material. The absorption anisotorpy implies that randomly dispersed CdSe QRs have larger absorption coefficient than CdSe QDs.

In addtion, we introduce and assess an electro-optical method to analyze absorption anisotropy of dispersed QRs. In this method, the absorbance of the dispersion is measured while aligning the nanocrystals using an electric field. Using alternating electric fields high enough to prevent charge accumulation at the electrodes and low enough to ensure rotational relaxation, we demonstrate that the resulting change in absorbance as a function of field strength can be quantified by a model based on Boltzmann statistics. The method is validated using CdSe and CdS quantum rods, where we find a difference between the absorption coefficient at 400 nm and at bandgap for fields polarized parallel and perpendicular to

the rod axis that is fully in line with the predictions of the local field approximation. Finally, using this method, we extended the analysis to the first exciton transition of CdSe/CdS dot-in-rods. Based on a quantitative analysis of the absorption change as a function of field strength, we find that this absorption is almost fully polarized, with a vanishing absorption coefficient for fields that are polarized perpendicular to the long axis of the rods.

The nature of wave function delocalization in CdSe/CdS dot-in-rods has been investigated by temperature-resolved and time-resolved spectroscopy. We observed that the thermally induced photoluminescence (PL) quenching is absent, which enables to study the radiative decay process directly and its effects on the wave function delocalization. The radiative lifetime increases with decreasing CdSe core size has been observed, this is caused by different degree of localization of the electronic wave function. Besides this the radiative lifetime also increases with temperature due to the change in the band offset. This change in lifetime, quantitatively agrees with a conduction band offset of 0.3 eV, as reported in literature. These results indicate that the degree of electron delocalization in the lowest conduction band level can be controlled by the size of the core and the temperature.

In chapter 6, colloidal PbS/CdS heterorods are synthesised by successive cationic exchange steps, starting from CdS quantum rods. The resulting particles are evaluated by absorption spectroscopy, photoluminescence spectroscopy and TEM based techniques. The successive, complete Cd/Cu and Cu/Pb exchanges leads to the formation of PbS QRs. Thus formed PbS QRs are observed to be polycrystalline. The different crystallities observed to have grain boundaries and are seperated by (111) twin planes. The distance between different twin planes is comparable to the stacking fault observed in CdS QRs. The photoluminescence quantum yield measured in PbS QRs is observed to be very low compared to 55% in PbS/CdS heterorods formed by partial exchange Cd/Pb. Instead of simple core/shell structures, this results in the formation of multiple dot-in-rod heterostructures, probably because each PbS segment in the original PbS QR is transformed into a single PbS/CdS unit. The number of PbS dots in a single rod depends on the original CdS rod length. Since further tuning

is possible by limiting the extent of the final cationic exchange, this shows that successive cationic exchange is a versatile approach to form complex anisotropic heteronanostructures active in the IR. This opens new vistas in the development of applications in, *e.g.*, solar concentrators and QD-based near-IR light sources.

List of publications

International Journals

1. J. S. Kamal, A. Omari, K. Van Hoecke, Q. Zhao, A. Vantomme, F. Vanhaecke, R. K. Čapek and Z. Hens, *Size-dependent optical properties of zinc blende cadmium telluride quantum dots*, J. Phys. Chem. C **2012**,*112*, 5049.

2. J. S. Kamal, R. Gomes, M. Karvar, K. Neyts, S. Compernolle, F. Vanhaecke and Z. Hens, *Direct determination of absorption anisotropy in colloidal quantum rods*, Phys. Rev. B **2012**, *85*, 035126.

3. Y. Justo, B. Goris, J. S. Kamal, P. Geiregat, S. Bals and Z. Hens, *Multiple dot-in-rod PbS/CdS heterostructures with high photoluminescence quantum yield in the near-infrared*, J. Am. Chem. Soc. **2012**, *134*, 5484.

4. G. Rainò, T. Stöferle, I. Moreels, R. Gomes, J. S. Kamal, Z. Hens and R. F. Mahrt *Probing the wave function delocalization in CdSe/CdS dot-in-rod nanocrystals by time- and temperature-resolved spectroscopy*, ACS Nano **2011**, *5*, 4031.

5. K. Lambert, Y. Justo, J. S. Kamal and Z. Hens, *Phase transitions in quantum-dot Langmuir films*, Angew. Chem. **2011**, *50*, 12058.

International Conference Contributions

6. J. S. Kamal, R. Gomes, M. Karvar, K. Neyts, S. Compernolle, F. Vanhaecke and Z. Hens, *Understanding absorption coefficient anisotropy of colloidal quantum rods*, E-MRS Spring Meeting 2011, Nice, France **2011**.

7. J. S. Kamal, R. Gomes, M. Karvar, K. Neyts, S. Compernolle, F. Vanhaecke and Z. Hens, *Direct determination of absorption anisotropy in colloidal quantum rods*, Scientific meeting on Chemistry related to Physics Material Sciences, Veldhoven, Netherlands **2011**.

8. J. S. Kamal, R. Gomes, M. Karvar, D. De Muynck, F. Vanhaecke, K. Neyts and Z. Hens, *Anisotropic local field factors determine the absorption coefficient of colloidal quantum rods*, TNT2010, Braga, Portugal **2010**.

9. J. S. Kamal, D. De Muynck, Q. Zhao, A. Vantomme, F. Vanhaecke, R. K. Čapek and Z. Hens, *Size dependent optical properties of zinc blende CdTe nanocrystals*, TNT2010, Braga, Portugal **2010**.

10. J. S. Kamal, D. De Muynck, Q. Zhao, A. Vantomme, F. Vanhaecke, R. K. Čapek and Z. Hens, *The optical properties of CdTe nanocrystals*, Scientific meeting on Chemistry related to Physics Material Sciences, Lunteren, Netherlands **2009**.